

NAVAL POSTGRADUATE SCHOOL

Monterey, California



THESIS

**APPLICATION OF THE ROBUST SYMMETRICAL
NUMBER SYSTEM TO HIGH RESOLUTION DIRECTION
FINDING INTERFEROMETRY**

by

David J. Wickersham

March 2000

Thesis Advisor:
Co-advisor:

Phillip E. Pace
D. Scott Davis

Approved for public release; distribution is unlimited.

DTIC QUALITY INSPECTED 4

20000623 082

REPORT DOCUMENTATION PAGE

Form Approved
OMB No. 0704-0188

Public reporting burden for this collection of information is estimated to average 1 hour per response, including the time for reviewing instruction, searching existing data sources, gathering and maintaining the data needed, and completing and reviewing the collection of information. Send comments regarding this burden estimate or any other aspect of this collection of information, including suggestions for reducing this burden, to Washington Headquarters Services, Directorate for Information Operations and Reports, 1215 Jefferson Davis Highway, Suite 1204, Arlington, VA 22202-4302, and to the Office of Management and Budget, Paperwork Reduction Project (0704-0188) Washington DC 20503.

1. AGENCY USE ONLY (Leave blank)		2. REPORT DATE March, 2000	3. REPORT TYPE AND DATES COVERED Master's Thesis
4. TITLE AND SUBTITLE Application of the Robust Symmetrical Number System to High Resolution Direction Finding Interferometry			5. FUNDING NUMBERS
6. AUTHOR(S) Wickersham, David J.			
7. PERFORMING ORGANIZATION NAME(S) AND ADDRESS(ES) Naval Postgraduate School Monterey, CA 93943-5000			8. PERFORMING ORGANIZATION REPORT NUMBER
9. SPONSORING / MONITORING AGENCY NAME(S) AND ADDRESS(ES)			10. SPONSORING / MONITORING AGENCY REPORT NUMBER
11. SUPPLEMENTARY NOTES The views expressed in this thesis are those of the author and do not reflect the official policy or position of the Department of Defense or the U.S. Government.			
12a. DISTRIBUTION / AVAILABILITY STATEMENT Approved for public release; distribution unlimited.			12b. DISTRIBUTION CODE
13. ABSTRACT (maximum 200 words) <p>To reduce the number of phase sampling comparators in a direction finding (DF) interferometer antenna, a new array based on a robust symmetrical number system (RSNS) is described. The RSNS is used to decompose the spatial filtering operation into a number of parallel sub-operations that are of smaller computational complexity. Each sub-operation (interferometer) symmetrically folds the phase with folding period equal to $2Nm_i$ where N is the number of channels that are used and m_i is the channel modulus. A small comparator ladder mid-level quantizes each folded phase response. Each sub-operation only requires a precision in accordance with that modulus. A much higher DF resolution is achieved after the N different RSNS moduli are used and the results of these low precision sub-operations are recombined. The parallel use of phase waveforms increases the antenna resolution without increasing the folding rate of the system. The new antenna is constructed and tested in an anechoic chamber, and the results are compared with the experimental results of a previously tested optimum symmetrical number system (OSNS) array. Although the dynamic range of the RSNS is somewhat less than the OSNS, the inherent Gray code properties make it attractive for error control in phase sampling interferometry.</p>			
14. SUBJECT TERMS Robust symmetrical number system; Optimum symmetrical number system; Phase sampling interferometry; Direction finding, Ambiguity resolution.			15. NUMBER OF PAGES 164
16. PRICE CODE			
17. SECURITY CLASSIFICATION OF REPORT Unclassified	18. SECURITY CLASSIFICATION OF THIS PAGE Unclassified	19. SECURITY CLASSIFICATION OF ABSTRACT Unclassified	20. LIMITATION OF ABSTRACT UL

NSN 7540-01-280-5500

Standard Form 298 (Rev. 2-89)
Prescribed by ANSI Std.

Approved for public release; distribution is unlimited

**APPLICATION OF THE ROBUST SYMMETRICAL NUMBER SYSTEM TO HIGH
RESOLUTION DIRECTION FINDING INTERFEROMETRY**

David J. Wickersham
Lieutenant, United States Navy
B.S., United States Naval Academy, 1992

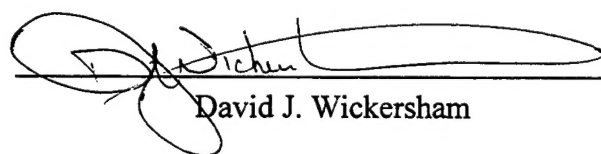
Submitted in partial fulfillment of the
Requirements for the degree of

MASTER OF SCIENCE IN APPLIED PHYSICS

from the

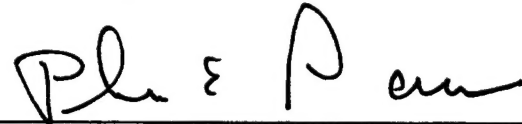
NAVAL POSTGRADUATE SCHOOL
March 2000

Author:



David J. Wickersham

Approved by:



Phillip E. Pace, Thesis Advisor



D. Scott Davis, Co-advisor



William B. Maier, Chairman

Department of Physics

ABSTRACT

To reduce the number of phase sampling comparators in a direction finding (DF) interferometer antenna, a new array based on a robust symmetrical number system (RSNS) is described. The RSNS is used to decompose the spatial filtering operation into a number of parallel sub-operations that are of smaller computational complexity. Each sub-operation (interferometer) symmetrically folds the phase with folding period equal to $2Nm_i$ where N is the number of channels that are used and m_i is the channel modulus. A small comparator ladder mid-level quantizes each folded phase response. Each sub-operation only requires a precision in accordance with that modulus. A much higher DF resolution is achieved after the N different RSNS moduli are used and the results of these low precision sub-operations are recombined. The parallel use of phase waveforms increases the antenna resolution without increasing the folding rate of the system. The new antenna is constructed and tested in an anechoic chamber, and the results are compared with the experimental results of a previously tested optimum symmetrical number system (OSNS) array. Although the dynamic range of the RSNS is somewhat less than the OSNS, the inherent Gray code properties make it attractive for error control in phase sampling interferometry.

TABLE OF CONTENTS

I.	INTRODUCTION.....	1
A.	PHASE SAMPLED INTERFEROMETRY	1
B.	PRINCIPAL CONTRIBUTIONS.....	3
C.	THESIS OUTLINE.....	4
II.	PHASE SAMPLED INTERFEROMETRY.....	7
A.	DIRECTION FINDING SYSTEMS.....	7
B.	PHASE COMPARISION SYSTEM	8
III.	OPTIMUM SYMMETRICAL NUMBER SYSTEM	
	DIRECTION FINDING ANTENNAS	15
A.	OPTIMUM SYMMETRICAL NUMBER SYSTEM.....	15
B.	OSNS ANTENNA ARCHITECTURE.....	16
C.	EXPERIMENTAL RESULTS.....	18
IV.	ROBUST SYMMETRICAL NUMBER SYSTEM	
	DIRECTION FINDING ANTENNAS	23
A.	ROBUST SYMMETRICAL NUMBER SYSTEM.....	23
B.	RSNS ANTENNA DESIGN	25
C.	COMPARATOR THRESHOLDS.....	26
D.	CHANNEL PHASING	27
E.	MAPPING RSNS DIGITAL OUTPUT TO ANGLE OF ARRIVAL.....	31
F.	SCALE FACTOR AND MAPABLE FIELD OF VIEW	36
V.	PROTOTYPE DESIGN AND PREDICTED RESULTS.....	41
A.	DETERMINATION OF MODULUS AND DYNAMIC RANGE	41
B.	FOLDING WAVEFORMS	45
C.	ELEMENT SPACING.....	48
D.	TRANSFER FUNCTION.....	49
E.	MUTUAL COUPLING	55

VI. RSNS HARDWARE DESIGN.....	59
A. ANALOG CIRCUIT COMPONENTS.....	59
B. DIGITAL CIRCUIT COMPONENTS	66
VII. TEST AND EVALUATION OF PROTOTYPE HARDWARE.....	81
A. ANECHOIC CHAMBER AND TEST PROCEDURE	81
B. UNSCALED ANTENNA RESULTS.....	86
C. SCALED ANTENNA RESULTS	91
D. DUMMY ELEMENT INFLUENCE ON MUTUAL COUPLING	94
E. THREE CHANNEL SCALED ANTENNA RESULTS	99
VIII. CONCLUSIONS	103
A. PROTOTYPE OUTPUT.....	103
B. FUTURE WORK.....	107
C. CONCLUDING REMARKS	111
APPENDIX A. MATLAB SIMULATION AND DATA EVALUATION CODE....	113
APPENDIX B. LABVIEW VI CODE.....	139
APPENDIX C. THREE CHANNEL RSNS ARRAY DESIGN RESULTS.....	147
LIST OF REFERENCES.....	151
INITIAL DISTRIBUTION LIST	153

LIST OF FIGURES

Figure 2-1.	Two Element Interferometry.....	9
Figure 2-2.	Mixer Output Voltage Versus Phase Difference, $d = \lambda/2$	11
Figure 2-3.	Mixer Output Voltage Versus Angle of Incidence $d = \lambda/2$	11
Figure 2-4.	Mixer Output Voltage Versus Angle of Arrival for $d = 7.5\lambda$	12
Figure 3-1.	Symmetrical Folding Waveform for OSNS $m_1=5$ and $m_2=6$	16
Figure 3-2.	Optimum Symmetrical Number System Antenna Architecture	17
Figure 3-3.	Comparison of Measured and Predicted Modulus 6 Mixer Output [from 10]	20
Figure 3-4.	Comparison of Measured and Predicted Modulus 11 Mixer Output [from 10]	20
Figure 3-5.	Simulated Transfer Function of OSNS Measured Mixer Output [from 10,11]	21
Figure 3-6.	Measured Transfer Function of OSNS Prototype Antenna [from 10, 11]	21
Figure 4-1.	Half Fold of Cosine Theta.....	26
Figure 4-2.	Modulus 3 Comparator Thresholds	27
Figure 4-3.	Phase Angle at Center of Bin 7.....	30
Figure 4-4.	Phase Corrected Folding Waveforms	30
Figure 4-5.	Active Comparators	31
Figure 4-6.	Bin Number to AOA Mapping	32
Figure 4-7.	Bin Number as a Function of Sine of Angle of Arrival	33
Figure 4-8.	Reported Angle of Arrival	35
Figure 4-9.	Quantization Error for Three Bit Resolution	35
Figure 4-10.	Effect of Three Scaling Factors as a Function of Theta.....	37
Figure 4-11.	Effect of Three Scaling Factors as a Function of Sine Theta	37
Figure 4-12.	Determination of Maximum Mapable Aperture	38
Figure 4-13.	Transfer Function with Scale Factor $\sqrt{3}/2$	39
Figure 4-14.	Unscaled Antenna Transfer Function	39

Figure 5-1.	Block Diagram of the Unscaled RSNS Antenna	41
Figure 5-2.	Vectors around Broadside.....	45
Figure 5-3.	Folding Waveforms for Unscaled Prototype Array	46
Figure 5-4.	Comparator States for Unscaled Prototype Array	47
Figure 5-5.	Folding Waveforms for the Scaled Prototype Array	47
Figure 5-6.	Comparator States for the Scaled Prototype Array.....	48
Figure 5-7.	Unscaled Antenna Map of Angle of Arrival to Bin Number.....	50
Figure 5-8.	Scaled Antenna Map of Angle of Arrival to Bin Number	50
Figure 5-9.	Unscaled Antenna Transfer Function	51
Figure 5-10.	Scaled Antenna Transfer Function.....	52
Figure 5-11.	Bin Population of the Unscaled Antenna.....	53
Figure 5-12.	Bin Population of the Scaled Antenna.....	53
Figure 5-13.	Quantization Error in Estimated Angle of Arrival for Unscaled Antenna	54
Figure 5-14.	Quantization Error in Estimated Angle of Arrival for Scaled Antenna....	55
Figure 5-15.	Predicted Mutual Coupling Phase Error for the Unscaled Antenna	57
Figure 5-16.	Unscaled RSNS Array with One Pair of Dummy Elements.....	57
Figure 5-17.	Simulated Mutual Coupling Phase Error of the Unscaled Antenna with Dummy Elements	58
Figure 6-1.	Analog Circuit Diagram Showing Scaled Element Spacings	60
Figure 6-2.	Stripline Element Construction.....	61
Figure 6-3.	Stripline Element Array Isometric	61
Figure 6-4.	Stripline Antenna Elements Array	62
Figure 6-5.	Scaled Array Mounted on Antenna Pedestal	62
Figure 6-6.	Stripline Antenna Element Patterns	63
Figure 6-7.	Cascaded Amplifier Pairs.	64
Figure 6-8.	Digital Circuit Diagram	67
Figure 6-9.	RSNS Modulus 17 Digital Circuit	68
Figure 6-10.	RSNS Modulus 8 Digital Circuit	68
Figure 6-11.	Shift and Bias Weighted Summing Amplifier.....	70

Figure 6-12.	Shift and Bias Inverting Amplifier	71
Figure 6-13.	Comparator Schematic and Pin-Out Diagram	72
Figure 6-14.	Voltage Divider Circuit.....	74
Figure 6-15.	Schematic Diagram of Mod 17 Comparator Output to EEPROM#2 Input.....	78
Figure 6-16.	Schematic Diagram of EEPROM#2 to DIO Board Wiring	79
Figure 7-1.	Anechoic Chamber Configuration	82
Figure 7-2.	Anechoic Chamber Control and Recording Equipment	83
Figure 7-3.	Data Collection Flow Chart	84
Figure 7-4	Unscaled Antenna, Modulus 8 Normalized Phase Detector Output.....	87
Figure 7-5.	Unscaled Antenna, Modulus 17 Normalized Phase Detector Output.....	87
Figure 7-6.	Phase Difference between Simulated and Measured Waveforms, Unscaled Antenna	88
Figure 7-7.	Measured Phase Detector Output through Simulated Digital Circuit.....	88
Figure 7-8.	Unscaled Antenna, Shift and Bias Circuit Output	89
Figure 7-9.	Bin Mapping of Unscaled Antenna.....	89
Figure 7-10.	Transfer Function of Unscaled Antenna.....	90
Figure 7-11.	Scaled Antenna, Modulus 8 Phase Detector Output.....	92
Figure 7-12.	Scaled Antenna, Modulus 17 Phase Detector Output.....	92
Figure 7-13.	Phase Difference between Simulated and Measured Waveforms, Scaled Antenna	93
Figure 7-14.	Measured Phase Detector Output passed through Simulated Digital Circuit	93
Figure 7-15.	Shift and Bias Output, Scaled Antenna.....	94
Figure 7-16.	Scaled Antenna Bin Mapping	94
Figure 7-17.	Scaled Antenna Transfer Function.....	95
Figure 7-18.	Scaled Array Construction with Dummy Elements.....	96
Figure 7-19.	Phase Error Results with No Dummy Elements Installed	97
Figure 7-20.	Phase Error Results with One Pair of Dummy Elements Installed.....	97

Figure 7-21.	Phase Error Results with Two Pair of Dummy Elements Installed	98
Figure 7-22.	Normalized Measured Phase Detector Output, Three Channel Array, Modulus 6	100
Figure 7-23.	Normalized Measured Phase Detector Output, Three Channel Array, Modulus 11	100
Figure 7-24.	Normalized Measured Phase Detector Output, Three Channel Array, Modulus 17	101
Figure 7-25:	Three Channel Array Measured Phase Detector Output Processed by Simulated Digital Circuit.....	101
Figure 8-1.	Simulated Transfer Function of the Unscaled Prototype Array.....	103
Figure 8-2.	Measured Transfer Function of the Unscaled Prototype Array	104
Figure 8-3.	Simulated Transfer Function of the Scaled Prototype Array	105
Figure 8-4.	Measured Transfer Function of the Scaled Prototype Array	105
Figure 8-5.	Transfer Function for Design Frequency	108
Figure 8-6.	Transfer Function for Half Design Frequency	109
Figure 8-7.	Transfer Function for Twice Design Frequency	109
Figure 8-8.	Possible Four Channel Geometry	110
Figure B-1.	Configuration to Link Devices Using a GPIB Cable [from 16]	139
Figure B-2.	A GPIB Connector Showing Signal Assignment [from 16].....	140
Figure B-3.	Front Panel	142
Figure B-4.	Writes Command String to the GPIB Device (Multimeter)	143
Figure B-5.	Frame 1 Waits for GPIB to Assert SRQ. Frame 2 Reads Measurement from Multimeter.....	144
Figure B-6.	Clears the SRQ Mode to be Ready for the Next Request.....	145
Figure C-1.	Three Channel RSNS Prototype Array Geometry	147
Figure C-2.	Folding Waveform for Three Channel Array Modulus 6	148
Figure C-3.	Folding Waveforms for Three Channel Array Modulus 11.....	149
Figure C-4.	Folding Waveforms for Three Channel Array Modulus 17.....	145

Figure C-5. Bin Mapping of RSNS 3 Channel Prototype Array.....145

LIST OF TABLES

Table 3-1. Several OSNS Arrays Possessing the Same Spatial Resolution ($M = 60$)	18
Table 4-1. Vector Series for Two Channel RSNS, Modulus 3 and 4	25
Table 4-2. Dynamic Range of RSNS System, Modulus 3 and 4	28
Table 5-1. Moduli 8 and 17 Vector Sequence	43
Table 5-2. Modulus 8 and 17 Comparator Thresholds	44
Table 5-3. Element Spacing for the Prototype Antenna Arrays	49
Table 6-1. Cascaded Amplifier Pairs with Saturation Data	64
Table 6-2. Voltage Divider Calculations	75
Table 6-3. Thermometer Code of EEPROM Programming	77
Table 7-1. Normalized RMS Phase Error for Various Dummy Element Configurations	98

LIST OF ABBREVIATIONS, ACRONYMS, AND SYMBOLS

ADC	Analog to Digital Converter
AOA	Angle of Arrival
BW	Bin Width
d_i	Element Spacing for Element I
d'	Element Spacing for Scaled Array
∂	Forced Phase Difference
DC	Direct Current
DF	Direction Finding
DIO	Digital Input-Output card
EEPROM	Electrically Erasable Programmable Read Only Memory
f	Frequency
FM	Frequency Modulated
ϕ	Broadside Phase Difference
g	Discrete state of RSNS vector
GPIB	General Purpose Interface Bus (synonymous with HPIB)
HPIB	Hewlett-Packard Interface Bus (synonymous with GPIB)
I_j	Current through Voltage Divider Resistance of j -th Comparator
IF	Intermediate Frequency
k	Wave Number
\hat{k}	Bin Number
LNA	Low Noise Amplifier
LPF	Low Pass Filter
λ	Wavelength
M, \hat{M}	Dynamic Range for OSNS, RSNS
m, m_i	Modulus
N	Number of Channels

n_i	Number of Folds
η	Normalized Phase Detector Output
OSNS	Optimum Symmetrical Number System
PRP	Pairwise Relatively Prime
PSI	Phase Sampled Interferometry
ϕ	Wave Function of Free Space Wave
R_j	Voltage Divider Resistance of j -th Comparator
r_k	Resolution of Bin k
RDF	Radio Direction Finding
RSNS	Robust Symmetrical Number System
s_i	Channel Sequence Shift Value
SNS	Symmetrical Number System
θ	Angle of Arrival
$\hat{\theta}$	Reported Angle of Arrival (Output of SNS system)
θ'	Angle of Arrival for Scaled Array
θ_{mm}	Maximum Mapable Aperture
V	Voltage
V_j	Threshold Voltage for j -th Comparator
V_{out}	Output of Amplifier Stage
V_{thresh}	Comparator Threshold Voltage
VNA	Vector Network Analyzer
ξ	Scale Factor
ψ	Wave function at a receiving element

ACKNOWLEDGEMENTS

Clearly, I need to begin by thanking Professor Phillip Pace, my thesis advisor, whose guidance, enthusiasm and patience have made this project enjoyable. To Professor Scott Davis, thank you for your careful review of this thesis and thoughtful comments. I would also like to thank Professor David Jenn, the Microwave Laboratory Director, for his insight and analysis and for loaning space in the lab for all of the antenna hardware. Next, I need to thank Bob Vitale whose microwave experience and knowledge, as well as a few very late nights, made is project work. Thank you Professor David Styer for your hard work laying the foundation on which this thesis is built. To LT Nathan York, my successor in RSNS research, good luck-it's all yours now! Finally, to my patient, often neglected, but never resentful wife Erin, thank you most of all.

This research was supported in part by the Tactical Electronic Warfare Division of the Naval Research Laboratory, Washington DC and the Naval Postgraduate School Center for Joint Services Electronic Warfare.

I. INTRODUCTION

A. PHASE SAMPLED INTERFEROMETRY

Direction finding (DF) systems find applications in many disciplines including geo-location, navigation, and targeting. Law enforcement officials, military personnel and wildlife managers use DF systems extensively for tracking. Radio DF systems commonly use phase sampled linear interferometer arrays to measure the direction of arrival of a single incident planar waveform in order to estimate the geographical bearing of the emitter. Each interferometer consists of two receive elements separated by a distance d (baseline). A waveform impinging on an ideal interferometer has the *same* amplitude at both element locations. Thus all of the information about the direction of arrival is contained in the phase of the signal measured by the different array elements. Consequently, most existing radio DF systems are based on phase-only measurements. As the planar waveform impinges upon the receive elements, the difference in phase is measured, and the direction of arrival is estimated. Ambiguities in the phase difference occur if the separation between interferometer elements is greater than half the electrical wavelength. These ambiguities cause ambiguous estimations of the direction of arrival.

To resolve the ambiguities, the addition of a second interferometer (third element) can be used [1,2]. Multiple baseline systems can become quite long when high resolution is required. This long baseline may be unacceptable in volume confined applications such as spacecraft, unmanned aerial vehicles, and hand held DF systems. Many alternative approaches to resolving the ambiguities within a phase sampling system have been recently investigated.

The *extended phase interferometry* technique [3,4] incorporates both calibrated phase and amplitude response data from the antenna arrays. This technique appropriately weights the square of the baseline phase differences with the antenna gains. The incorporation of amplitude data provides significant performance improvement over

phase-only interferometry; however, it requires a modest increase in computational complexity.

Pseudo Doppler techniques [5] have also been investigated in the 2-2000 MHz range to prevent ambiguities. This system employs a circular array of four omni-directional antennas. A commutation switch samples the antennas such that the resulting phase modulation on the received signal encodes the direction of arrival. As the elements are commutated a FM discriminator responds with impulses with size approximately proportional to the phase step between each element. The maximum spacing between adjacent elements is less than half a wavelength. The phase of the output is used to estimate the angle of arrival. The single channel interferometer minimizes cost and power consumption by avoiding a multitude of expensive receivers and by employing the cost-effective pseudo Doppler antenna.

The *symmetric pair antenna array* [6] provides accurate DF by means of low-resolution phase measurements, achieved by virtue of the symmetry of the array geometry. This type of array consists of pairs of antenna elements that are arranged around a common phase center. Due to symmetry, any arriving wavefront generates a phase lead at one member and a phase lag of equal magnitude at the other member of the symmetric pair. Since the polarity of the output signal is dependent on the angle of incidence, it can be used to determine the signal direction of arrival. The sign bit pattern of the pairs of a given symmetric pair array will change for different angles of incidence and, assuming an unambiguous arrangement, (annular zones on the surface of a sphere) will be distinguishable.

This thesis presents a phase sampled linear interferometer array that incorporates a robust symmetrical number system encoding. The system has no moving parts or switches. Due to the inherent Gray code (adjacent codes differ by one bit) properties, the robust symmetrical number system (RSNS) efficiently resolves the ambiguities and resists mutual coupling induced errors. RSNS is used to decompose the spatial filtering operation into a number of parallel sub-operations that are of smaller computational complexity. Each sub-operation (interferometer) symmetrically folds the phase with

folding period equal to $2Nm_i$ for the Robust Symmetrical Number System (RSNS) where N is the number of channels that are used and m_i is the channel modulus. A small comparator ladder mid-level quantizes each folded phase response. Each sub-operation only requires a precision in accordance with that modulus. The low precision demanded in each sub-operation permits the system to overcome phase errors induced by mutual coupling. A much higher DF resolution is achieved after the N different RSNS moduli are used and the results of these low precision sub-operations are recombined. The parallel use of phase waveforms increases the antenna resolution without increasing the folding rate of the system. Previous experimental results from an Optimum Symmetrical Number System (OSNS) prototype antenna revealed encoding errors at the code transition points. Although the dynamic range of the RSNS is somewhat smaller than OSNS, the inherent Gray code properties of the RSNS make it attractive for error control. A prototype RSNS system has been designed and built to investigate the effectiveness of this signal processing technique.

B. PRINCIPAL CONTRIBUTIONS

The focus of this thesis research has been to design, fabricate, and test prototype antenna arrays that investigate the performance of the RSNS architecture. This antenna is the first of its kind incorporating innovative microwave technology (stripline antenna elements), developing new digital hardware designs, and deriving unique performance equations. The antenna design results in a system that is resistant to phase errors while simultaneously providing high resolution with a minimal amount of hardware.

The design efforts were initially focused upon the phase detection process. MATLAB programs were written to simulate the design. Several array configurations were built and evaluated. MATLAB programs were also written to evaluate the experimental results. The decision to build an array with a 6-bit resolution restricted the element spacings and demanded the design and fabrication of innovative stripline dipole antenna elements and associated microwave circuits.

The sub-operations consist of mid-level quantization accomplished by parallel comparator networks. The derivation of the comparator thresholds enabled the proper

quantization to occur. The comparator networks process the folding waveform output of the phase detection circuit. The proper phase relationship between the antenna elements was derived and verified through MATLAB simulation.

The initial results from the array possessed phase errors attributed to mutual coupling between the antenna elements. A scale factor was derived and performance simulated in order to increase the element spacing and reduce the mutual coupling effects.

A hybrid of Gray code and binary EEPROM mapping enabled optimization of the digital circuit design and reduced the required number of components. A MATLAB program simulated the performance of the digital circuit.

Data processing was conducted by collecting the EEPROM output and phase detector outputs in parallel with a LABVIEW program. Over 100 patterns studied the impact of mutual coupling, antenna scaling, amplifier harmonics, and signal multi-paths.

C. THESIS OUTLINE

In Chapter II, two-element interferometry theory is reviewed. The equations governing the sampling of an incident wave front are presented and the variables that effect the output are discussed.

In Chapter III, the Optimum Symmetrical Number Systems is presented. The OSNS prototype antenna is described, and the experimental results are presented.

In Chapter IV the application of the RSNS theory to phase sampled interferometry is described.

Chapter V derives the design equations and application to the specific prototype antenna. The geometric derivations of the required phase and comparator settings are shown. The MATLAB simulations of the prototype antenna arrays are provided. The folding waveforms and transfer functions used to design the prototype are presented.

Chapter VI describes the hardware design and anechoic chamber testing procedures.

Chapter VII presents the experimental results from the prototype antenna arrays.

Chapter VIII summarizes the results and conclusions derived from the RSNS prototype antenna array. It also presents areas for further research and insights into the possible results of that research.

Appendix A presents the MATLAB codes used to design, simulate, and evaluate the RSNS antenna.

Appendix B shows the LABVIEW codes used for data collection.

Appendix C describes the array design, predicted folding waveforms, and predicted transfer function of a 3-channel RSNS antenna used to investigate the folding waveform phase errors caused by mutual coupling.

II. PHASE SAMPLED INTERFEROMETRY

A. DIRECTION FINDING SYSTEMS

Radio direction finding is a class of direction finding by which the direction to a radio source is determined by means of a radio direction finder (RDF). A RDF is a passive receiving system that measures the energy extracted from the passing electromagnetic radio wave to obtain direction-of-arrival (DOA) information.

A radio direction finding system consists of four essential functional elements [7]. The antenna extracts the electromagnetic energy and converts it to a signal containing DOA information. The receiver down-converts, amplifies, and processes the antenna signal to intermediate frequencies (IF) or baseband. The post-receiver processor further processes the signal to obtain the DOA information. The DF information processing-read-out-display unit prepares the basic DOA data for transmission to users of the DF information. The antenna is the key subsystem in a RDF. It extracts energy from the incident electromagnetic field and provides output signals containing the incident energy DOA information [8].

At microwave frequencies, antennas typically have aperture sizes of several wavelengths. Small aperture RDFs determine direction-of-arrival information by one of the following three measurement methods [7]:

1. Amplitude response,
2. Phase difference,
3. Time delay.

More specifically, small aperture DF systems may be separated into four functional categories based on the fundamental measurement methods presented above. The four basic categories are as follows [7]:

Category I: Systems using either direct or comparative amplitude response of the antenna subsystem for DOA information.

Category II: Systems using the phase difference between disposed antenna elements with the phase differential converted to amplitude DOA information.

Category III: Systems using the phase difference between disposed antenna elements for DOA information.

Category IV: Systems using the time-of-arrival difference between disposed antenna elements for DOA information.

The RSNS antenna investigated in this thesis falls into Category III.

B. PHASE COMPARISON SYSTEM

A two-element linear interferometer is shown in Figure 2 - 1. The two antenna elements are spaced a distance d apart, and the incident plane wave arrives with bearing angle θ . In this phase monopulse configuration the angle θ is measured from the perpendicular to the baseline axis and can take on values $\pi/2 > \theta > -\pi/2$. The electromagnetic wave arrives first at antenna element 1 located at $x = d/2$. Without loss of generality, the phase of the wave arriving at the first element at time t is $\psi_1 = 2\pi ft$. The plane wave arrives at antenna element 2 (located at $x = -d/2$) after traveling an additional distance of $d \sin(\theta)$. The phase of the wave arriving at the second element is then

$$\psi_2 = 2\pi ft - \frac{2\pi}{\lambda} d \sin(\theta). \quad (2.1)$$

The phase difference between the two elements is

$$\Delta\psi = \psi_1 - \psi_2 = \frac{2\pi}{\lambda} d \sin(\theta_B) = kd \sin(\theta), \quad (2.2)$$

where k is the wave number, is a function of the incidence angle of the wave.

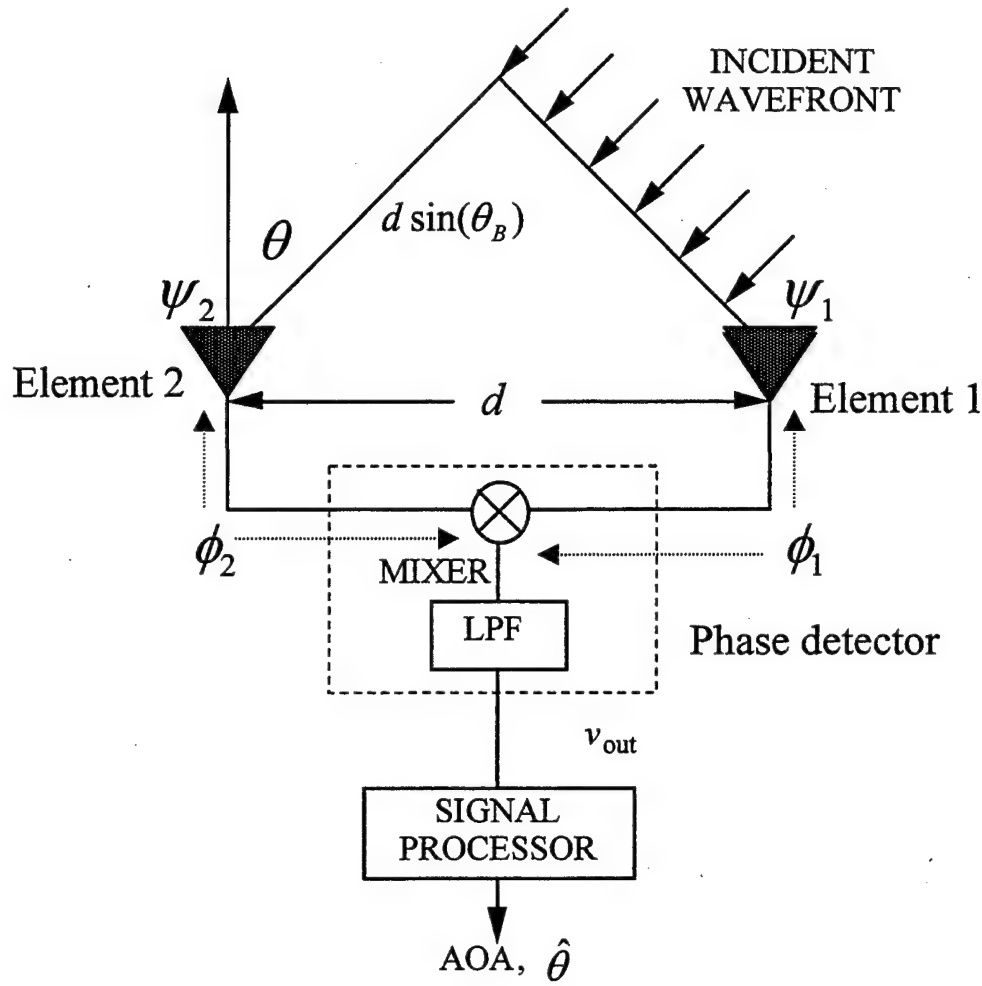


Figure 2 - 1: Two-Element Interferometry.

The signals received by the antenna elements are phase detected (multiplied together and processed by a lowpass filter) resulting in an output signal whose frequency is the difference between the two input signal frequencies. Because the signals have the same frequency, the mixer output is a DC voltage whose value is proportional to the difference between signal phases ψ_1 and ψ_2 . This difference is not purely $\Delta\psi$ because of the time delays due to the different transmission line lengths from each antenna element. However, these line lengths are known and defined as ϕ_1 and ϕ_2 . The phase

error due to the line length differences is $\phi = \phi_1 - \phi_2$ and can be compensated for in the angle estimate. Let the signals from the two antenna elements be

$$v_1(t) = V \cos[\psi_1 + \phi_1(t)] \quad (2.3)$$

and

$$v_2(t) = V \cos[\psi_2 + \phi_2(t)], \quad (2.4)$$

where V is the maximum value of the voltage at the antenna elements. The lowpass mixer output voltage is

$$v_{out} = \frac{V^2}{2} \cos(\Delta\psi + \phi) = \frac{V^2}{2} \cos(kd \sin(\theta) + \phi) \quad (2.5)$$

which contains the plane wave angle of arrival (AOA) information. For values of $d = \lambda/2$, $\phi = 0$, and $\Delta\psi = \pi \sin(\theta)$, as the AOA θ varies from $-\pi/2$ to $\pi/2$, the phase difference $\Delta\phi$ varies from $-\pi$ to π as shown in Figure 2 - 2. The output voltage from the phase detector is also a function of the phase difference and is a symmetrical folding waveform. Together these relationships give the phase detector output voltage as a symmetrical function of the AOA as shown in Figure 2 - 3 for $d = \lambda/2$.

Ambiguities are generated for baselines where $d > \lambda/2$. That is, the phase detector output voltage is highly ambiguous with a single phase corresponding to many angles of arrival. The number of folding periods n that occur within an AOA of π radians is

$$n = \frac{2d}{\lambda}. \quad (2.6)$$

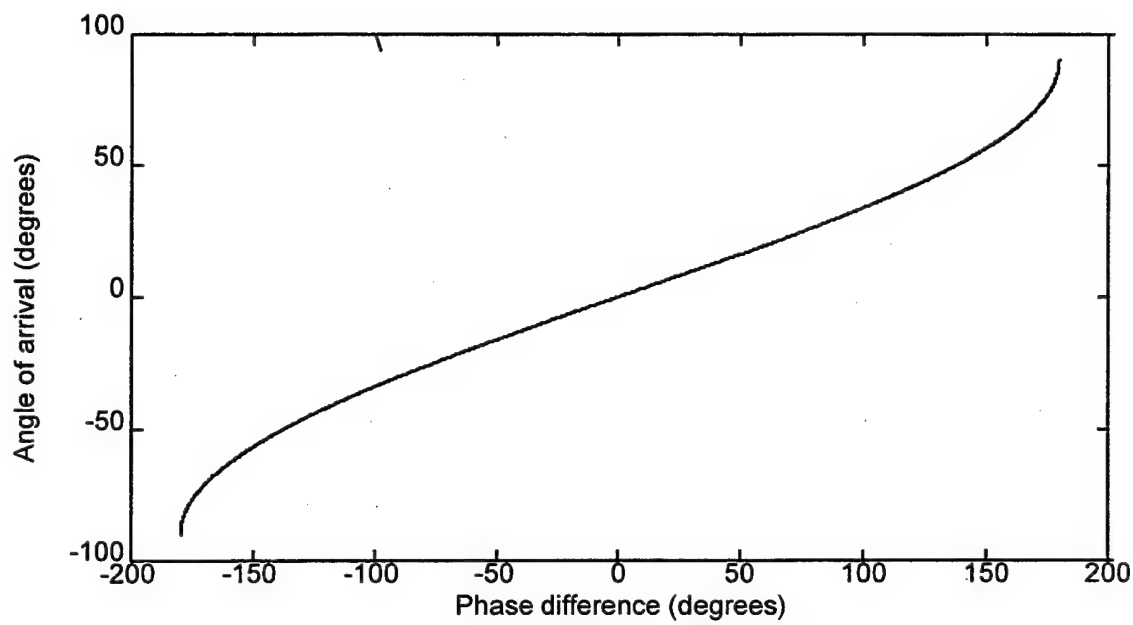


Figure 2 - 2: Mixer Output Voltage Versus Phase Difference, $d = \lambda /2$.

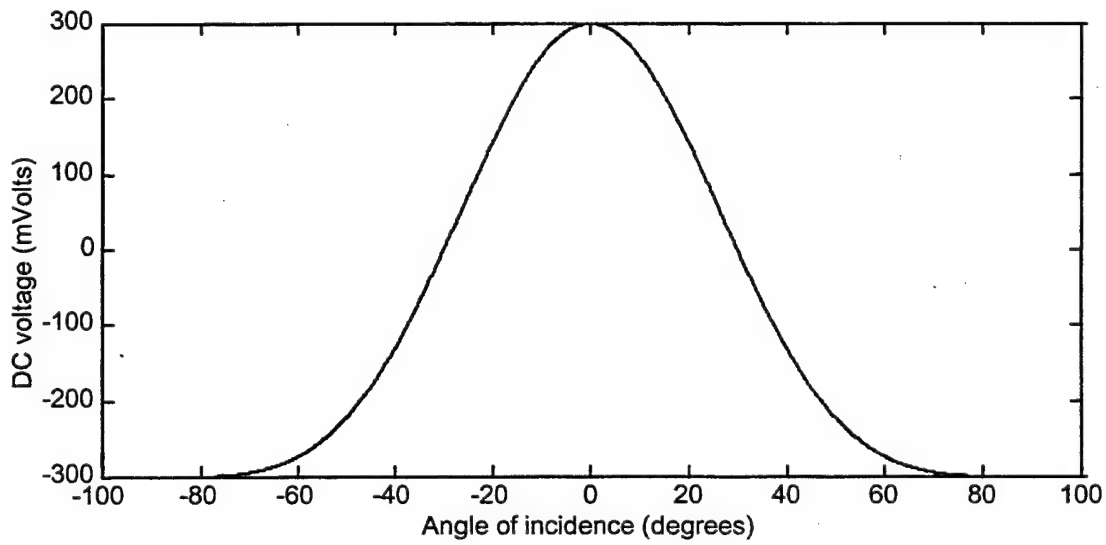


Figure 2 - 3: Mixer Output Voltage Versus Angle of Incidence, $d = \lambda /2$.

For example, with $d = 7.5\lambda$, $n=15$ folds are available as shown in Figure 2 - 4. The folding period is not constant but grows larger in proportion to the off-perpendicular angle θ because of the $\sin(\theta)$ dependence in (2.5).

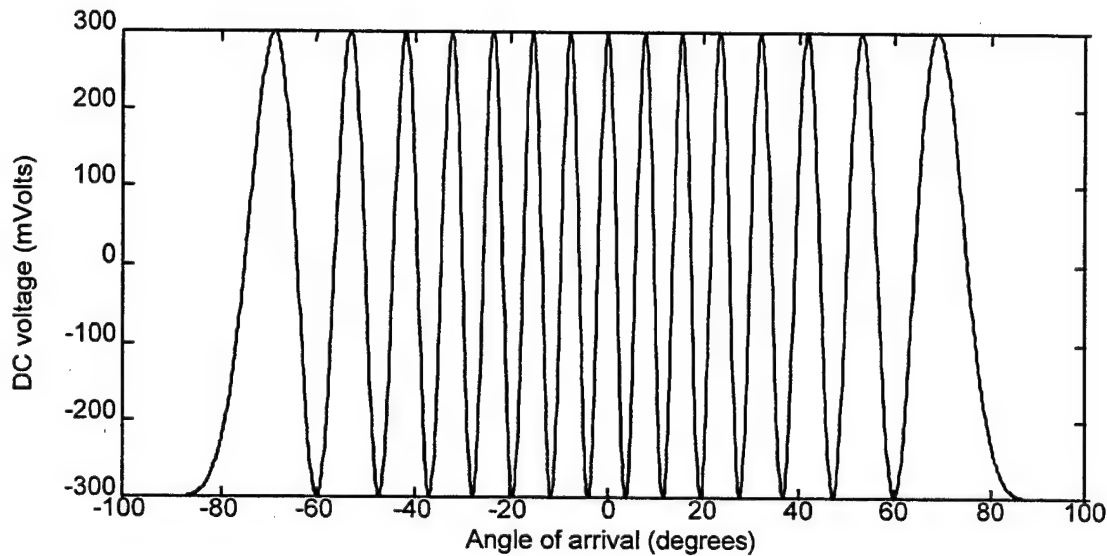


Figure 2 - 4: Mixer Output Voltage Versus Angle of Arrival for $d = 7.5\lambda$.

The ambiguities within the symmetrical folding waveforms represent the phase difference between the elements and can be resolved by using additional interferometers in the linear array. Typically, each interferometer in the linear array symmetrically folds the phase response with the folding period between interferometers being a successive factor of two, or $d_4 = 2d_3 = 4d_2 = 8d_1$. High-speed binary comparators are used to produce a digital output. The folding waveforms are shifted appropriately using a phase shifter in each channel to achieve a Gray code result. The folded output from each phase detector is then quantized with a single comparator with a normalized threshold level $T=0.5$. Together, the comparator outputs directly encode the signal's AOA in the Gray code format. This approach makes use of the periodic dependence of the interferometer's phase response on the applied plane wave's AOA and the distance between the elements

of each interferometer. One of the major limitations associated with this approach is the achievable resolution. For each folding period to be a factor of two longer than its predecessor, the distance between the elements must also be doubled. That is, an 8-bit DF antenna using the previous scheme would require element spacings $\lambda/4, \lambda/2, \lambda, 2\lambda, 4\lambda, \dots, 32\lambda$ with a total baseline length of 32λ . This distance doubling of the element spacings requires complex analog hardware, adversely affects the physical implementation of the DF architecture, and ultimately constrains the achievable resolution.

III. OPTIMUM SYMMETRICAL NUMBER SYSTEM DIRECTION FINDING ANTENNAS

A. OPTIMUM SYMMETRICAL NUMBER SYSTEM

Incorporation of the optimum symmetrical number system (OSNS) encoding overcomes the major limitations of the binary encoding approach and provides an efficient method to enhance the resolution of the array while minimizing the total hardware baseline.

The OSNS is composed of a number of pairwise relatively prime (PRP) moduli m_i . The integers within each OSNS modulus are representative of a symmetrically folded waveform with the period of the waveform equal to twice the modulus, i.e., $2m_i$ [9]. For m given, the integer values within twice the individual modulus are defined by the row vector

$$\bar{x}_m = [0, 1, \dots, m-1, m-1, \dots, 1, 0]. \quad (3.1)$$

Figure 3 - 1 shows part of the OSNS folding waveforms and the integer values within the modulus for $m_1=5$ and $m_2=6$. The horizontal axis represents the normalized input. The vertical lines represent folding waveform reference levels. The numbers in squares at the top of the figure represent the number of reference levels that are crossed by the folding waveform for a given input value and correspond to the row vector \bar{x}_m . The period of one complete fold is equal to $2m_1 = 10$ and $2m_2 = 12$.

Due to the presence of ambiguities, the integers within the vector (3.1) do not form a complete system of length $2m$ by themselves. The ambiguities that arise within the modulus are resolved by considering the paired values from all channels together. If N pairwise relatively prime moduli are used, the *dynamic range* (the number of unambiguous vectors) of this scheme is [10]:

$$M = \prod_{i=1}^N m_i . \quad (3.2)$$

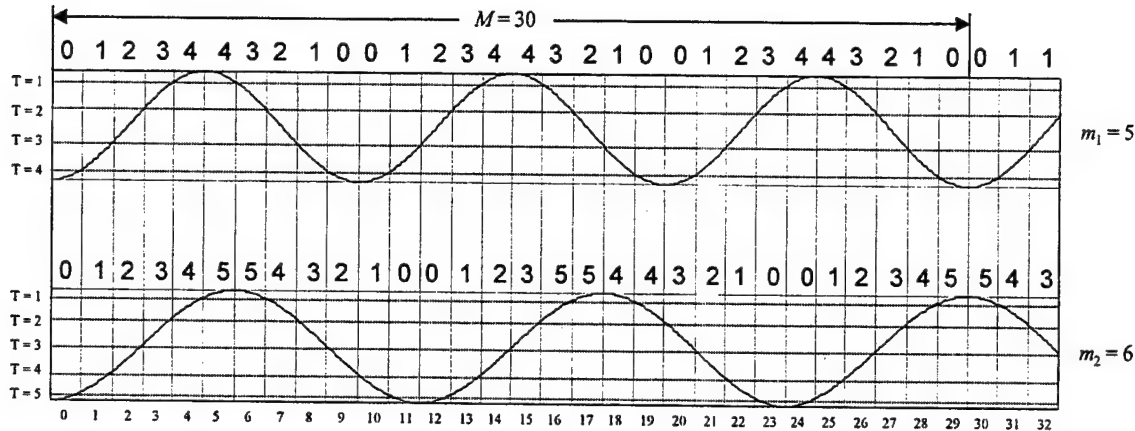


Figure 3 - 1: Symmetrical Folding Waveform for OSNS $m_1=5$ and $m_2=6$.

This dynamic range is also the position of the first repetitive moduli vector. As shown in Figure 3 - 1, the dynamic range for the $m_1 = 5$ and $m_2 = 6$ case is $M=30$. That is, no set appears twice for a normalized input in the range [0,29].

B. OSNS ANTENNA ARCHITECTURE

Figure 3 - 2 shows the schematic diagram of a $N=2$ channel OSNS DF antenna. The array consists of three elements, with both channels sharing a common element. With the correct distances between elements, each interferometer folds the phase response at $2m_i$. The phase response from each channel is quantized using m_i-1 comparators. The integers shown at each step on Figure 3 - 1 represent the number of comparators ON due to the phase voltage exceeding the comparator matching threshold voltage.

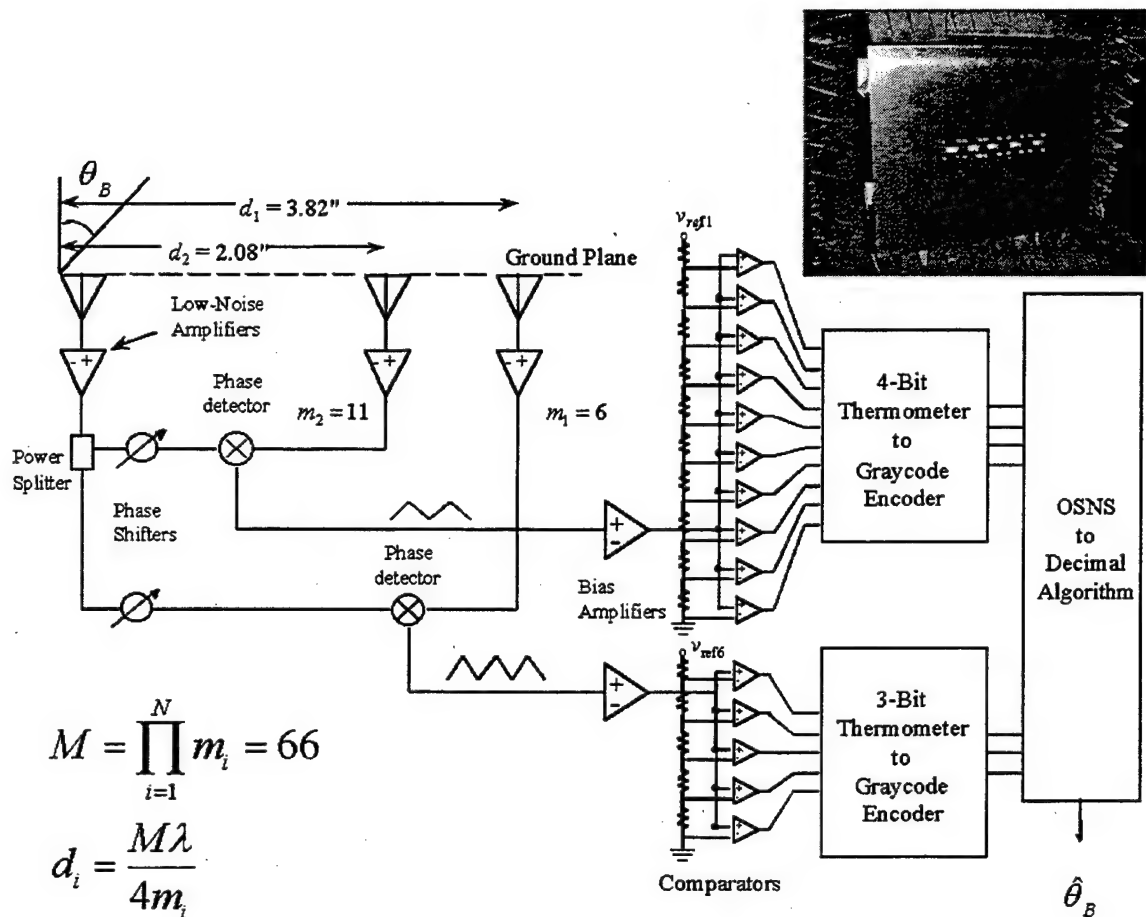


Figure 3 - 2: Optimum Symmetrical Number System Antenna Architecture.

The distance between each pair of elements is a function of the modulus, m_i . The phase response must have the correct number of folds to cover the dynamic range. For a given modulus m_i , the number of folds within the dynamic range is

$$n_i = M / 2m_i. \quad (3.3)$$

Since each fold of the array corresponds to a change in phase of π for $d = \lambda/2$, the required spacing between the reference element and the respective element of channel i is given by

$$d_i = n_i \frac{\lambda}{2} = \frac{M\lambda}{4m_i}. \quad (3.4)$$

The bin widths are uniform in size in $\sin(\theta)$ space with a width $2/M$. The spatial resolution will be derived for Equation (4.18) and is given by:

$$r_{\hat{k}} = \arcsin\left(\frac{2\hat{k} - M + 2}{M}\right) - \arcsin\left(\frac{2\hat{k} - M}{M}\right), \quad (3.5)$$

where $\hat{k} \in \{0, 1, \dots, M-1\}$ and $\hat{k} = 0$ is the bin that starts at $\theta = -\pi/2$. Note that the spatial resolution is not uniform over the range of $-\pi/2$ to $\pi/2$. The resolution is finest at broadside ($\theta = 0^\circ$) and increases with angle off broadside, because of the $\sin(\theta)$ dependence in (2.5).

In some applications element placement at certain locations on a platform may be prohibited, in which case an alternate OSNS design could be used to provide the same unambiguous AOA resolution, using e.g., a different number of comparators, as shown in Table 3 - 1. When the channels are recombined the result is a high accuracy unambiguous estimate of the AOA.

OSNS Moduli	Element Spacings	Comparators Required
$m_1 = 3, m_2 = 20$	$d_1 = 5\lambda, d_2 = 0.75\lambda$	21
$m_1 = 4, m_2 = 15$	$d_1 = 3.75\lambda, d_2 = 1\lambda$	17
$m_1 = 5, m_2 = 12$	$d_1 = 3\lambda, d_2 = 1.25\lambda$	15
$m_1 = 3, m_2 = 4$ $m_3 = 5$	$d_1 = 5\lambda, d_2 = 3.75\lambda$ $d_3 = 3\lambda$	9

Table 3 - 1: Several OSNS Arrays Possessing the Same Spatial Resolution ($M = 60$).

C. EXPERIMENTAL RESULTS

An OSNS array based on the moduli $m_1 = 6$ and $m_2 = 11$ was designed, fabricated and tested at a frequency 8.5 GHz [11]. The radiating elements are open-ended

waveguides as shown in Figure 3 - 2. For moduli $m_1 = 6$ and $m_2 = 11$, $d_1=3.82$ inches and $d_2=2.08$ inches. With $M=66$, the number of folding periods $n_1=5.5$ and $n_2=3$. To provide an adequate signal-to-noise ratio, a low-noise amplifier is included at the output of each interferometer element. Since the common element splits the signal into N paths, an attenuator is placed in the other branches to balance the amplitudes. The amplifiers operate in saturation so that the mixer input signal levels are independent of the angle of incidence. A fixed phase shifter is also included in one branch of each interferometer so that the symmetrically folded phase response waveforms from each mixer may be aligned. This alignment insures that the comparators in the digital processor properly sample the phase waveform and encode it in the OSNS.

The anechoic chamber facility at the Naval Postgraduate School was used for the antenna pattern measurements for each pair of elements. The measured mixer outputs are shown with the ideal folding waveforms in Figure 3 - 3 and Figure 3 - 4. Since the array is not useful in the endfire regions, the phase response from each channel was minimized at input AOA of -50° . This is the point where the digital code starts. Introducing the appropriate phase shifts to the signals at a point between the elements and the mixer controls the location of the voltage minima. A simulation of the transfer function for the OSNS array is shown in Figure 3 - 5. The measured transfer function (output of digital hardware) is shown in Figure 3 - 6.

The spikes in the transfer function are AOA encoding errors. The phase waveforms must cross the comparator thresholds (code transitions) at the same time across all channels. The OSNS can present a problem at each of these specific AOAs. When the set of comparators does not change state synchronously, the recovered amplitude will have a large error. Encoding errors can also occur due to imperfections in the transmission line phases. These errors however, can be isolated with additional comparators and corrected using additional circuitry as described in [9]. An alternate approach however is to develop a symmetrical number system that eliminates the possibility of this type of encoding error. That is, a symmetrical number system where only one comparator threshold is crossed at any one particular code transition.

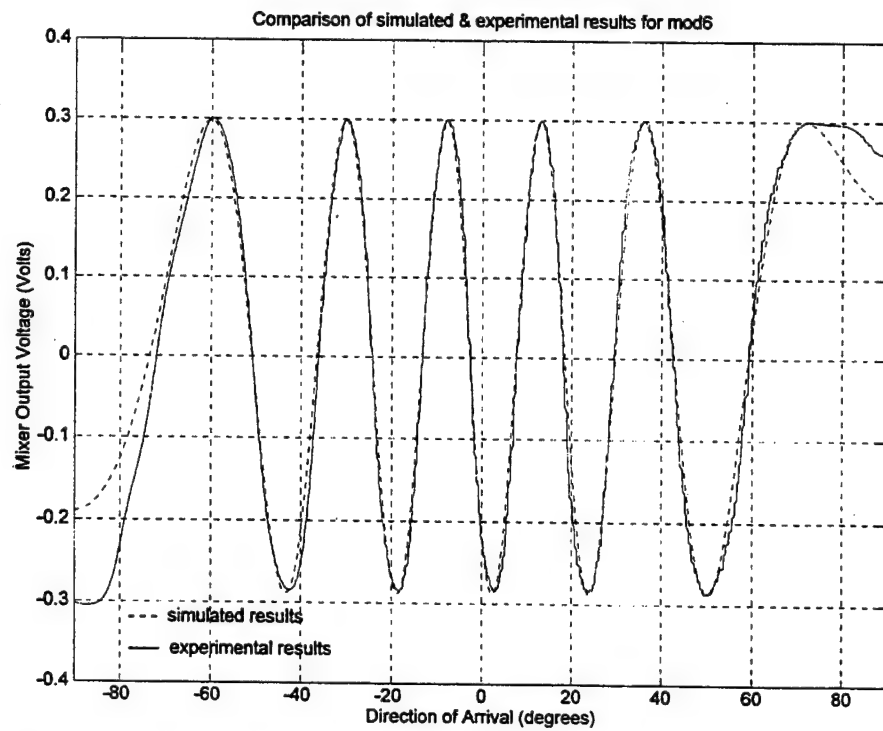


Figure 3 - 3: Comparison of Measured and Predicted Modulus 6 Mixer Output [from 10].

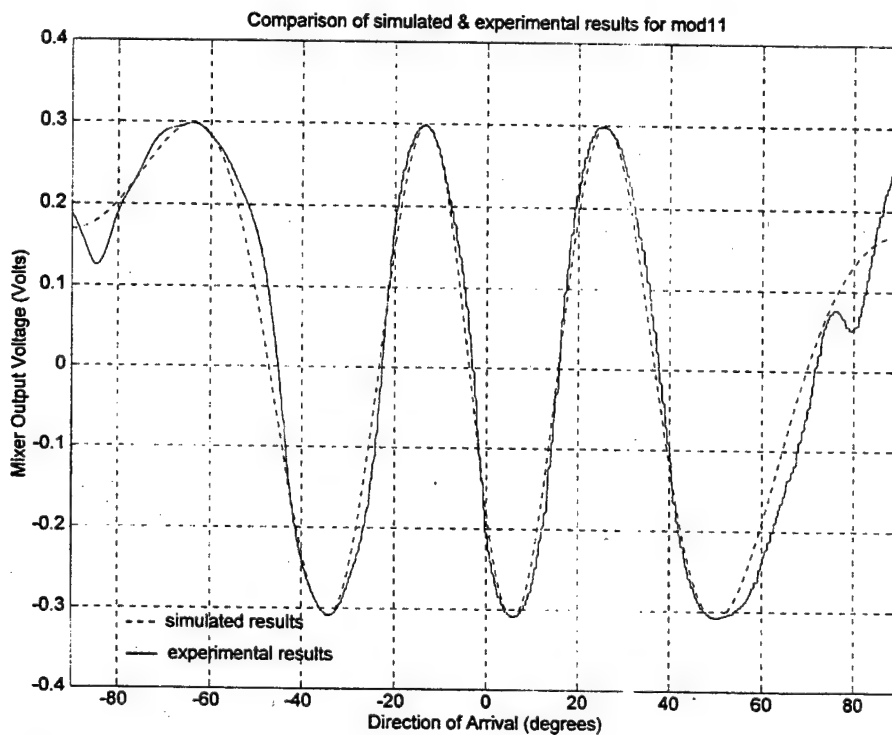


Figure 3 - 4: Comparison of Measured and Predicted Modulus 11 Mixer Output [from 10].

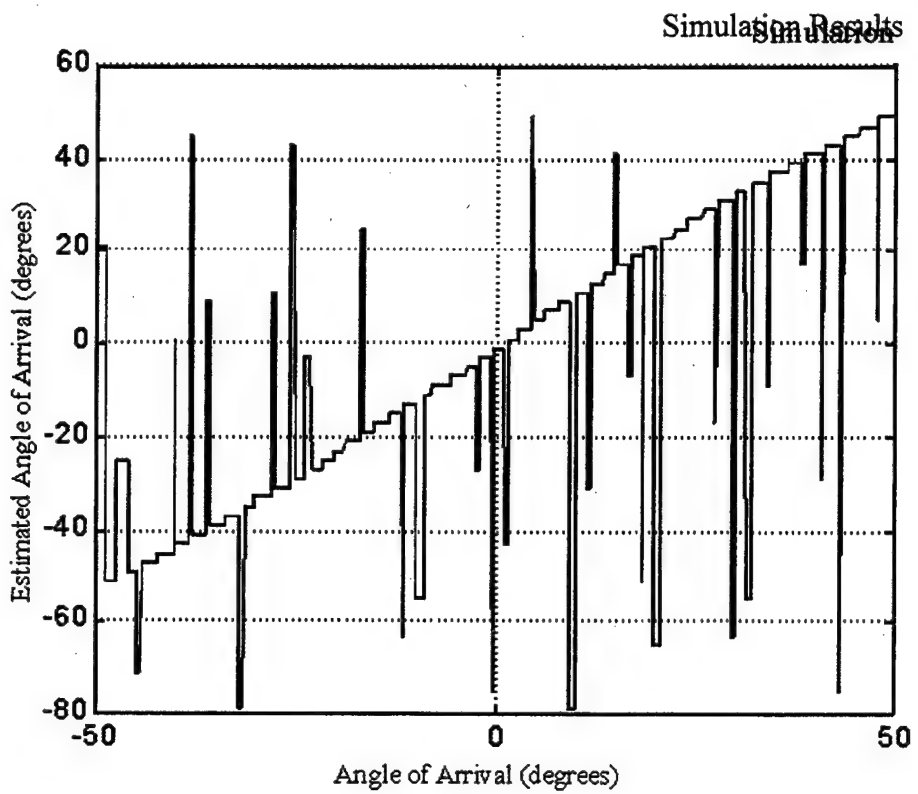


Figure 3 - 5: Simulated Transfer Function of OSNS Measured Mixer Output [from 10,11].

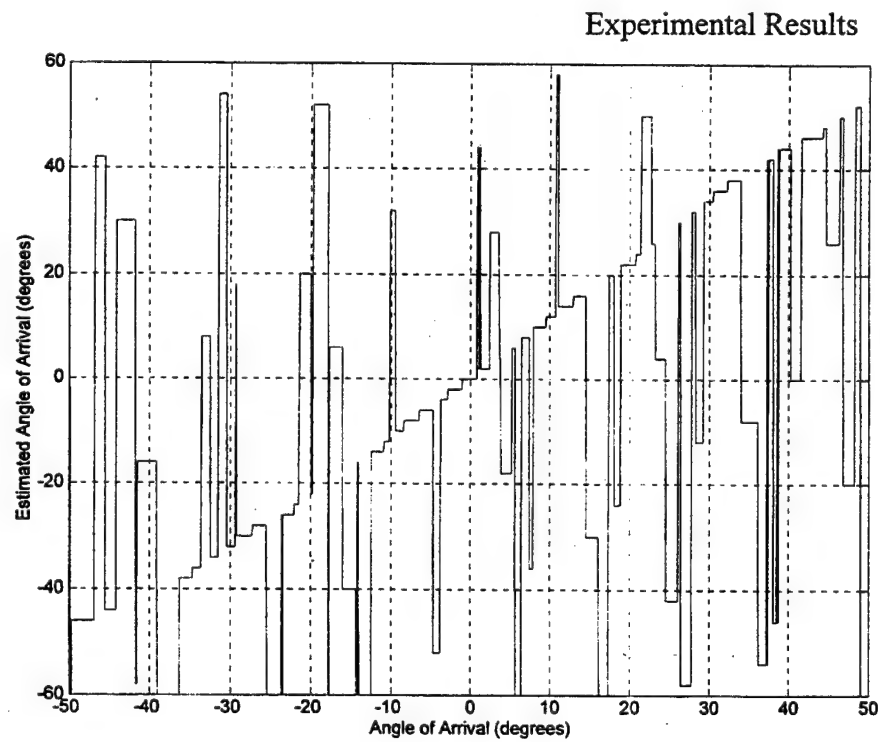


Figure 3 - 6: Measured Transfer Function of OSNS Prototype Antenna [from 10,11].

IV. ROBUST SYMMETRICAL NUMBER SYSTEM DIRECTION FINDING ANTENNAS

A. ROBUST SYMMETRICAL NUMBER SYSTEM

In the robust symmetrical number system (RSNS), N different periodic symmetrical waveforms are used with pairwise relatively prime integers m_1, m_2, \dots, m_N . The RSNS is based on the following sequence

$$x_{m1} = [0, 1, 2, \dots, m-1, m, m-1, \dots, 2, 1], \quad (4.1)$$

where x_{m1} is a row vector and m is a positive integer ($m > 0$). In an N -channel RSNS, where $N \geq 2$, the basic sequence for the i^{th} channel (modulus m) is

$$x_{m2} = [0, 0, \dots, 0, 0, 1, 1, \dots, 1, 1, \dots, m, m, \dots, m, m, \dots, 1, 1, \dots, 1, 1]. \quad (4.2)$$

In this sequence each value in the x_{m1} row vector is entered N times in succession. This sequence is repeated in both directions, forming a periodic sequence with the period

$$P_{RSNS} = 2m_i N. \quad (4.3)$$

Considering a single channel, the discrete states of the robust symmetrical number system can be expressed as [12]

$$g = \begin{cases} \left\lfloor \frac{n - s_i}{N} \right\rfloor & s_i \leq n \leq Nm_i + s_i + 1 \\ \left\lfloor \frac{2Nm_i + N - n + s_i - 1}{N} \right\rfloor & Nm_i + s_i + 2 \leq n \leq 2Nm_i + s_i - 1 \end{cases}, \quad (4.4)$$

where g is the n^{th} term of channel i , m_i is the channel modulus, s_i is a corresponding sequence shift $s_i \equiv 0, 1, 2, \dots, N-1 \pmod{N}$ and $N \geq 2$ is the number of channels in the system. The values $\{s_1, s_2, \dots, s_N\}$ must form a complete residue system modulo N . Because of the relative property of the shifts, one of the shift values will be set equal to zero. The index n corresponds to the input value. The discrete states of the RSNS are indexed using the $s_i = 0$ row vector with the index starting from the first zero. Note that the largest integer within each periodic sequence is the modulus m .

An N -channel RSNS is formed of vectors by picking N moduli m_i , and N shift values s_i , $1 \leq i \leq N$. Since the fundamental period for channel i is $2Nm_i$, the period for the RSNS vectors must be a multiple of $2Nm_i$. Therefore the *fundamental period* for the RSNS is

$$PF_{RSNS} = [2m_1N, 2m_2N, \dots, 2m_NN], \quad (4.5)$$

where $[a_1, a_2, \dots, a_N]$ is the least common multiple of a_1, a_2, \dots, a_N . From number theory [13],

$$PF_{RSNS} = 2N[m_1, m_2, \dots, m_N]. \quad (4.6)$$

The *system dynamic range* (\hat{M}_{RSNS}) of the RSNS is the maximum number of distinct vectors without a redundancy. For two channels, with the moduli separated by 1 or 2 [14],

$$\hat{M}_{RSNS} = 4m_1 + 2m_2 - 5. \quad (4.7)$$

For two channels, with the moduli separated by 3 or more,

$$\hat{M}_{RSNS} = 4m_1 + 2m_2 - 2. \quad (4.8)$$

Checking against computer results when $m_1=8$ and $m_2=17$, $\hat{M} = 64$ which fits (4.8).

B. RSNS ANTENNA DESIGN

Element spacing is a fundamental characteristic of any antenna. The RSNS architecture is capable of high resolution with very small baselines. The choice of spacing is not arbitrary; it defines the folding waveforms produced by the analog circuit. The element spacing is a function of the modulus, number of channels, dynamic range, and signal frequency. The spacing is found in three steps: determine the modulus folding period, determine the number of folds contained in the dynamic range, and factor in the frequency.

Vector	0	1	2	3	4	5	6	7	8	9	10	11	12	13	14	15	16	17	18	19	20	21
$m=3$	0	0	1	1	2	2	3	3	2	2	1	1	0	0	1	1	2	2	3	3	2	2
$m=4$	0	1	1	2	2	3	3	4	4	3	3	2	2	1	1	0	0	1	1	2	2	3

Table 4 - 1: Vector Series for Two Channel RSNS, Modulus 3 and 4.

Table 4 - 1 shows the integer values within the RSNS for $m_1=3$ and $m_2=4$. Recall from (4.3) that the folding period depends on the modulus m_i and the number of channels N and given by

$$P_{RSNS} = 2m_iN. \quad (4.9)$$

The number of folds n_i is:

$$n_i = \frac{\hat{M}}{P_{RSNS}} = \frac{\hat{M}}{2m_iN}. \quad (4.10)$$

The folds must fill the antenna's field of view (FOV). For the RSNS antenna, the FOV is 180° . In phase space, 180° corresponds to $\lambda/2$. Therefore, the required spacing, d , is

$$d_i = n_i \frac{\lambda}{2} = \frac{\hat{M}\lambda}{4m_i N}. \quad (4.11)$$

Comparing (4.11) to (3.4), for systems with the same dynamic range, the RSNS element spacing is smaller than the OSNS element spacing by a factor of N .

C. COMPARATOR THRESHOLDS

In the RSNS, m_i comparators are required for each channel. Consider the cosine of θ for $-\pi \leq \theta \leq 0$, shown Figure 4 - 1. This represents a half-fold of a folding waveform. If the folding waveform represents the modulus 3 channel of a two-channel system, the modulus 3 component of the RSNS vector string is $\{\dots 1,0,0,1,1,2,2,3,3,2,\dots\}$. The first zero and second three belong to the adjacent half-folds. This leaves six bins for this half-fold. To space the bins equally, each bin must span $\pi/6$ radians. The modulus 3 component changes when a comparator changes state. The three comparator thresholds for this case are $\cos(-\pi + \frac{\pi}{6})$, $\cos(-\pi + \frac{3\pi}{6})$, and $\cos(-\pi + \frac{5\pi}{6})$. Figure 4 - 2 shows these comparator states.

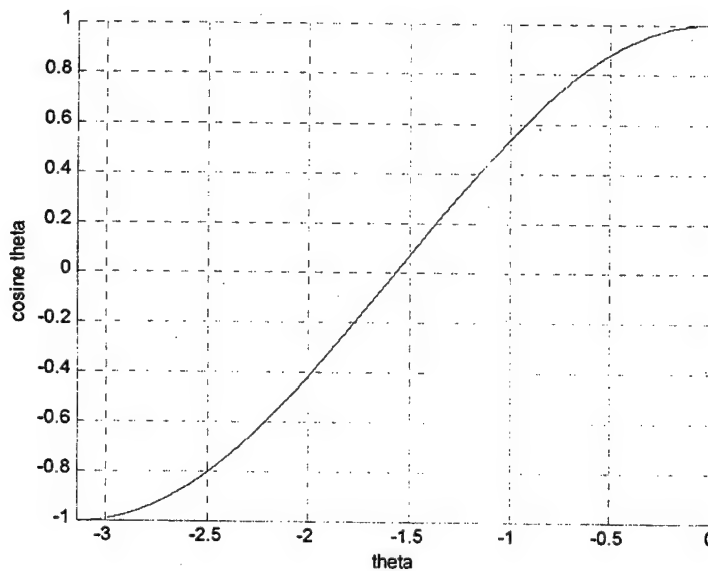


Figure 4 - 1: Half Fold of Cosine Theta.

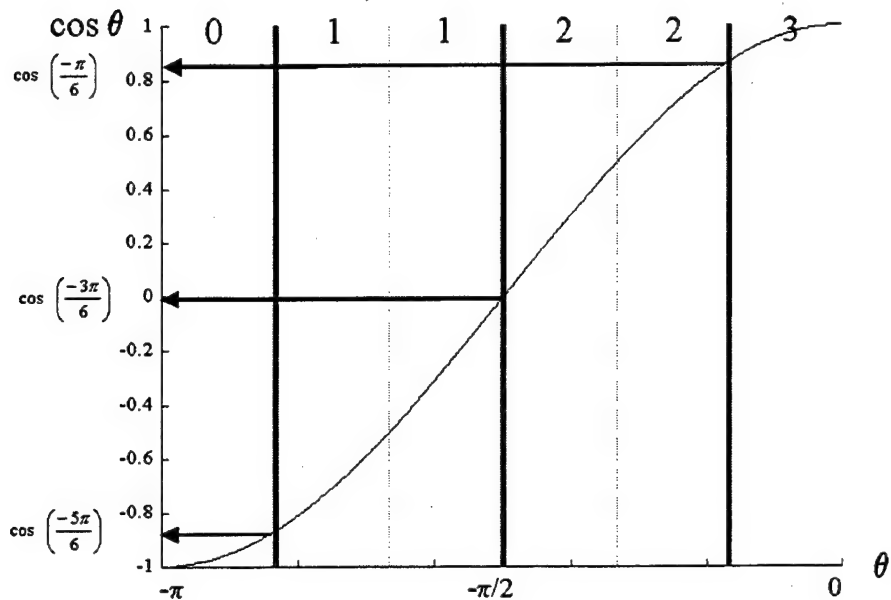


Figure 4 - 2: Modulus 3 Comparator Thresholds.

The expression for the j -th normalized comparator threshold in a modulus m_i channel is observed graphically to be:

$$V_{m_i,j} = \cos\left(\frac{(m_i - j + \frac{1}{2})}{m_i}\pi\right). \quad (4.12)$$

The comparator thresholds depend only upon the channel modulus. This powerful relationship is required prior to determining the proper phase relationships of the folding waveforms.

D. CHANNEL PHASING

A computer search algorithm determines the dynamic range of a set of moduli. Equations exist for special cases such as Equations 4.7 and 4.8. Even when the value of the dynamic range is known, the computer search algorithm is used to determine the

location of the dynamic range within the vector string [14]. For the case of $m_1=3$ and $m_2=4$, the dynamic range is 15 and falls between vectors 6 and 20 as shown in Table 4 - 2. The bin number is a re-indexing of the vector, counting the first unambiguous vector as zero.

Vector	0	1	2	3	4	5	6	7	8	9	10	11	12	13	14	15	16	17	18	19	20	21
$m=3$	0	0	1	1	2	2	3	3	2	2	1	1	0	0	1	1	2	2	3	3	2	2
$m=4$	0	1	1	2	2	3	3	4	4	3	3	2	2	1	1	0	0	1	1	2	2	3
Bin							0	1	2	3	4	5	6	7	8	9	10	11	12	13	14	

Table 4 - 2: Dynamic Range of RSNS System, Modulus 3 and 4.

The OSNS has folding waveforms that are either even or odd functions about broadside. For RSNS, the first vector is not the zero vector, and the dynamic range is not a multiple of the fundamental period. Coincidental cases of symmetry may occur in the RSNS dynamic range. This is clearly seen in Table 4 - 1, which has the dynamic range shaded. The ambiguous vectors in vectors 5, 9 and 21 delimit the dynamic range. The first vector of the dynamic range is vector 6, is (3,3). Neither modulus has symmetry about the midpoint, vector 13. The lack of symmetry in the RSNS dynamic range makes it necessary to determine this unique phase value at broadside for each channel. From (2.5) the normalized phase detector output is

$$mx(\theta) = \cos(kd \sin \theta + \phi). \quad (4.13)$$

When $\theta=0$, $\sin \theta = 0$, so $mx(\theta=0)=\cos(\phi)$. Theta equal zero corresponds to the center of Bin 7. This is broadside incidence. At the left edge of Bin 7, the folding waveform is at its minimum, and at the right edge of Bin 10, the folding waveform is at maximum. This is exactly the waveform of Figure 4 - 2.

Expanding the lower left corner of this graph, Figure 4 - 3 shows bins 7 and 8. The left edge of Bin 7 corresponds to $\phi=-\pi$ and the right edge of Bin 7 is the comparator threshold, $\phi = \frac{-5\pi}{6}$. The center of Bin 7 is midway between these angles: $\phi_3 = \frac{-11\pi}{12}$. The

sign is negative because the phase is on the negative half cycle. A similar phase determination for Modulus 4 shows the left edge of Bin 7 is at the comparator #2 threshold, which is (from Equation 4.11) $\phi = \frac{5\pi}{8}$. The right edge of Bin 8 is at the comparator #1 threshold, $\phi = \frac{7\pi}{8}$. The center of Bin 7 is one quarter of the angular distance between the thresholds, or $\phi_4 = \frac{11\pi}{16}$. The signs of these angles is positive because the folding waveform is in the decreasing half cycle. This phase difference between the elements can be inserted with a phase adjuster in the analog microwave circuit. The resulting folding waveforms with the correctly determined phases is shown Figure 4 - 4. The equations that describe the folding waveforms are:

$$mx_3(\theta) = \cos(kd_3 \sin \theta + \phi_3) = \cos\left(\frac{\pi \hat{M}}{2Nm_i} \sin \theta - \frac{11}{12}\pi\right), \quad (4.14)$$

$$mx_4(\theta) = \cos(kd_4 \sin \theta + \phi_4) = \cos\left(\frac{\pi \hat{M}}{2Nm_i} \sin \theta + \frac{11}{16}\pi\right). \quad (4.15)$$

Note that (4.14) and (4.15) are independent of frequency.

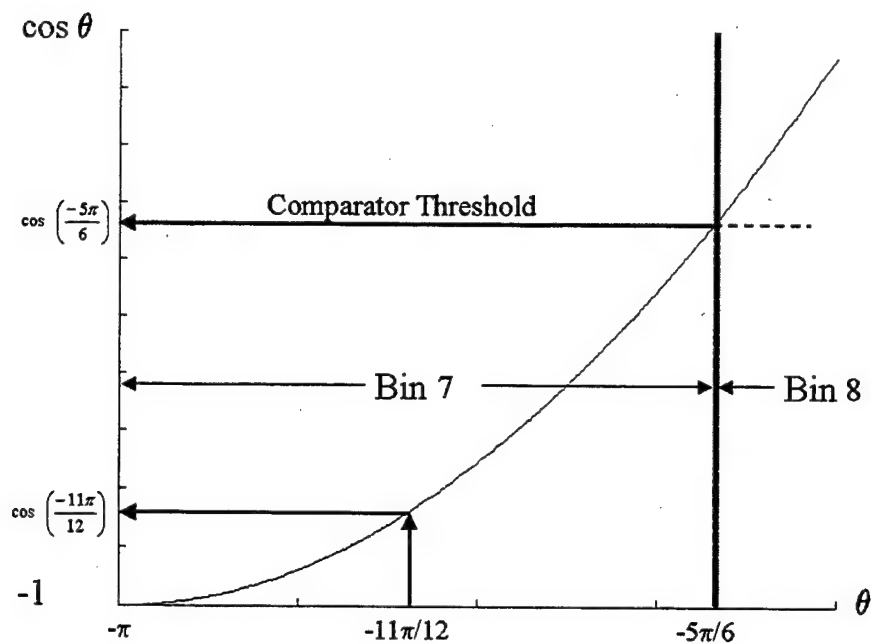


Figure 4 - 3: Phase Angle at Center of Bin 7.

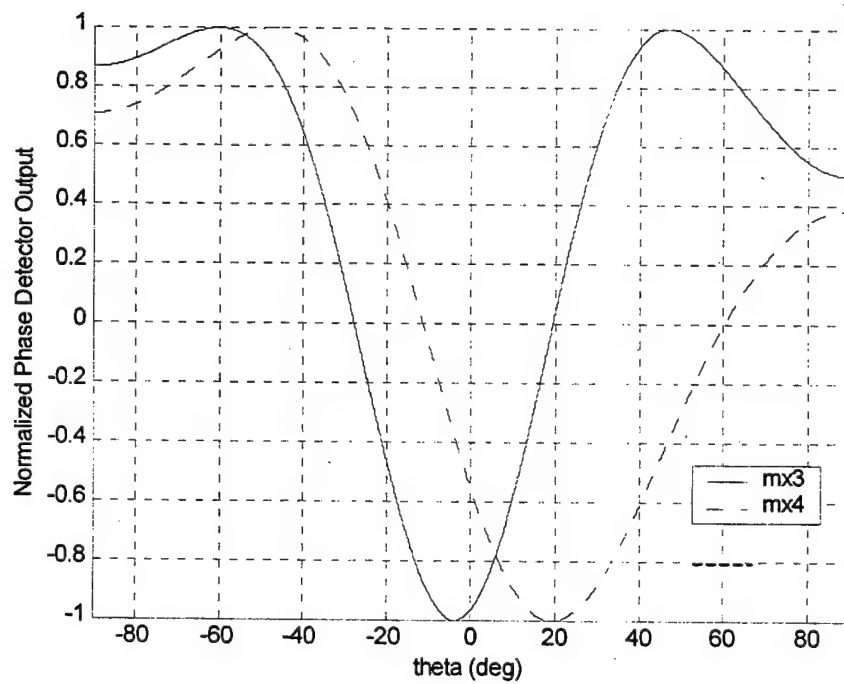


Figure 4 - 4: Phase Corrected Folding Waveforms.

E. MAPPING RSNS DIGITAL OUTPUT TO ANGLE OF ARRIVAL

Whenever a folding waveform exceeds a comparator threshold, the comparator turns ON. For the folding waveforms shown in Figure 4 - 4, the numbers of comparators in the ON state are shown in

Figure 4 - 5 (integer values within RSNS code). The active comparator map exactly matches the RSNS unambiguous vector string shown in Table 4 - 2. The dynamic range of this string falls in vectors 6-20. This is the string of vectors that are useful for DF, so those bins are indexed as shown in the bottom row of Table 4 - 2.

Re-indexing the vectors in the dynamic range with a bin number enables the RSNS code to map the AOA. The comparator states of

Figure 4 - 5 are unambiguously mapped into a bin as shown in Figure 4 - 6.

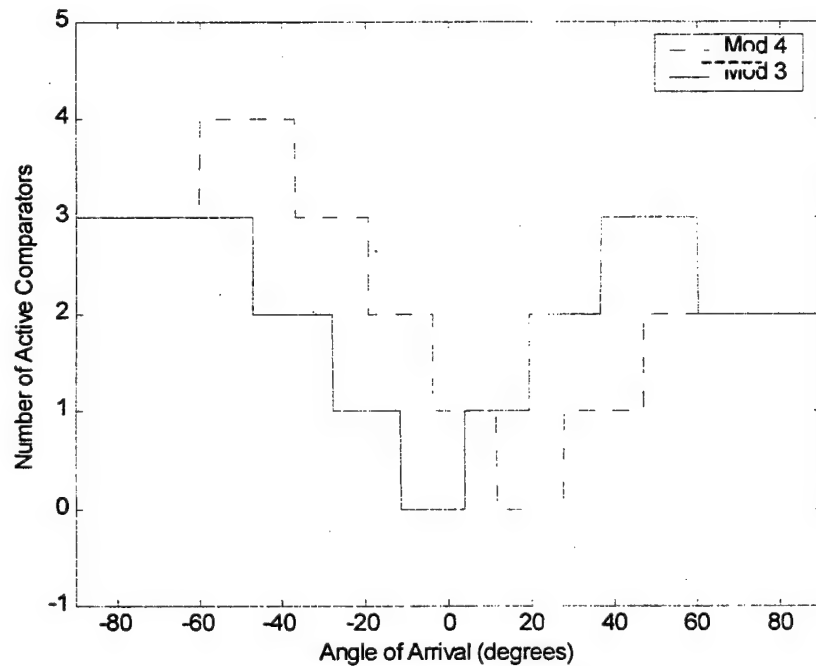


Figure 4 - 5: Active Comparators.

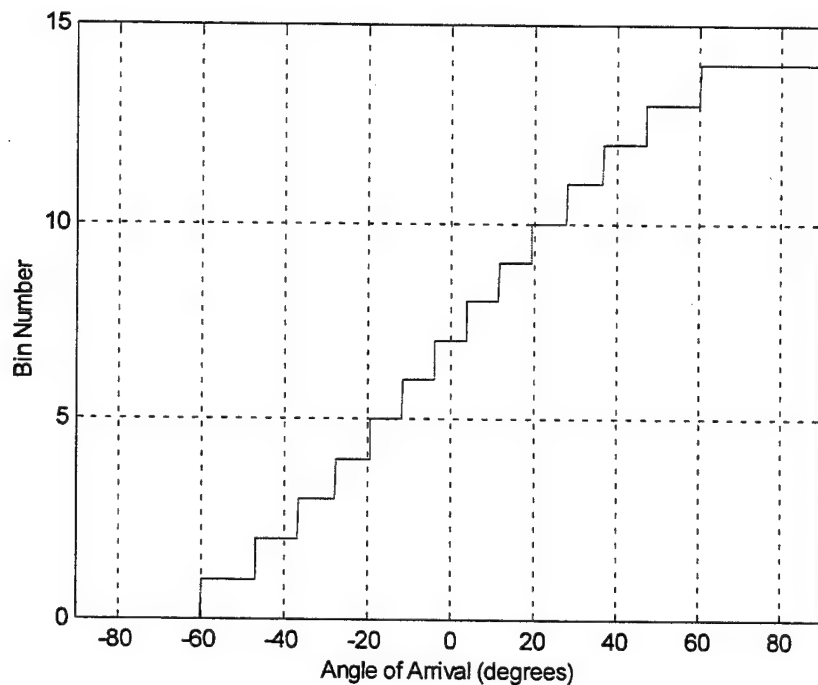


Figure 4 - 6: Bin Number to AOA Mapping.

The folding waveforms of Figure 4 - 4 expand as a function of θ . This causes the bin widths (the angle encompassed within a bin) in Figure 4 - 6 to expand as $|\theta|$ increases (the incident wave diverges from broadside). This effect is caused by the embedded trigonometric functions of Equations 4.14 and 4.15. This effect is obvious when comparing the angle included in Bins 7 and 14. The bin widths are expanding as $1/\sin\theta$, as described in Section F. In Figure 4 - 7, the bin mapping is shown as a function of the sine of the angle of arrival. In this graph, the bin widths are uniform across the $\sin\theta$ domain.

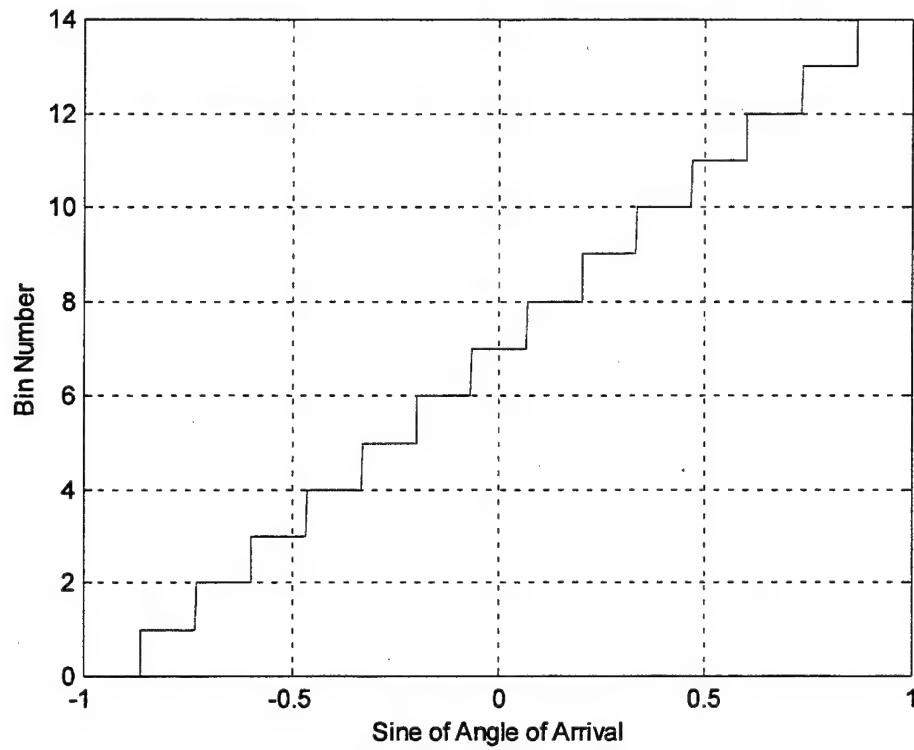


Figure 4 - 7: Bin Number as a Function of Sine of Angle of Arrival.

The bin width in Figure 4 - 7 ($\sin \theta$ space) is:

$$BW = \frac{1}{\hat{M}} \left[\sin\left(\frac{\pi}{2}\right) - \sin\left(\frac{-\pi}{2}\right) \right] = \frac{2}{\hat{M}}. \quad (4.16)$$

Therefore, each bin width is $2/15$. The center of Bin \hat{k} in Figure 4-7 is located at:

$$\sin \theta_{\hat{k}} = \frac{2\hat{k}+1}{\hat{M}} - 1. \quad (4.17)$$

For the first bin (Bin 0), the center is located as $\sin \theta_0 = -1 + BW/2$, and the center of the last bin (Bin 14) is located at $\sin \theta_{14} = 1 - BW/2$. A consequence of quantizing the angle of arrival into a bin is that the RSNS system reports any signal that falls within a bin as if it arrived at the bin center, $\hat{\theta}_k$. That is to say, for one angle within each bin, the estimation is exact, but for the remaining angles a reporting error exists. Figure 4 - 9 illustrates the cause of this sampling quantization error. The quantization error will be analyzed in the next chapter. The bin width in θ -space is

$$r_k = \arcsin\left(\frac{2\hat{k} - \hat{M} + 2}{\hat{M}}\right) - \arcsin\left(\frac{2\hat{k} - \hat{M}}{\hat{M}}\right). \quad (4.18)$$

The best resolution is at broadside ($\theta = 0$) and becomes worse in the end-fire ($|\theta| \rightarrow \pi/2$) regions. Taking the arcsine of each side of Equation 4.17 gives the quantized angle of arrival $\hat{\theta}$ as:

$$\hat{\theta}_k = \sin^{-1}\left(\frac{2\hat{k} + 1}{\hat{M}} - 1\right). \quad (4.19)$$

This is the RSNS transfer function.

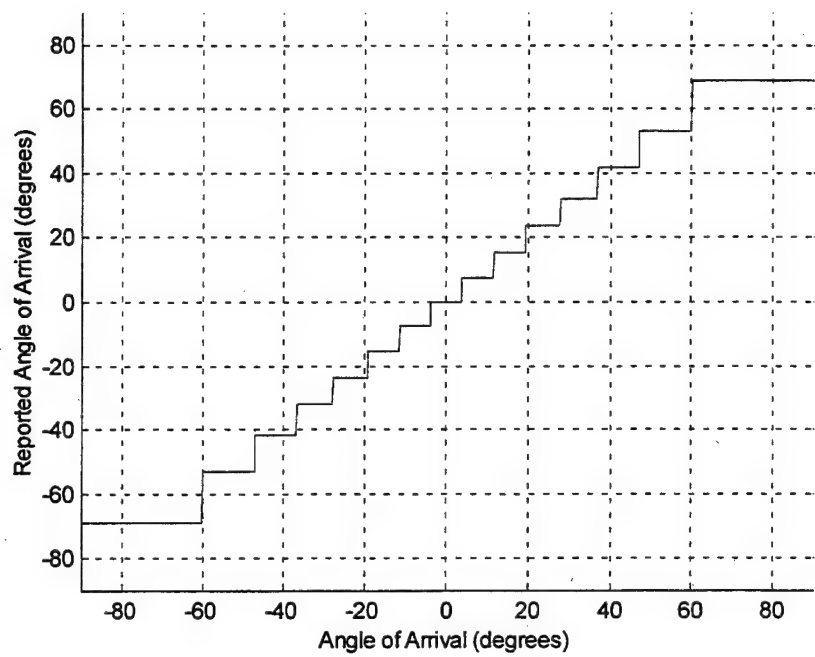


Figure 4 - 8: Reported Angle of Arrival.

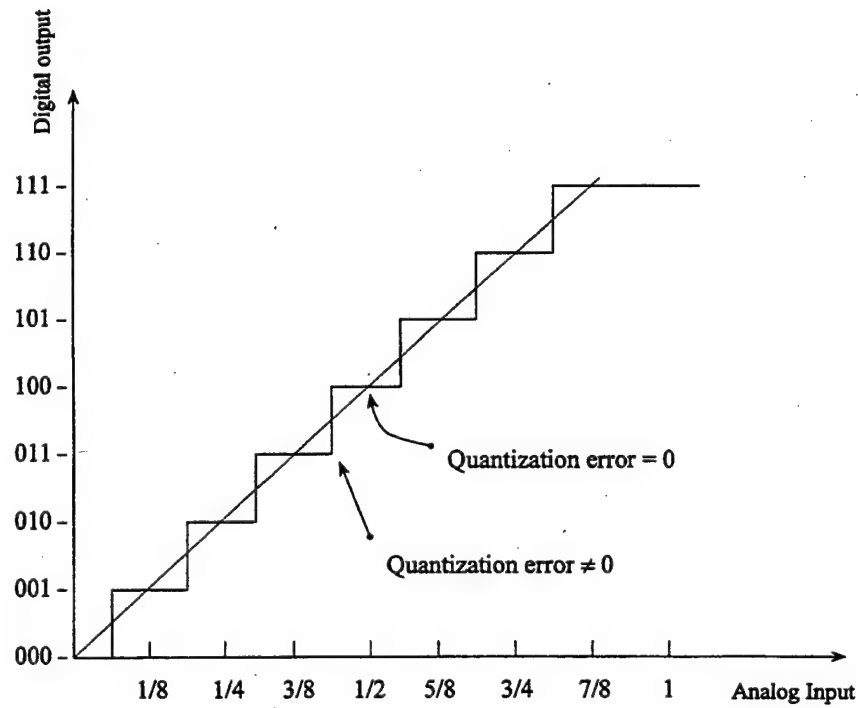


Figure 4 - 9: Quantization Error for Three Bit Resolution.

F. SCALE FACTOR AND MAPPABLE FIELD OF VIEW

The number of folds n_i is the number of folds the a given modulus with a specified dynamic range is capable of mapping. As the element spacing d_i is increased, the number of folding waveforms increases. Increasing d compresses the existing waveform and symmetrically adds additional folds at the extreme angles. This compresses the aperture that the RSNS maps. The maximum mappable aperture, θ_{mm} , that the RSNS dynamic range is capable of mapping is determined by a scale factor, ξ .

The number of folds is a linear function of d (Equation 4.11). For $d=\lambda/2$, the mixer output has one fold. The ratio of the element spacings where d is the unscaled separation and d' is the scaled element separation is the scale factor.

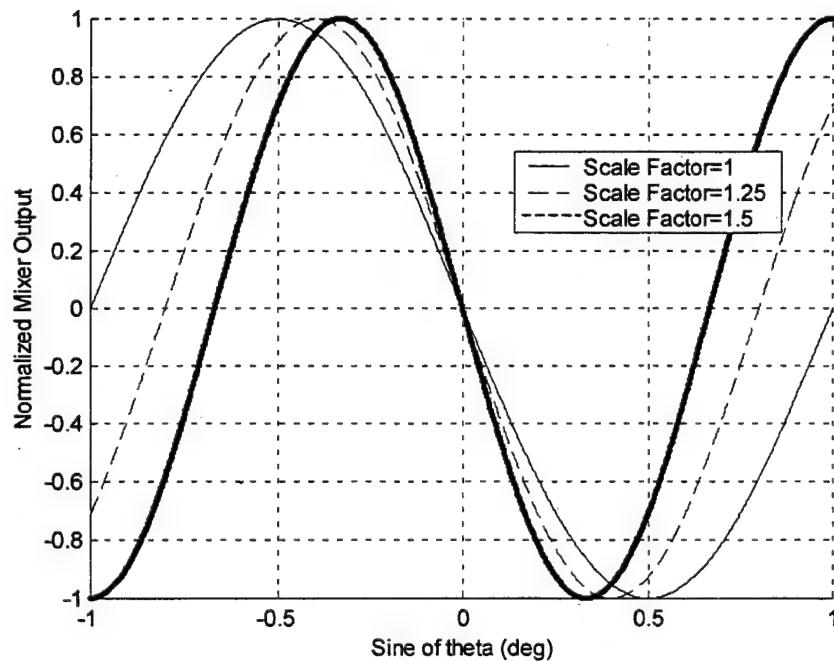
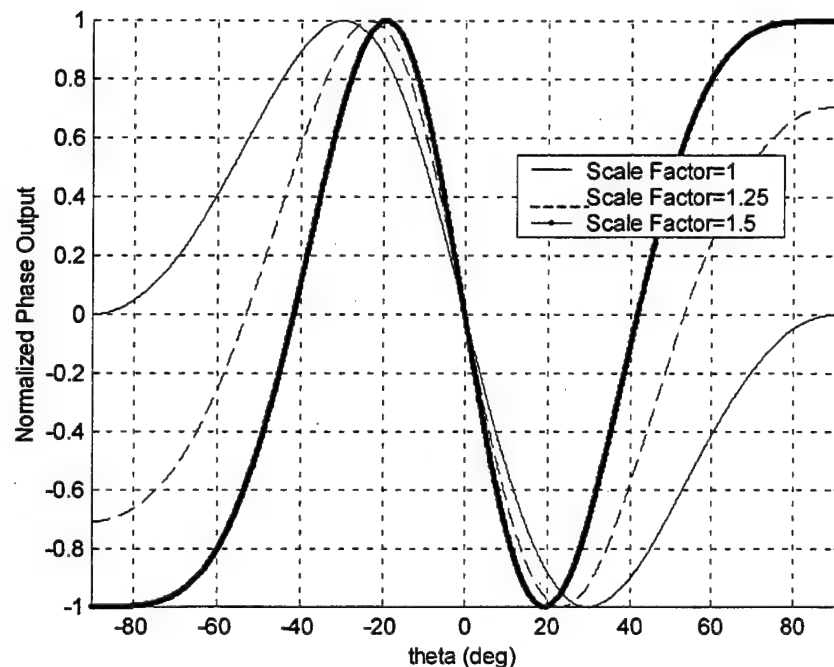
$$\xi = \frac{d}{d'} = \frac{\sin \theta}{\sin \theta'}. \quad (4.20)$$

The mixer output function of θ is shown in Figure 4-10 for three scale factors. The mixer output as a function of $\sin \theta$ is shown in Figure 4 - 11 for the same three scale factors. Including the scale factor in the element spacing, it follows that

$$d_i = \frac{\hat{M}\lambda}{4Nm_i\xi}. \quad (4.21)$$

The new angle resulting from the transformation is:

$$\theta' = \arcsin\left(\frac{\sin \theta}{\xi}\right). \quad (4.22)$$



For example, for $\theta = \pi/2$ and $-\pi/2$, the new angles θ' are shown in Figure 4-12. These particular angles represent θ_{mm} the maximum mappable aperture of the scaled waveform. If the separation of all elements is scaled by the same scale factor, all of the resulting folding waveforms are compressed similarly. The RSNS mapping is maintained; however, the mapping is contained within θ_{mm} . The scaled antenna determines the angle of arrival according to:

$$\hat{\theta} = \arcsin\left(\frac{2\hat{k}+1}{\hat{M}\xi} - \xi\right) \quad (4.23)$$

Beyond θ_{mm} , the folding waveforms continue to be processed by the RSNS circuitry, but the resulting vectors either do not map into the dynamic range or are ambiguous as shown in Figure 4-13. For comparison, the same transfer function operating on an unscaled antenna produces the transfer function shown in Figure 4 - 14.

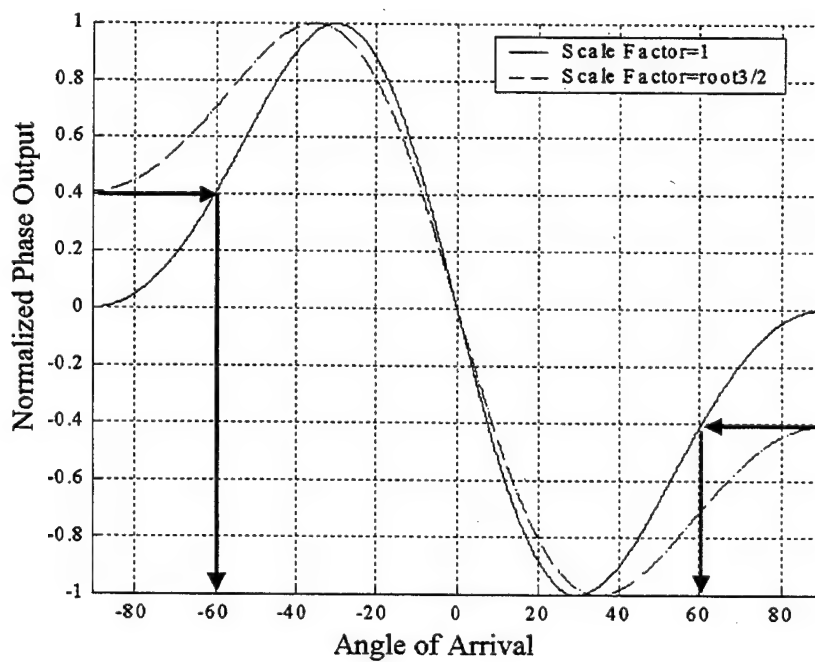


Figure 4 - 12: Determination of Maximum Mappable Aperture.

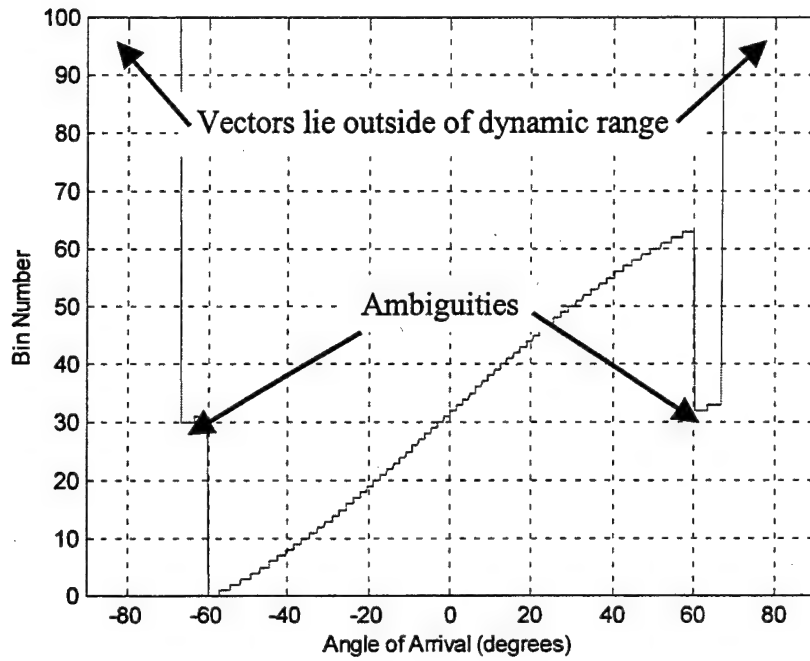


Figure 4 - 13: Transfer Function with Scale Factor $\sqrt{3}/2$.

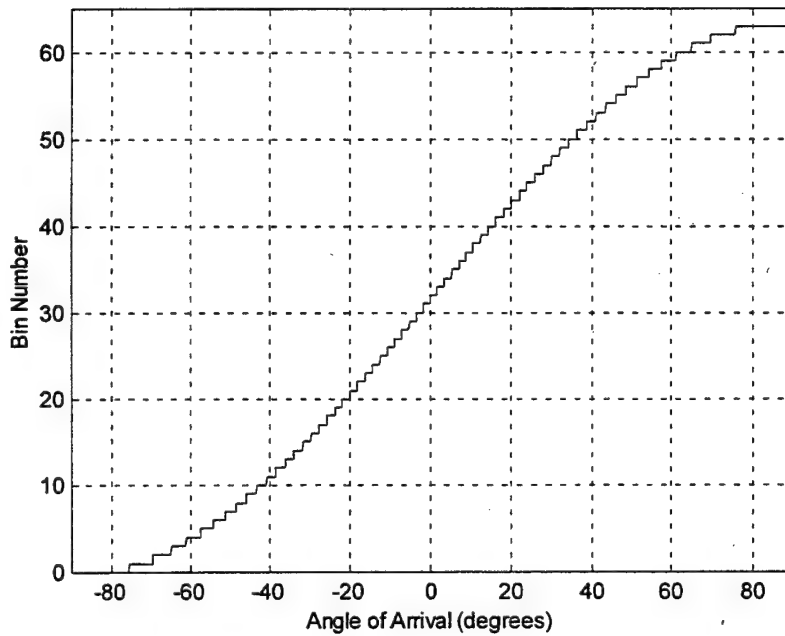


Figure 4 - 14: Unscaled Antenna Transfer Function.

There are several factors affected by changing the spacing of the elements. The increased spacing reduces the antenna's useful field of view, but the larger spaces can decrease mutual coupling. The new field of view reduces the mappable aperture, but it also improves the antenna resolution. The folding waveforms at the endfire do not behave properly and are discarded in the scaled antenna.

The process described in this chapter demonstrates the method of determining the transfer function for a given RSNS antenna configuration. In the next chapter these methods are used to design a high resolution antenna.

V. PROTOTYPE DESIGN AND PREDICTED RESULTS

A. DETERMINATION OF MODULUS AND DYNAMIC RANGE

The previous chapter presented the design equations for an RSNS architecture. This chapter will apply those equations to the design of a prototype antenna array. Two arrays are presented. The arrays are identical except that one is an unscaled array ($\xi = 1$) and the other is scaled with $\xi = \sqrt{3}/2$. MATLAB simulations are used to predict the performance of the prototype antenna. The prototype antenna is shown in Figure 5-1.

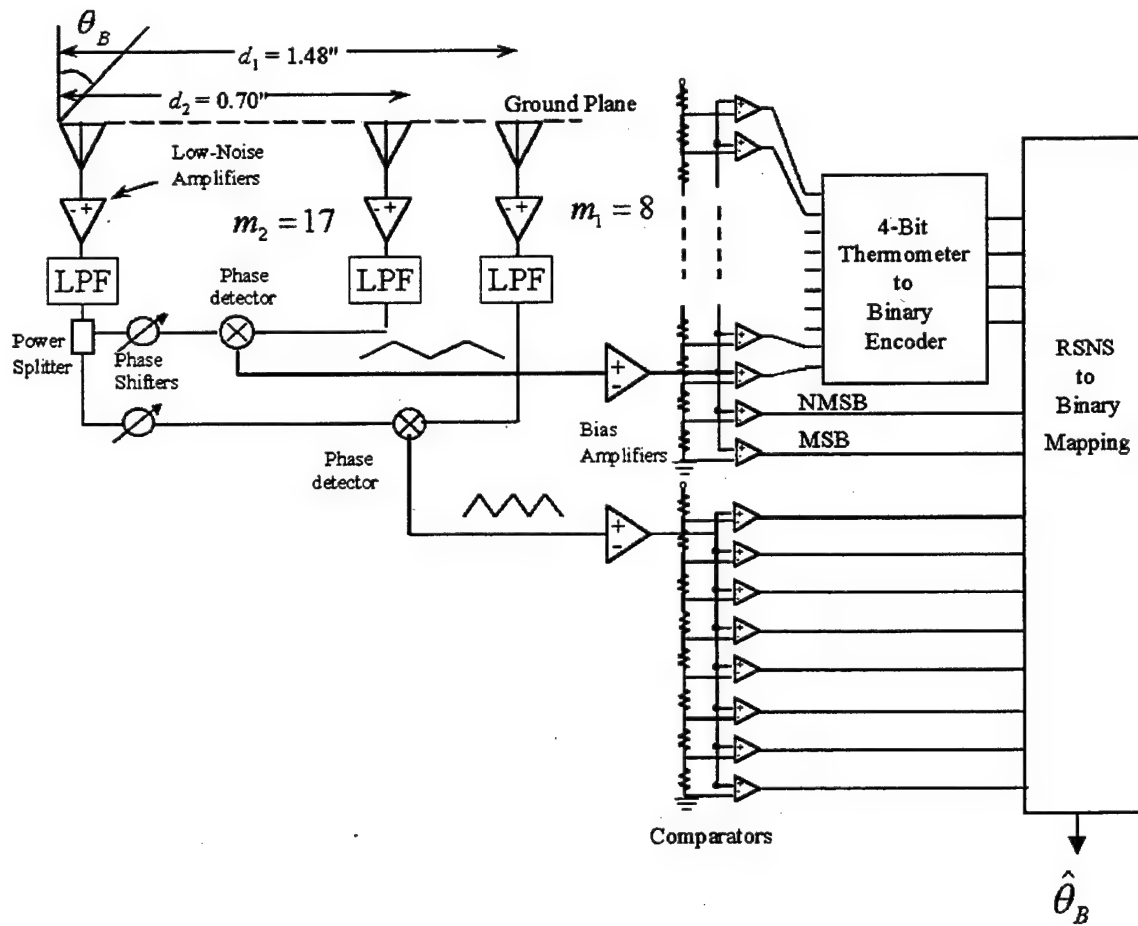


Figure 5 - 1: Block Diagram of the Unscaled RSNS Antenna.

Every design must begin with one decision. The OSNS system previously designed and tested at the Naval Postgraduate School (described in Chapter III) possessed two channels and a dynamic range of 66. In order to design a prototype of comparable spatial resolution, a two-channel system with dynamic range of 64 was chosen. The smaller dynamic range allows the digital hardware to have a 6-bit output, making the RSNS system less complex than the OSNS (7-bit) prototype. The second goal of the prototype was to demonstrate the ambiguity resolution capability of the Robust Symmetrical Number System.

The dynamic range for a two-channel case is $\hat{M} = 4m_1 + 2m_2 - 2$ [14] for moduli spaced three or more integers apart (Equation 4.8). Moduli pairs which have a dynamic range of 64 are $\{(1,31), (2,29), (3,27), (4,25), (5,23), (6,21), (7,19), (8,17), (9,15), \text{ and } (10,13)\}$. The moduli pair (8,17) was chosen to build the prototype. The modulus 8 channel has two folds and the modulus 17 channel has $\frac{16}{17}$ of a fold. This combination of folds will nicely demonstrate the RSNS ambiguity resolution capability. Table 5- 1 shows the vector sequence for $m_1=8$ and $m_2=17$. The dynamic range falls between Vectors 21 and 84. Note that Vector 20 is ambiguous with Vector 52, and Vector 85 is ambiguous with Vector 53. The vectors in the dynamic range are re-indexed with a bin number in the 4th, 8th, and 12th columns.

Vector	Mod 8	Mod 17	Bin	Vector	Mod 8	Mod 17	Bin	Vector	Mod 8	Mod 17	Bin
1	0	0		34	1	16	13	67	1	1	46
2	1	0		35	1	17	14	68	2	1	47
3	1	1		36	2	17	15	69	2	0	48
4	2	1		37	2	16	16	70	3	0	49
5	2	2		38	3	16	17	71	3	1	50
6	3	2		39	3	15	18	72	4	1	51
7	3	3		40	4	15	19	73	4	2	52
8	4	3		41	4	14	20	74	5	2	53
9	4	4		42	5	14	21	75	5	3	54
10	5	4		43	5	13	22	76	6	3	55
11	5	5		44	6	13	23	77	6	4	56
12	6	5		45	6	12	24	78	7	4	57
13	6	6		46	7	12	25	79	7	5	58
14	7	6		47	7	11	26	80	8	5	59
15	7	7		48	8	11	27	81	8	6	60
16	8	7		49	8	10	28	82	7	6	61
17	8	8		50	7	10	29	83	7	7	62
18	7	8		51	7	9	30	84	6	7	63
19	7	9		52	6	9	31	85	6	8	
20	6	9		53	6	8	32	86	5	8	
21	6	10	0	54	5	8	33	87	5	9	
22	5	10	1	55	5	7	34	88	4	9	
23	5	11	2	56	4	7	35	89	4	10	
24	4	11	3	57	4	6	36	90	3	10	
25	4	12	4	58	3	6	37	91	3	11	
26	3	12	5	59	3	5	38	92	2	11	
27	3	13	6	60	2	5	39	93	2	12	
28	2	13	7	61	2	4	40	94	1	12	
29	2	14	8	62	1	4	41	95	1	13	
30	1	14	9	63	1	3	42	96	0	13	
31	1	15	10	64	0	3	43	96	0	14	
32	0	15	11	65	0	2	44	97	1	14	
33	0	16	12	66	1	2	45	98	1	15	

Table 5- 1: Moduli 8 and 17 Vector Sequence.

The selection of moduli determines the required comparator thresholds. As determined by Equation 4.12, the comparator thresholds for the two channels are shown in Table 5- 2.

Comparator	Modulus 8 Channel	Modulus 17 Channel
1	$\cos\left(\frac{15}{16}\pi\right)$	$\cos\left(\frac{33}{34}\pi\right)$
2	$\cos\left(\frac{13}{16}\pi\right)$	$\cos\left(\frac{31}{34}\pi\right)$
3	$\cos\left(\frac{11}{16}\pi\right)$	$\cos\left(\frac{29}{34}\pi\right)$
4	$\cos\left(\frac{9}{16}\pi\right)$	$\cos\left(\frac{27}{34}\pi\right)$
5	$\cos\left(\frac{7}{16}\pi\right)$	$\cos\left(\frac{25}{34}\pi\right)$
6	$\cos\left(\frac{5}{16}\pi\right)$	$\cos\left(\frac{23}{34}\pi\right)$
7	$\cos\left(\frac{3}{16}\pi\right)$	$\cos\left(\frac{21}{34}\pi\right)$
8	$\cos\left(\frac{1}{16}\pi\right)$	$\cos\left(\frac{19}{34}\pi\right)$
9	-----	$\cos\left(\frac{1}{2}\pi\right)$
10	-----	$\cos\left(\frac{15}{34}\pi\right)$
11	-----	$\cos\left(\frac{13}{34}\pi\right)$
12	-----	$\cos\left(\frac{11}{34}\pi\right)$
13	-----	$\cos\left(\frac{9}{34}\pi\right)$
14	-----	$\cos\left(\frac{7}{34}\pi\right)$
15	-----	$\cos\left(\frac{5}{34}\pi\right)$
16	-----	$\cos\left(\frac{3}{34}\pi\right)$
17	-----	$\cos\left(\frac{1}{34}\pi\right)$

Table 5- 2: Modulus 8 and 17 Comparator Thresholds.

B. FOLDING WAVEFORMS

The folding waveforms require two pieces of information: the broadside phase difference and the scale factor. Broadside incidence corresponds to the transition between Bins 31 and 32. Figure 5 - 2 shows these bins. In the modulus 8 channel, broadside is midway between the comparator #7 and comparator #6 thresholds. Since $V_{8,7} = \cos(\frac{5\pi}{16})$ and $V_{8,6} = \cos(\frac{3\pi}{16})$, the forced phase difference ϕ for the modulus 8 channel is $\phi_8 = \frac{4\pi}{16} = \frac{\pi}{4}$. The forced phase difference for the modulus 17 channel is simpler since broadside occurs at the threshold for the ninth comparator. From Equation 4.12, $V_{17,9} = \cos(\frac{17\pi}{34}) = \cos(\frac{\pi}{2})$, therefore, $\phi_{17} = \frac{\pi}{2}$.

Bin	29	30	31	32	33	34
m = 8	7	7	6	6	5	5
m=17	10	9	9	8	8	7

Figure 5 - 2: Vectors around Broadside.

The equations of the folding waveforms with the correct broadside phase difference are (from 4.13):

$$mx_8(\theta) = \cos(kd_8 \sin \theta + \frac{\pi}{4}), \quad (5.1)$$

$$mx_{17}(\theta) = \cos(kd_{17} \sin \theta + \frac{\pi}{2}). \quad (5.2)$$

The folding waveforms for the prototype antenna (Equations 5.1 and 5.2) are simulated for the unscaled array by MATLAB codes *rsns8.m* and *rsns17.m* presented in Appendix A. The simulated phase detector outputs are shown as Figure 5 - 3. The *BinPop.m* algorithm simulates the comparator thermometer code. Its output is shown in Figure 5 - 4. The folding waveforms and thermometer codes for the scaled array are

simulated by the same routines and are presented in Figure 5 - 5 and Figure 5 - 6. The folding waveforms are frequency independent.

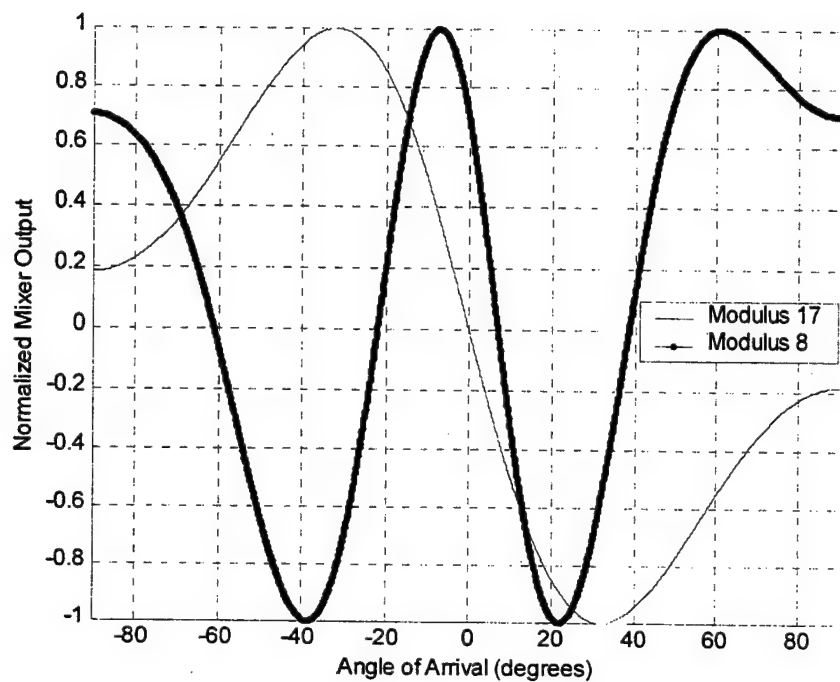


Figure 5 - 3: Folding Waveforms for Unscaled Prototype Array.

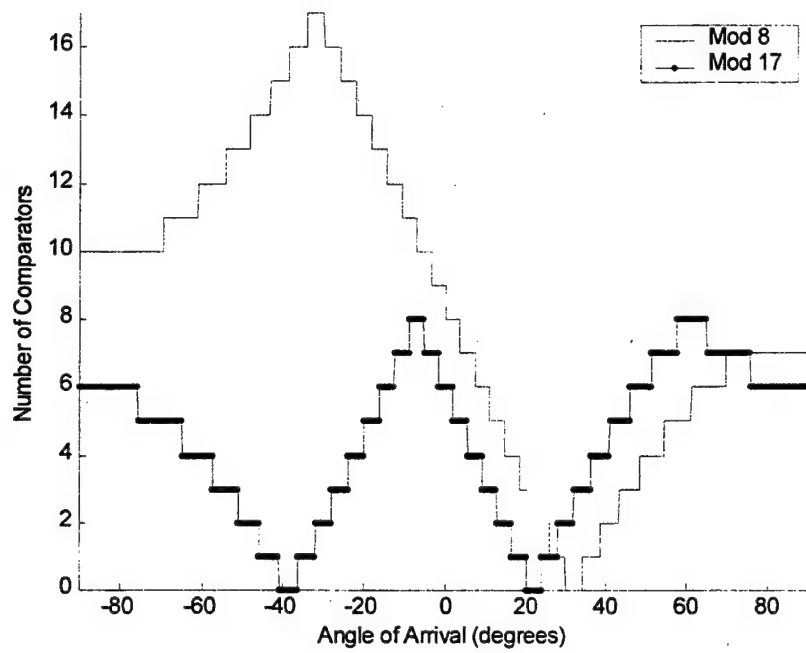


Figure 5 - 4: Comparator States for Unscaled Prototype Array.

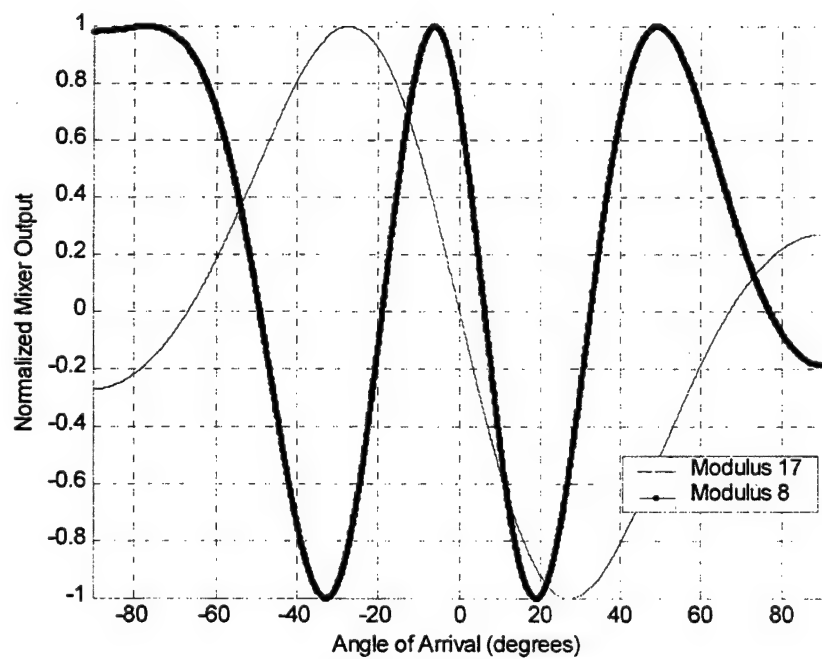


Figure 5 - 5: Folding Waveforms for the Scaled Prototype Array.

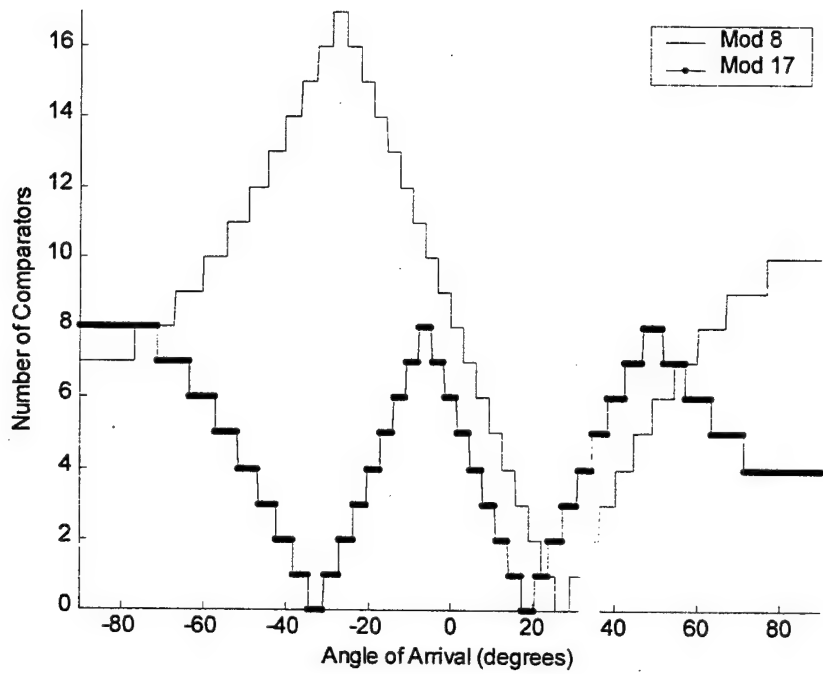


Figure 5 - 6: Comparator States for the Scaled Prototype Array.

C. ELEMENT SPACING

The number of channels, dynamic range, modulus, scale factor, and wavelength determine element spacing (Equation 4.20). The first four variables are set. Only the wavelength remains variable. The OSNS prototype employed coaxial waveguide transitions to receive the incident signal. These components are 1.625 inches in width; therefore, the smallest element separation must be greater than 1.625 inches while maintaining a frequency in the bandwidth of the component (8.2 to 12.4 GHz). The largest modulus determines the minimum element spacing because the modulus is in the denominator of Equation (4.21). The calculated element spacings are too small even at the longest wavelength: $d_{17}(8.2 \text{ GHz}) = 0.68$ inches. To accommodate these components, the scale factor would have to be 2.39 or greater. This scale factor corresponds to a maximum mappable aperture of 25°. This mappable aperture is unacceptably small. Stripline antenna elements were designed and manufactured. These stripline antenna

elements are 50 mils thick. The resonant frequency of the stripline antenna elements is 8.0 GHz. The wavelength is 1.48 inches. The original array did not scale the element spacings; however, mutual coupling concerns prompted the construction of a scaled array. Using equation 4.20 and $\xi = \sqrt{3}/2$, the spacing for each element is presented in Table 5-3.

Unscaled Antenna	Scaled Antenna
$d_8 = \frac{64}{2 \cdot 2 \cdot 8} \cdot \frac{1.48''}{2} \cdot 1 = 1.48''$	$d_8 = \frac{64}{2 \cdot 2 \cdot 8} \cdot \frac{1.48''}{2} \cdot \frac{2}{\sqrt{3}} = 1.70''$
$d_{17} = \frac{64}{2 \cdot 2 \cdot 17} \cdot \frac{1.48''}{2} \cdot 1 = 0.70''$	$d_{17} = \frac{64}{2 \cdot 2 \cdot 17} \cdot \frac{1.48''}{2} \cdot \frac{2}{\sqrt{3}} = 0.80''$

Table 5-3: Element Spacing for the Prototype Antenna Arrays.

D. TRANSFER FUNCTION

The MATLAB algorithm *BinPop.m* that simulated the thermometer code also simulates the transfer function of the entire system. The simulation divides the entire 180° field of view into 0.1° units. This resolution is the minimum step size of the antenna positioning servomotor, so simulated and measured data will be convenient to compare. In each unit, the normalized mixer output is calculated for both channels, and the number of active comparators is determined by comparing the mixer output to the comparator thresholds. The number of active comparators either maps into a bin within the dynamic range (0-63) or is assigned an ‘unmappable’ value of 100. The bin mapping is shown in Figure 5 - 7 and Figure 5 - 8. On the scaled antenna, angles of arrival greater than 60°, the RSNS system does not map accurately, as expected.

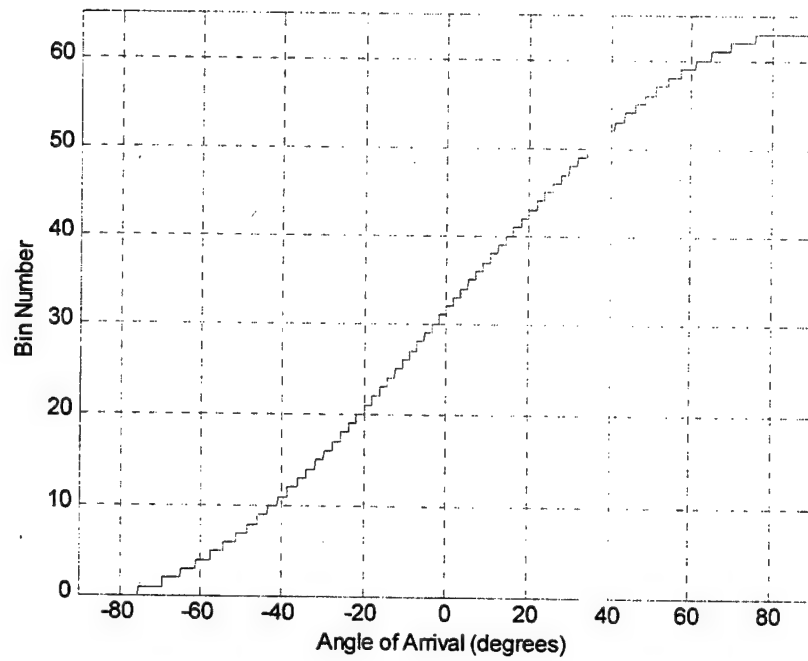


Figure 5 - 7: Unscaled Antenna Map of Angle of Arrival to Bin Number.

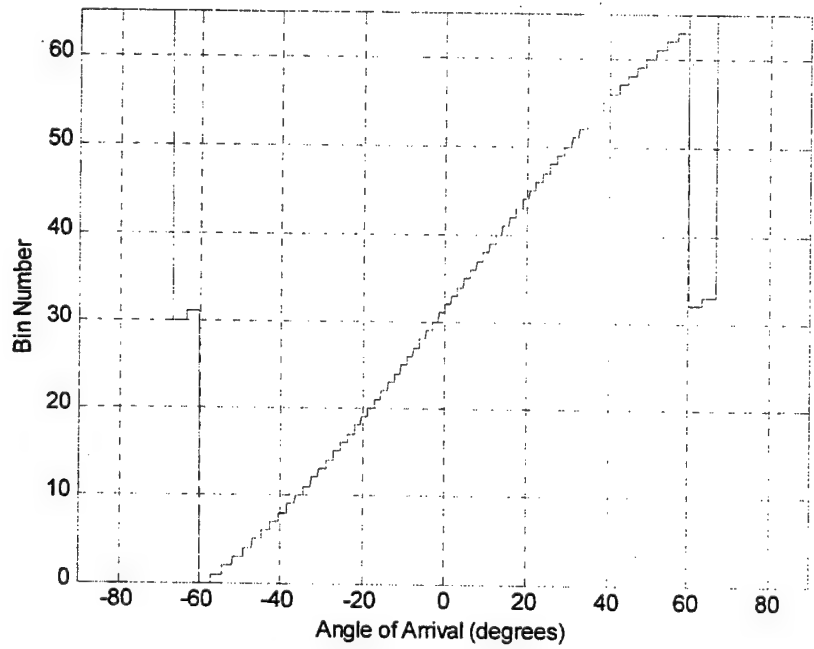


Figure 5 - 8: Scaled Antenna Map of Angle of Arrival to Bin Number.

The bin number corresponds to an angle of arrival, so the same MATLAB algorithm assigns the angle at the bin center $\hat{\theta}_k$ to any unit mapping into that bin. For angles that map into bin 100, the error bin, an angle of arrival of zero is coded as zero. The quantized angle of arrival is the final output of the antenna. Figure 5 - 9 and Figure 5 - 10 show the transfer functions from angle of arrival to reported angle of arrival.

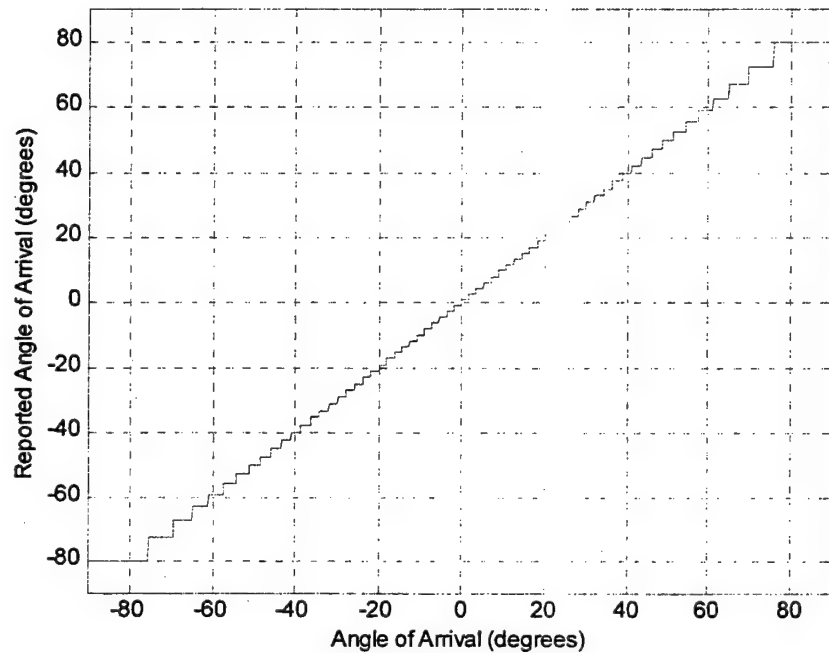


Figure 5 - 9: Unscaled Antenna Transfer Function.

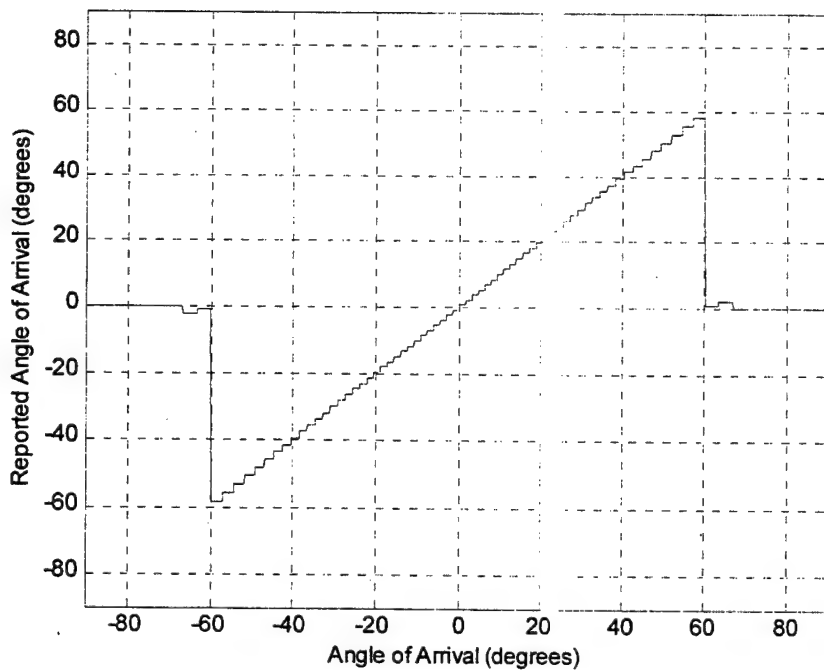


Figure 5 - 10: Scaled Antenna Transfer Function.

1. Bin Population

Each 0.1° is a population point. The “Bin Population” is the quantity of sample points in each bin. *BinPop.m* counts the bin population as the transfer function is applied. Figure 5 - 11 and Figure 5 - 12 shows the bin population for all 64 bins. A small bin population corresponds to a small bin width. This corresponds to a sharp resolution. If the system possessed an infinite number of bins, the bin width would be infinitesimally small, and a smooth curve would result. The bin population curve resembles a cosecant function. The jaggedness of the bin population curves is due to the quantization of the population points. The curve becomes smoother as more points are measured and fractional quantization error becomes smaller. Finally, the bin population curve of the scaled array is only about 85% of the unscaled values. This occurs because the scale factor (approximately 0.866) compresses all of the bin widths by a ratio of the scale factor. This means the bin is a narrower target for the thermometer code.

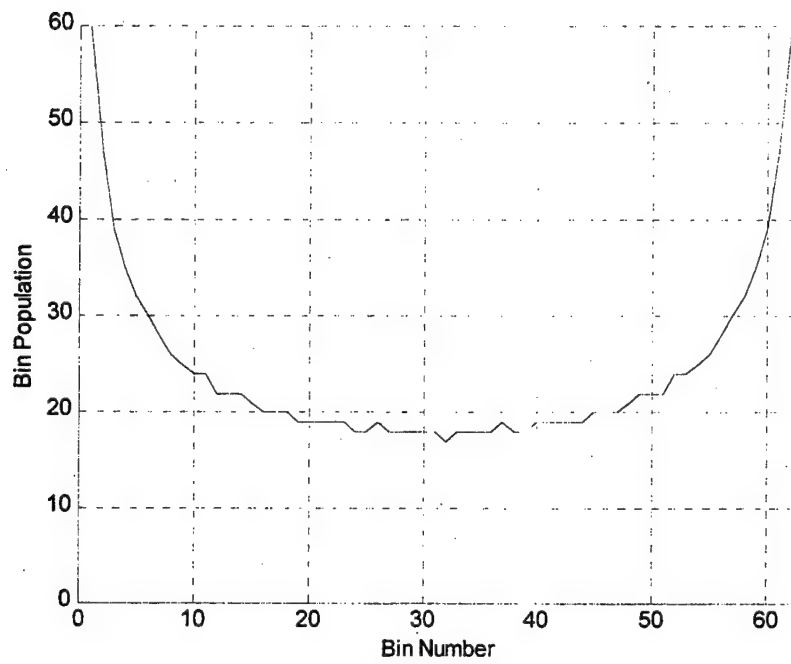


Figure 5 - 11: Bin Population of the Unscaled Antenna.

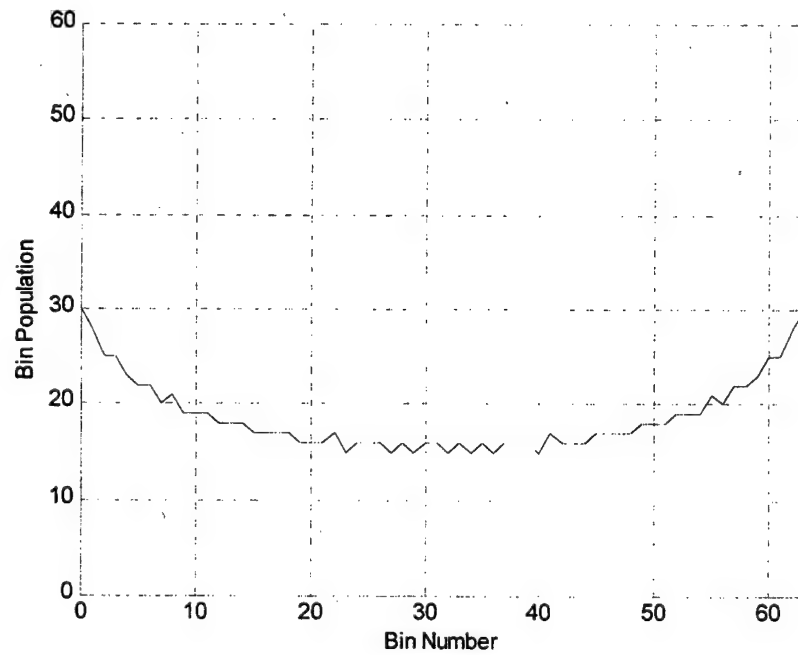


Figure 5 - 12: Bin Population of the Scaled Antenna.

2. Predicted Errors

The true angle of arrival is a continuous function, but all antenna must map the angle of arrival into a finite resolution. This quantization requires that the angle of arrival be estimated. High resolution corresponds to small estimation errors. Figure 5 - 13 and Figure 5 - 14 show the errors that arise due to quantization error. These figures illustrate that the antenna reports the angle of arrival to within one degree throughout most of the mappable field of view. It also shows that the scaled antenna has smaller estimation errors. This confirms the fact that the scaled antenna has a finer resolution and is corollary to the smaller bin population.

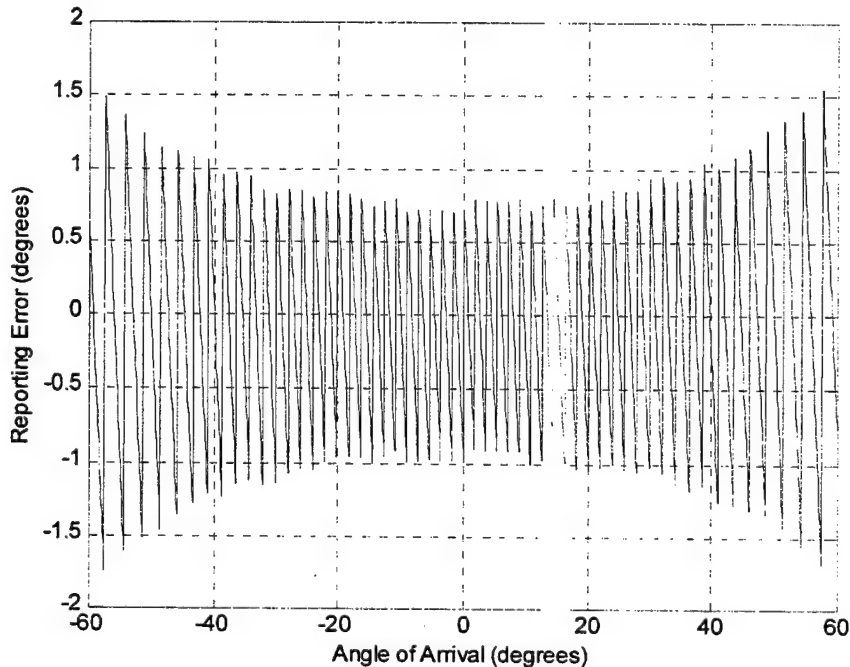


Figure 5 - 13: Quantization Error in Estimated Angle of Arrival for Unscaled Antenna.

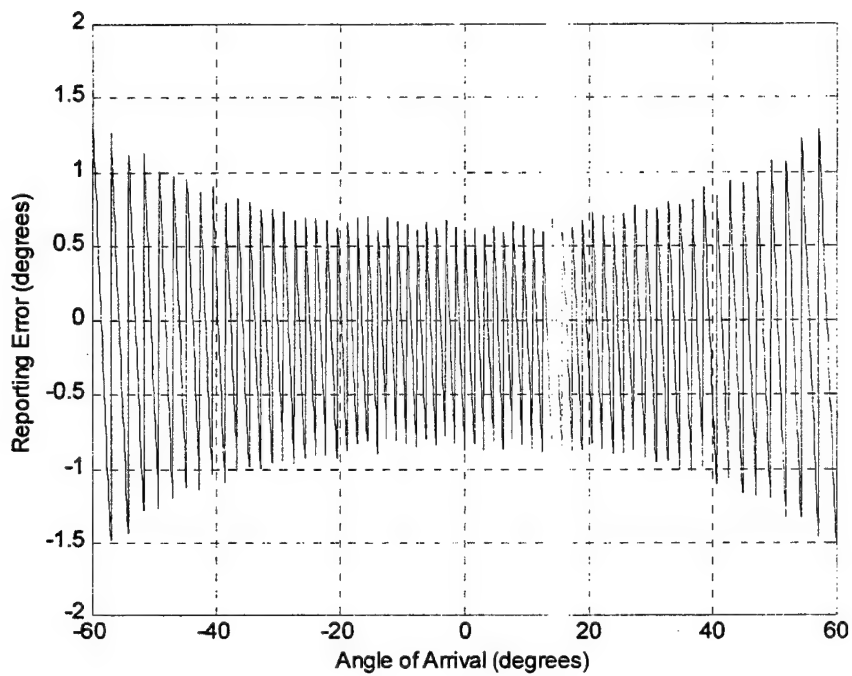


Figure 5 - 14: Quantization Error in Estimated Angle of Arrival for Scaled Antenna

E. MUTUAL COUPLING

The RSNS architecture, like all phase sampling systems, measures the output of a phase detector. Phase detectors are efficient in the absence of mutual coupling but become inefficient when mutual coupling is present. Practical antenna systems have significant levels of mutual coupling. The stripline antenna elements used in the RSNS prototype are closely spaced dipoles, so significant mutual coupling is anticipated. Mutual coupling causes the amplitude of the signal to vary between elements. This amplitude variation is a function of the direction of arrival of the signal. Thus, in the presence of mutual coupling, signal amplitude contains direction information. Discarding the amplitude information will decrease estimation accuracy [4].

The RSNS system operates low noise amplifiers (LNA) in saturation to equalize the amplitude imbalances received by each element. The second effect of mutual

coupling is to introduce phase errors into the signal due to the presence of secondary fields generated by the receiving elements. Although these secondary fields are weak, the elements are in close proximity, so the phase error can be significant. The secondary fields are created because the receiving elements reflect a portion of the incident wave and re-radiate a fraction of the signal due to reflections internal to the microwave circuit. The secondary waves are received at the other elements due to the inefficiency of each element. Dipoles have simple antenna patterns and the strength of the secondary fields can be simulated. The secondary fields also induce reactive fields in the other elements that cause another reaction in the other elements. The field interactions are interlaced. This is mutual coupling. An antenna simulation can predict the phase error generated by mutual coupling. The angle of arrival dependent result is shown as Figure 5 - 15. Element 1 is the reference element, element 2 is the modulus 17 element, and element 3 is the modulus 8 element.

Arrays with many elements have lower mutual coupling for the elements near the center of the array because the induced fields of the outer elements tend to cancel near the array center. Figure 5 - 16 illustrates an array with an additional pair of elements added to the ends of the array. The extra elements do not have circuits attached. Instead, the elements are loaded with a 50Ω dummy load that substitutes for the typical impedance of microwave circuits. The dummy element spacings are equal to the spacing of the adjacent element. The mutual coupling simulation is run for the array with dummy elements, and the results are shown in Figure 5 - 17. The dummy elements reduce the mutual coupling induced phase error by approximately 50%. The scaled antenna will be designed to incorporate such dummy elements.

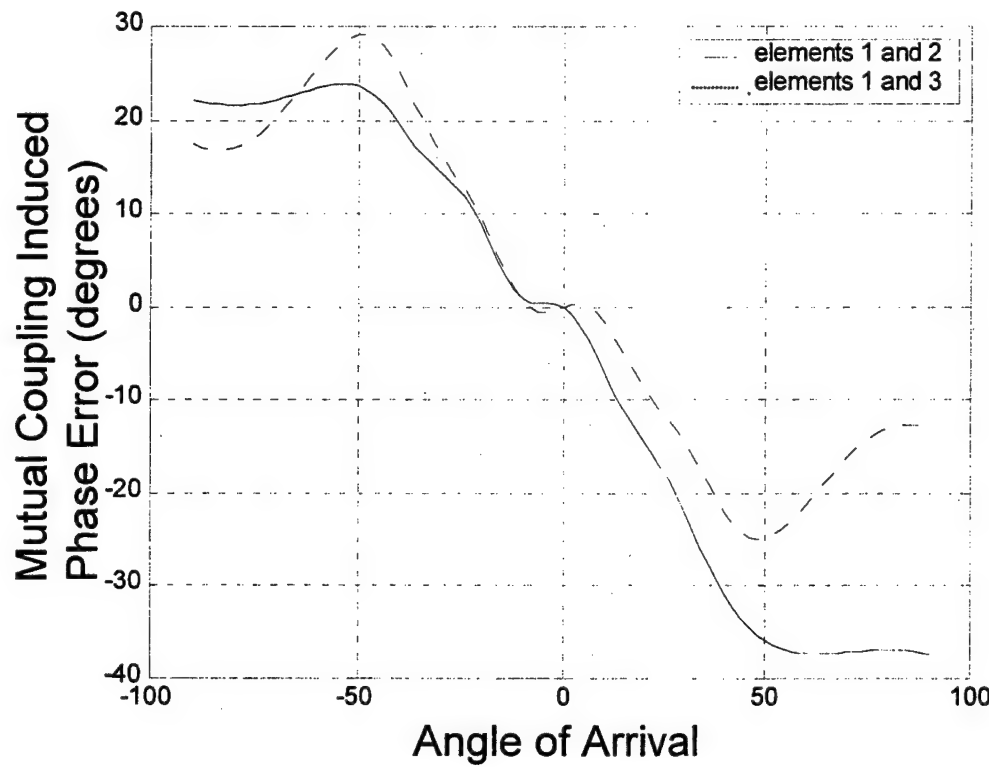


Figure 5 - 15: Predicted Mutual Coupling Phase Error for the Unscaled Antenna.

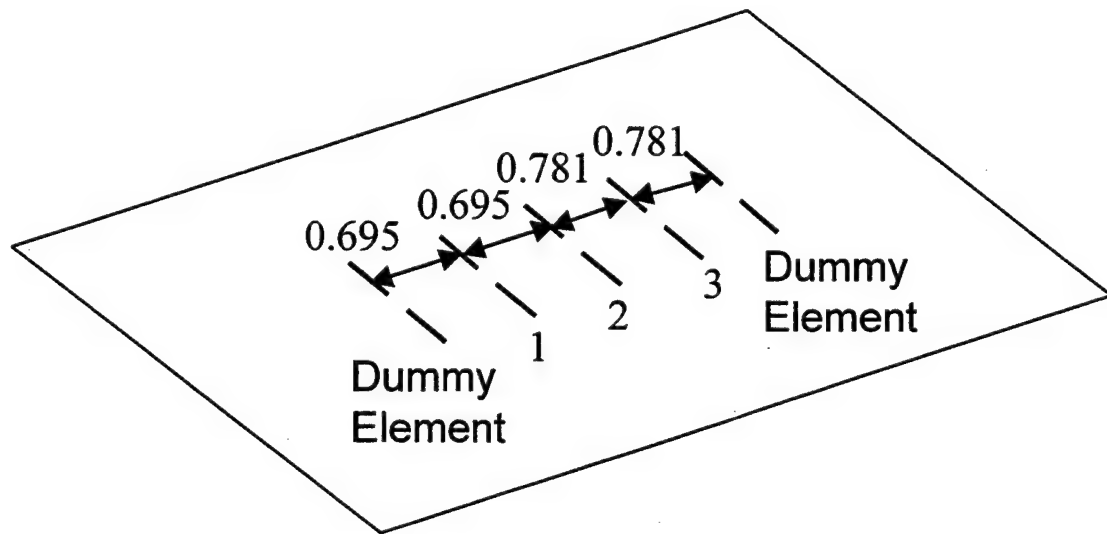


Figure 5 - 16: Unscaled RSNS Array with One Pair of Dummy Elements.

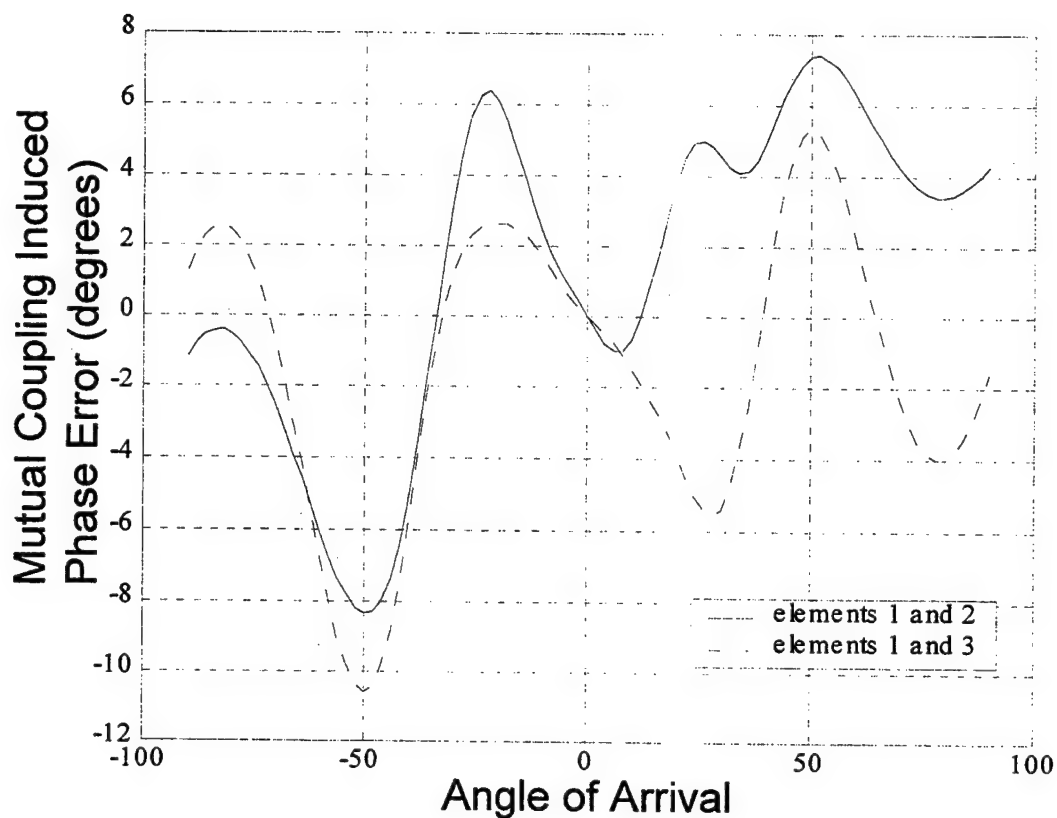


Figure 5 - 17: Simulated Mutual Coupling for Unscaled RSNS Array with Dummy Elements.

These results predicted in this chapter are the baseline for the prototype arrays. In the next chapter the hardware design that implements the RSNS technique will be presented.

VI. RSNS HARDWARE DESIGN

A. ANALOG CIRCUIT COMPONENTS

The microwave circuit shown in Figure 6-1 receives the incident waveform using stripline antenna elements. The entire microwave circuit is mounted on the back of the antenna ground plane. These elements efficiently couple the microwave signal from an atmospheric medium into rigid coaxial cables. The signal is amplified using Low Noise Amplifiers (LNA) to boost the signal and to provide a signal of constant amplitude for all AOA. The low pass filters (LPF) remove all harmonic output from the amplifiers, and the bandpass filters remove the DC component of the mixer output. A power splitter separates the reference signal into two equal signals to be mixed with the *modulus* signals. The modulus signals are phase shifted to set the phase of the signals at broadside relative to the reference. Attenuators are used to match the power from each signal prior to mixing. The mixer multiplies the reference and modulus signals together, and an internal low pass filter outputs only the low frequency term that is proportional to the phase difference between the modulus and reference signals. This signal has a dynamic range of approximately ± 400 mV. It is provided to the digital circuit (located outside of the chamber) via flexible coaxial cables.

1. STRIPLINE ANTENNA ELEMENTS

For the moduli and frequency chosen, standard coaxial transition receiving elements, such as those used in the OSNS prototype, are too wide for the required element spacing. Stripline antenna elements are designed and used to receive the incident waves. These elements are shown in Figure 6-2. Their 60 mil width easily fits within the element spacing. The printed dipoles are designed to resonate at 8.0 GHz. The conceptual linear array is shown in Figure 6-3. Single dipoles have a uniform receiving pattern; however, this pattern is perturbed when the element is located within an array.

The array used to measure the element patterns is shown as Figure 6- 4, and Figure 6- 5 shows the scaled array in the anechoic chamber ready for test. Figure 6- 6 shows the measured and predicted element patterns in the array. The measured patterns closely match the predicted patterns. The power incident upon each element at broadside is approximately -40dBm.

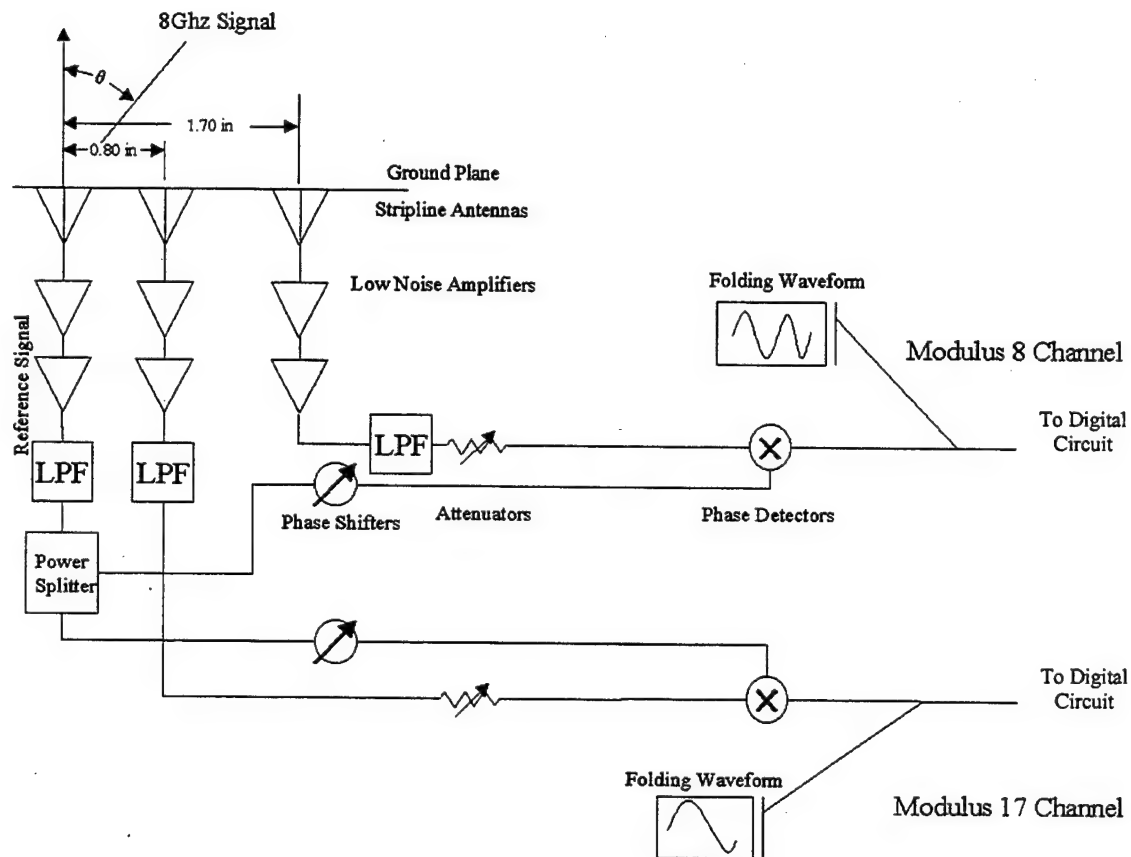


Figure 6- 1: Analog Circuit Diagram Showing Scaled Element Spacings.

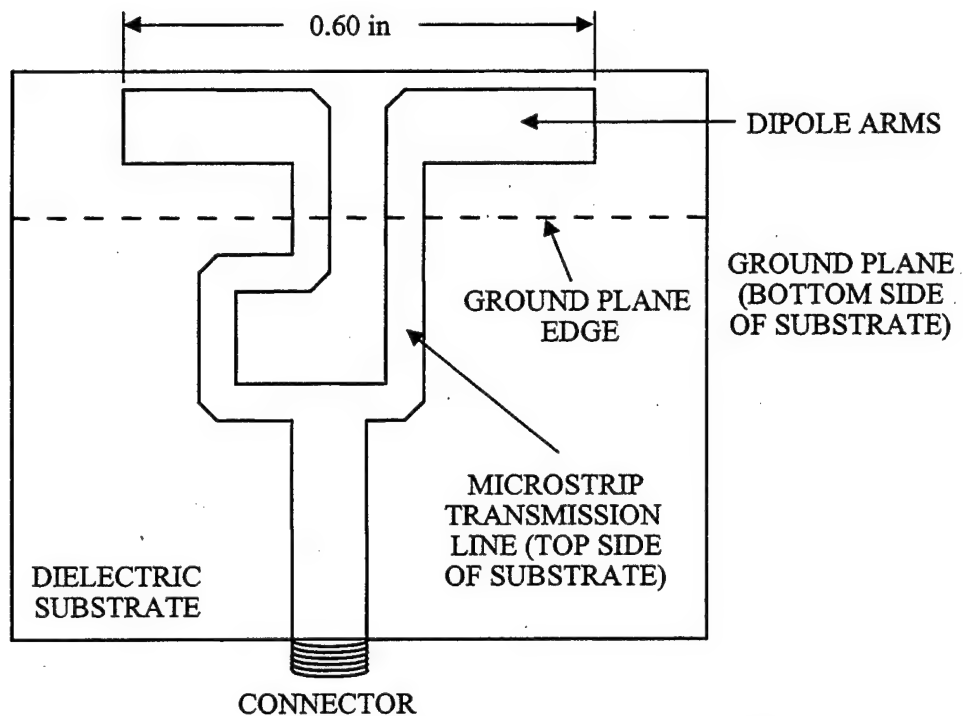


Figure 6- 2: Stripline Element Construction.

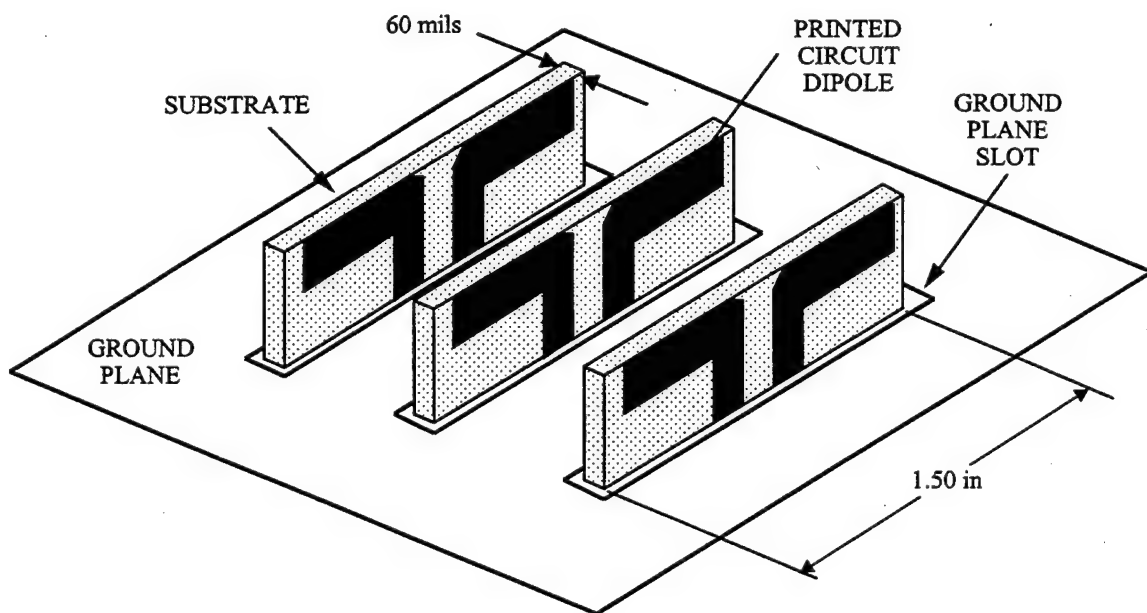


Figure 6- 3: Stripline Element Array Isometric.

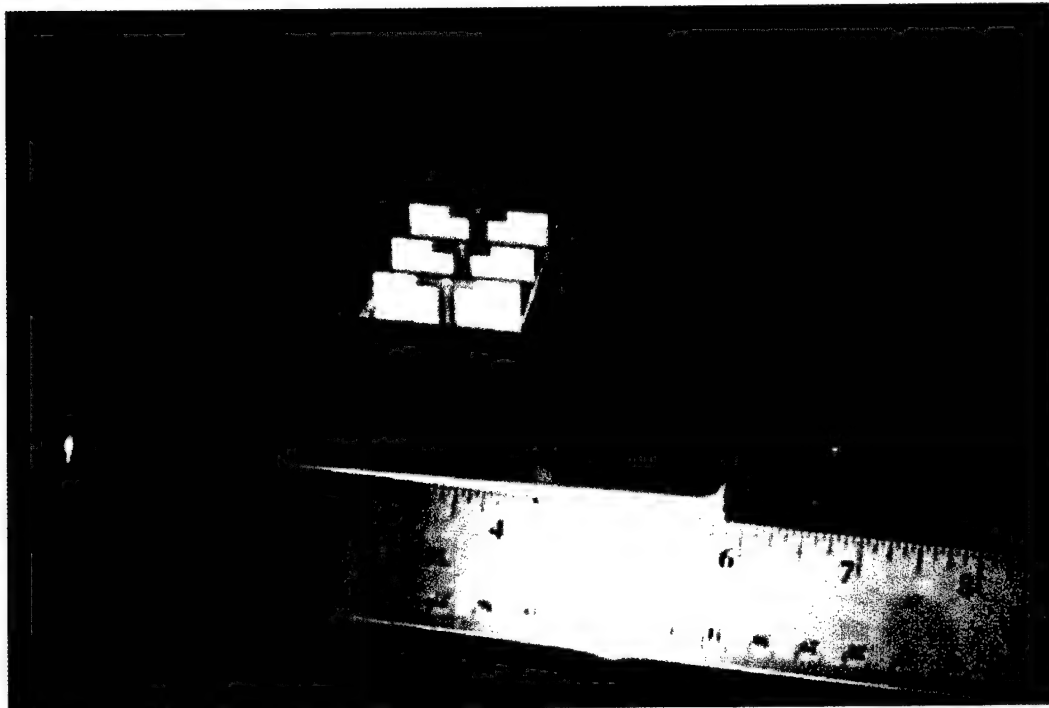


Figure 6- 4: Stripline Antenna Elements Array.

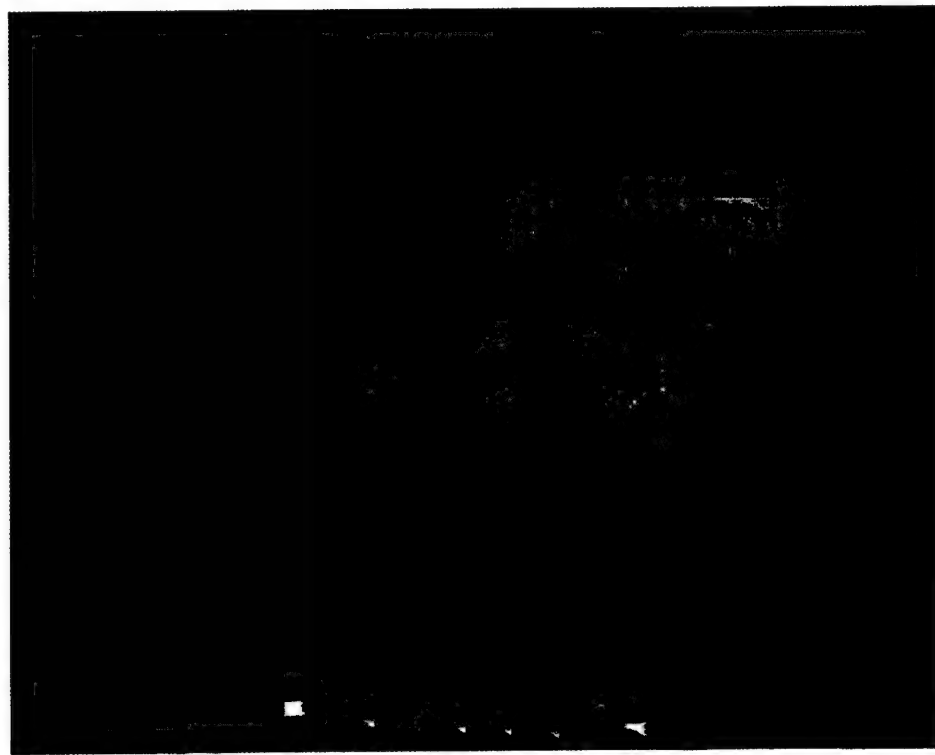


Figure 6- 5: Scaled Array Mounted on Antenna Pedestal.

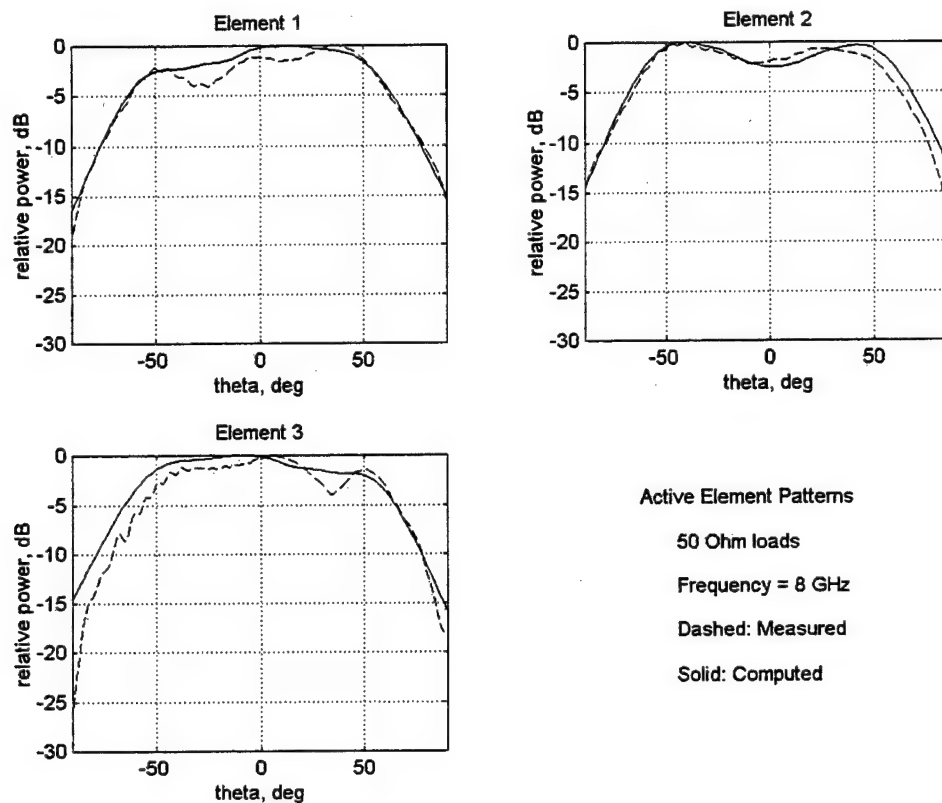


Figure 6- 6: Stripline Antenna Element Patterns.

2. Low Noise Amplifiers

The element patterns in Figure 6- 6 do not have a uniform output over the entire AOA. The phase detector requires equal amplitude inputs to operate properly. The low noise amplifiers (LNA) provide a uniform amplitude input to the phase detector for all AOA. Two LNA are in series after each stripline element. The first amplifier amplifies the signal allowing the second amplifier to operate in saturation. The second amplifier remains in saturation for received powers as low as -59 dBm as shown in Table 6-1. The cascaded amplifier pairs are labeled as shown in Figure 6- 7

Line	Amp	Make	Model	Serial	Saturated Power Out [dBm]	Minimum Input Power to Saturate
Ref	R-1	Avantek	SWL87-1000	F00553-8728	22.82	-59
	R-2	Avantek	SWL87-1000	F01342-8737		
Mod 8	8-1	DBS	DWT 18636	006-9923	20.83	-57
	8-2	DBS	SA84-1043	F03105-8823		
Mod 17	17-1	DBS	DWT 18636	001-9733	21.74	-55
	17-2	Avantek	DWT 18636	005-9922		

Table 6 - 1: Cascaded Amplifier Pairs with Saturation Data.

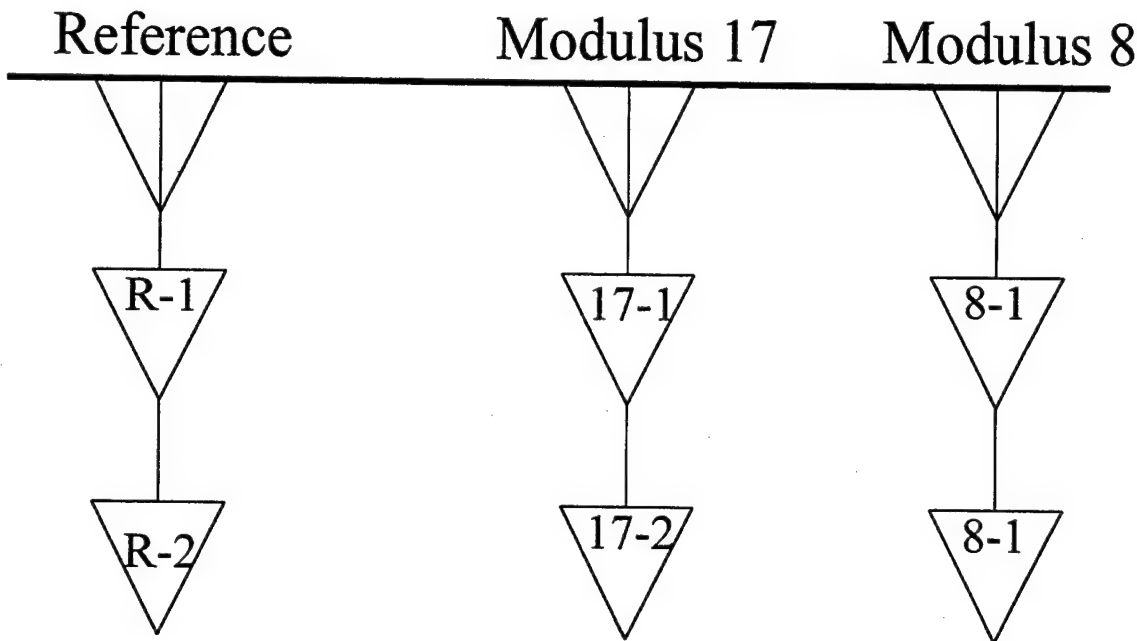


Figure 6- 7: Cascaded Amplifier Pairs.

3. Filters

The amplifiers, operating non-linearly in saturation, produce harmonics as well as the carrier frequency. These harmonic signals have power 20dB lower than the fundamental frequency. The LNAs also have a DC output. These sidebands and DC bias are significant enough to cause mixer phase output errors as large as 20 degrees. Two filters are used to suppress these signals. A low pass filter with cutoff frequency of 9

GHz is used to attenuate the harmonics. The low pass filter is a MICROLAB/FXR Model LA-90N. The stop band attenuation is 55dB minimum. The low pass filter outputs were measured. It attenuated the amplifier harmonic signals to less than 90dB below the fundamental. A band pass filter with pass band between 6 and 9 GHz is used to eliminate the DC bias of the amplifiers. The band pass filter is an AIRTRON part number 456969 and has a pass band of 4-8 GHz. These filters effectively eliminate all signals except for the fundamental and prevent phase errors at the mixer.

4. Phase Shifters

The phase difference between the reference signal and the modulus signal at broadside defines the relationship of the folding waveforms. Phase shifters are used to "phase in" the antenna. The phase shifter is a variable length coaxial cable. At 8.0 GHz, one turn is approximately 8° of phase. Shortening makes the phase more positive, lengthening makes the phase more negative. The total range of the phase shifter is approximately 80° .

5. Attenuators

As shown in Table 6-1, the amplifier pairs have different power outputs. The microwave circuitry with all of the components and connectors attenuate the signals differently in each channel. To provide signals of equal amplitude into the phase detector, the signal amplitudes are measured at the input to the mixer for each channel. Attenuators placed at the mixer input equalize the channel inputs. For the prototype, a 6dB attenuator is placed on the reference line before the modulus 8 mixer and a 2.5dB attenuator is placed on the reference line before the modulus 17 mixer.

6. Phase Detector

The phase detector is the final component in the microwave circuit. The prototype antenna uses two MITEQ model ZMX-10G phase detectors. The phase detector is comprised of two parts. The mixer is used to achieve frequency conversion.

The information contained in the input signal does not change, only the frequency is shifted. Many intermodulation product and harmonic frequencies other than the desired frequency exist at the output of a mixer. The high frequency terms (the term giving the sum of the input frequencies) are filtered through a low pass filter. The only term, which survives out of the low pass filter, is the DC term.

B. DIGITAL CIRCUIT COMPONENTS

The digital circuit (Figure 6- 8) maps the two phase detector outputs to an angle of arrival. The input from each phase detector varies from approximately -400 mV for 180° out of phase to +400 mV for signals that are in phase. The signals are shifted and amplified in the range 1 to 13 volts. Because the phase signal is always positive, only one power supply is required for the reference voltage. The 12 volt difference between the high and low values is a large band for the comparator thresholds and uses the power supply already present for the comparators. The shifted and amplified phase signal is input to all 25 comparators. This signal is compared to the comparator thresholds. Each comparator's TTL output is input to a pin on the Erasable Electronically Programmable Read Only Memory (EEPROM) chips. The two EEPROMs map the active comparators from each channel to a bin. The six-bit output is sent to the computer via the DIO board. The circuit is pictured on top of the computer in the anechoic laboratory in Figure 6- 9 and Figure 6- 10.

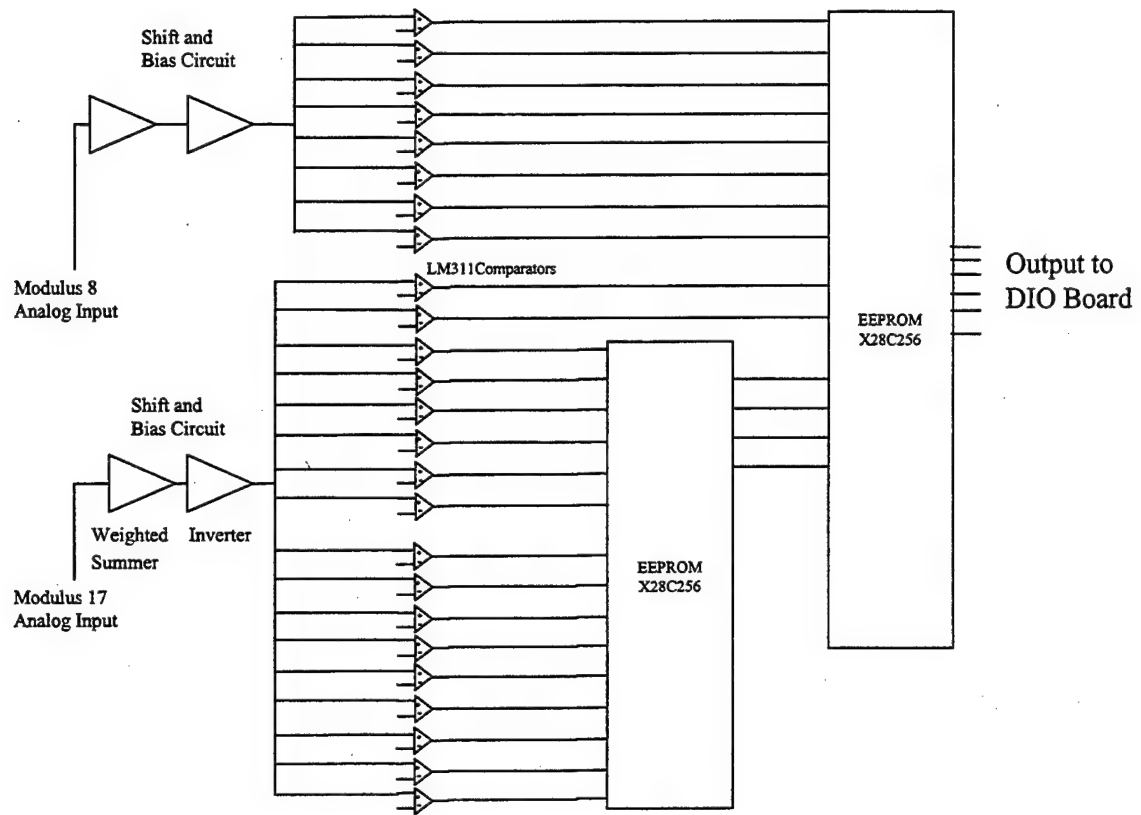


Figure 6- 8: Digital Circuit Diagram.



Figure 6- 9: RSNS Modulus 17 Digital Circuit.

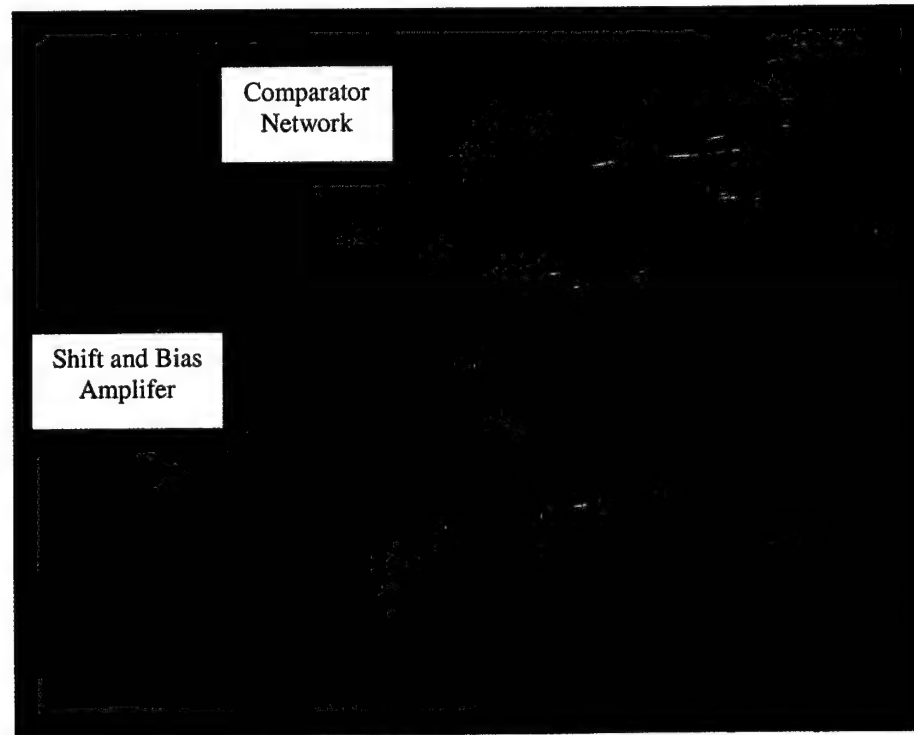


Figure 6- 10: RSNS Modulus 8 Digital Circuit.

1. Shift and Bias Circuit

The phase detector output is bipolar and unsuitable for threshold signal processing. Its small magnitude (approximately 400mV) also requires a tight reference voltage tolerance. The AC component requires the comparators to have multiple power supplies for the reference voltage generation. Both of these are undesirable. The shift and bias circuit converts the 400 millivolt AC signal into a positive voltage in the range of 1-13 volts. This allows the reference voltages to use a significant portion of the existing 18V range. The comparator thresholds are spread apart, and only one power supply is required to generate the reference voltage. The amplification occurs in two steps. First, the phase detector output is amplified using a weighted summing amplifier. Second, the signal is inverted.

The summing amplifier is shown in Figure 6- 11. The amplifier is a National Instruments LM-741CN Operational Amplifier. This amplifier has two inputs: the mixer output (Mod Signal) and V_2 that acts as a bias voltage. R_2 determines the amount of bias V_2 provides. R_1 determines the influence generated by the mixer input. R_3 sets the gain. The equation that governs the amplifier operation is the summing amplifier gain equation [15]:

$$V_{out} = -R_3 \left(\frac{V_1}{R_1} + \frac{V_2}{R_2} \right). \quad (6.1)$$

Because the +18 volt source is available, V_2 is 18 volts. Because one other variable must be chosen, R_3 is set to $10k\Omega$. The two remaining resistance values are determined by matching the phase detector output maximum and minimum values to the desired outputs. The negative sign on the right side of Equation (6.1) indicates that this is an inverting amplifier. The phase detector output has no DC bias. A phase detector output of zero maps to the middle of the shift and bias band: -7 Volts. When $V_1=0$, (6.1) reduces to

$$R_2 = -R_3 \frac{V_2}{V_{out}} = -10k\Omega \cdot \frac{18V}{-7V} = 25.7k\Omega . \quad (6.2)$$

The value of R_1 is determined by the maximum value of the mixer output. For the modulus 17 channel, the maximum mixer output is measured as 365 millivolts and the output is -13 volts. R_1 is determined as follows:

$$R_1 = \frac{-V_1}{\left(\frac{V_{out}}{R_3} + \frac{V_2}{R_2} \right)} = \frac{-0.365V}{\left(\frac{-13V}{10k\Omega} + \frac{18V}{25.7k\Omega} \right)} = \frac{-0.365V}{-600\mu A} = 609\Omega . \quad (6.3)$$

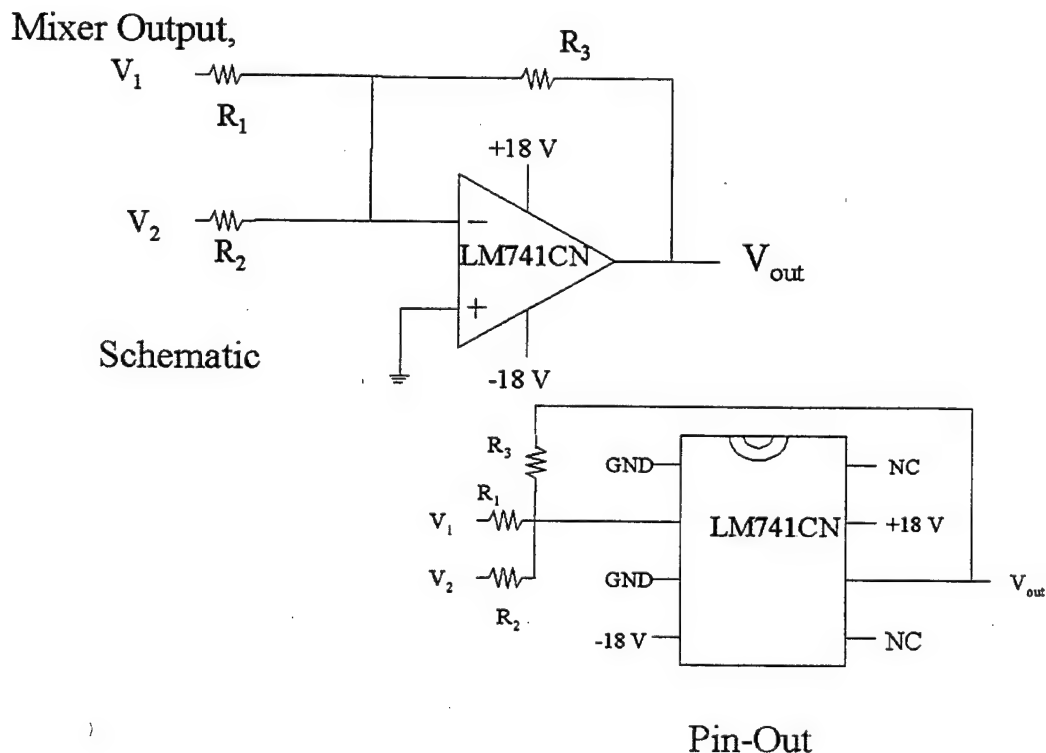


Figure 6- 11: Shift and Bias Weighted Summing Amplifier.

The maximum mixer output of the modulus 8 mixer is 0.397 millivolts. A similar calculation determines $R_1=662\Omega$. R_2 is the same in both channels. R_1 is a $1k\Omega$ variable resistor and R_2 is a variable $10k\Omega$ resistor in series with a $22k\Omega$ resistor.

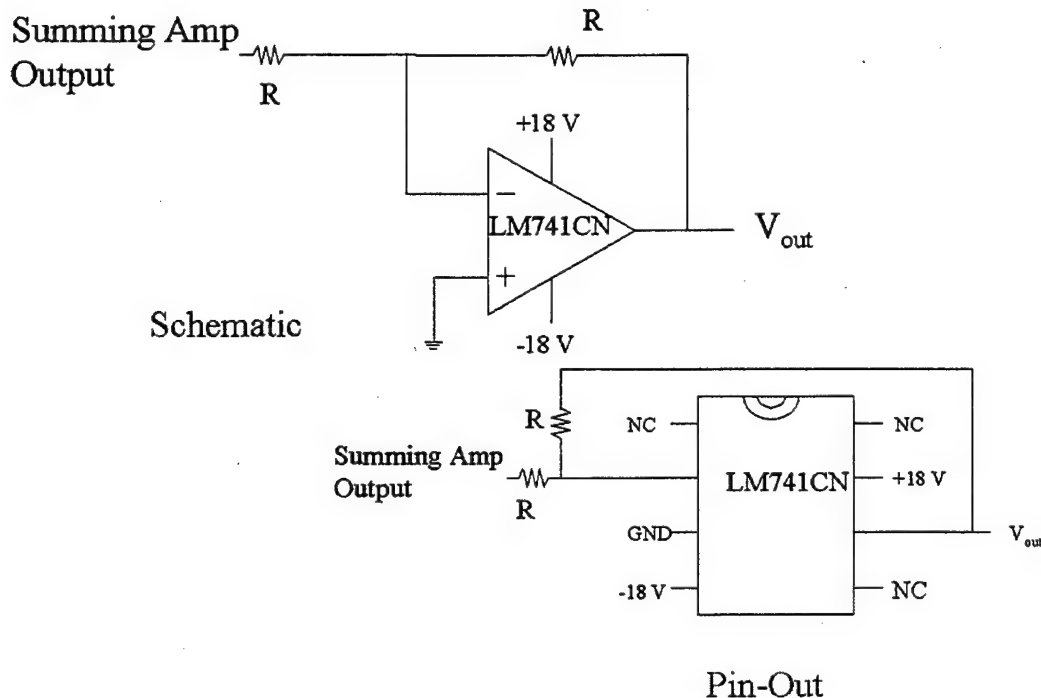


Figure 6- 12: Shift and Bias Inverting Amplifier.

The output of the summing amplifier must be inverted before transmission to the comparators. This is performed by the inverting stage shown in Figure 6- 12. Because the magnitude of the summing amplifier is correct, no amplification is required in the inverting stage. The equation that governs the output of an inverting amplifier is

$$V_{out} = -\frac{R_1}{R_2} V_{in} \quad (6.4)$$

To obtain unity gain with inversion, $R_1=R_2$. 20k Ω resistors are used because precision resistors were available. The output of the inverter is +1 to +13 volts as desired. This signal is provided to the comparators to determine the level of each signal.

2. Comparators

The comparator circuits have 8 and 15 comparators in parallel. The circuit for each comparator is shown in Figure 6- 13.

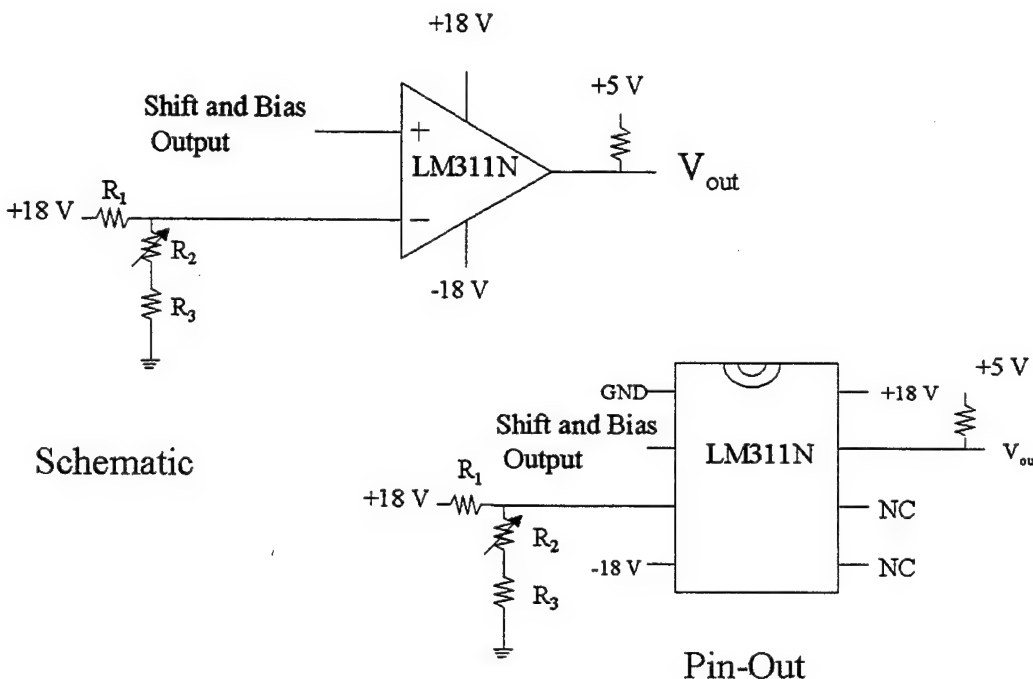


Figure 6- 13: Comparator Schematic and Pin-out Diagram.

The shift and bias circuit output is the input to the non-inverting terminal. The second input is a reference voltage generated in the voltage divider network shown in Figure 6- 14. Since the 18-volt power supply is available as the power supply for the comparator, it is used as the source for the voltage divider. The thresholds for the comparators, as explained in the previous section, range from 1 to 13 volts, so the

conversion from the normalized thresholds to the actual thresholds is $V_{act} = 6V_{norm} + 7$.

The normalized and actual threshold values are shown in columns two and three of

Table 6 - 2. Applying Ohm's law between the source and inverting terminal of the comparator, Equation 6.4 shows the relationship between I_2 and R_2 :

$$I_2 = \frac{18V - V_{threshold}}{R_2}. \quad (6.4)$$

The comparators (National Semiconductor LM311N) have a maximum input bias and offset currents of 100 nA. This current is I_2 in Figure 6- 14. In order to limit the input offset and bias currents to less than 1% of the current in the voltage divider, the total resistance of the network must not exceed $1.5M\Omega$. However, the resistance values must be large enough such that the current required by the system remains small. For these reasons, R_1 is chosen to be $10k\Omega$. The total current for the voltage dividers is

27.5mA as shown in the lower left corner of

Table 6 - 2. Kirchhoff's Current Law applied at the node above R_2 yields $I_3 = I_1 - I_2$. The only variables that remain are R_2 and R_3 . Ohm's law across these resistors dictates:

$$R_2 + R_3 = \frac{V_{thresh}}{I_3}. \quad (6.5)$$

As an initial value, R_2 is chosen to be 5% of R_3 . Once initial values are determined, standard resistor values are chosen and R_2 is made a variable resistor. The voltage divider sub-circuit is complete and provides a precise threshold voltage to the inverting terminal of the comparator.

When the shift and bias signal is larger than the reference voltage, the comparator is ON. In this state, no current is accepted at the output, so the 5 volt signal above the output resistor has no voltage drop. The 5 volts is impressed on the output. This voltage is passed to the input of the EEPROM. If the reference voltage exceeds the shift and bias

signal, the comparator is OFF. In this state, the output sinks current, and the 5 volts are dropped across the output resistor. The output of the comparator is shorted to ground through the opamp and passed to the input of the EEPROM.

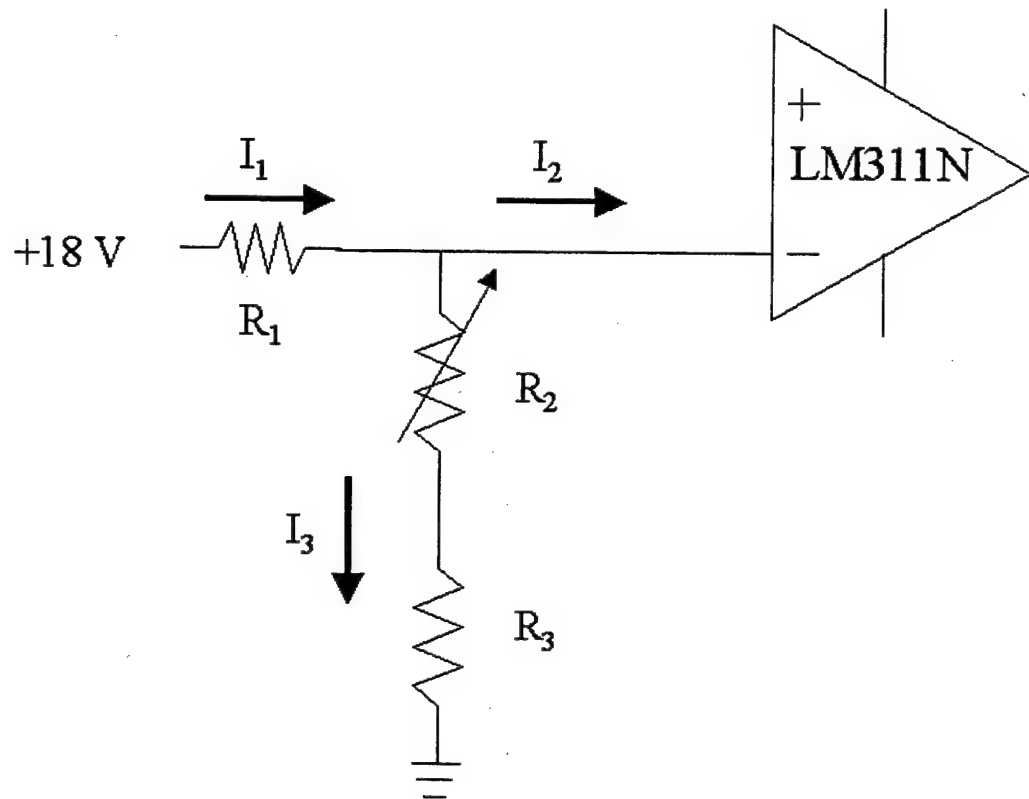


Figure 6- 14: Voltage Divider Circuit.

Simulation Thresholds		Given R1=10k and I2=100 nA					
Mod 8 Channel		Resistance Values					
		R1	R2	Use Var Res	R3	Use Resistor	
t1=	-0.98079	1.11528	811 1.000E+04	812 3.146E+01	1K	813 6.291E+02	5.6K
t2=	-0.83147	2.01116	821 1.000E+04	822 5.990E+01	1K	823 1.198E+03	12K
t3=	-0.55557	3.66655	831 1.000E+04	832 1.218E+02	5K	833 2.436E+03	22K
t4=	-0.19509	5.82943	841 1.000E+04	842 2.281E+02	2K	843 4.562E+03	47K
t5=	0.19509	8.17052	851 1.000E+04	852 3.959E+02	10K	853 7.917E+03	150K/150K
t6=	0.55557	10.33341	861 1.000E+04	862 6.419E+02	20K	863 1.284E+04	120K
t7=	0.83147	11.98881	871 1.000E+04	872 9.499E+02	20K	873 1.900E+04	180K
t8=	0.98079	12.88471	881 1.000E+04	882 1.200E+03	50K	883 2.399E+04	220K
Mod 17 Channel							
t1=	-0.99573	1.02559	711 1.000E+04	712 2.877E+01	1K	713 5.755E+02	5.6K
t2=	-0.96183	1.22905	721 1.000E+04	722 3.490E+01	1K	723 6.980E+02	6.8K
t3=	-0.89516	1.62902	731 1.000E+04	732 4.739E+01	2K	733 9.477E+02	18K/18K
t4=	-0.79802	2.21190	741 1.000E+04	742 6.672E+01	5K	743 1.334E+03	12K
t5=	-0.67370	2.95782	751 1.000E+04	752 9.364E+01	5K	753 1.873E+03	18K
t6=	-0.52643	3.84141	761 1.000E+04	762 1.292E+02	10K	763 2.584E+03	22K
t7=	-0.36124	4.83255	771 1.000E+04	772 1.748E+02	10K	773 3.496E+03	33K
t8=	-0.18375	5.89750	781 1.000E+04	782 2.321E+02	5K	783 4.641E+03	47K
t9=	0.00000	7.00000	791 1.000E+04	792 3.031E+02	10K	793 6.061E+03	56K
t10=	0.18375	8.10250	7A1 1.000E+04	7A2 3.899E+02	10K	7A3 7.797E+03	150K/150K
t11=	0.36124	9.16745	7B1 1.000E+04	7B2 4.943E+02	5K	7B3 9.886E+03	100K
t12=	0.52643	10.15859	7C1 1.000E+04	7C2 6.170E+02	20K	7C3 1.234E+04	120K
t13=	0.67370	11.04217	7D1 1.000E+04	7D2 7.558E+02	20K	7D3 1.512E+04	150K
t14=	0.79802	11.78810	7E1 1.000E+04	7E2 9.038E+02	20K	7E3 1.808E+04	180K
t15=	0.89516	12.37098	7F1 1.000E+04	7F2 1.047E+03	50K	7F3 2.093E+04	180K
t16=	0.96183	12.77095	7G1 1.000E+04	7G2 1.163E+03	50K	7G3 2.326E+04	220K
t17=	0.99573	12.97441	7H1 1.000E+04	7H2 1.230E+03	50K	7H3 2.459E+04	220K
Current Values		Input Bias Current: 1.00E-07					
		I1	I2	I3			
		811 1.688E-03	812 1.00E-07	813 1.688E-03			
		821 1.599E-03	822 1.00E-07	823 1.599E-03			
		831 1.433E-03	832 1.00E-07	833 1.433E-03			
		841 1.217E-03	842 1.00E-07	843 1.217E-03			
		851 9.829E-04	852 1.00E-07	853 9.828E-04			
		861 7.667E-04	862 1.00E-07	863 7.666E-04			
		871 6.011E-04	872 1.00E-07	873 6.010E-04			
		881 5.115E-04	882 1.00E-07	883 5.114E-04			
		711 1.697E-03	712 1.00E-07	713 1.697E-03			
		721 1.677E-03	722 1.00E-07	723 1.677E-03			
		731 1.637E-03	732 1.00E-07	733 1.637E-03			
		741 1.579E-03	742 1.00E-07	743 1.579E-03			
		751 1.504E-03	752 1.00E-07	753 1.504E-03			
		761 1.416E-03	762 1.00E-07	763 1.416E-03			
		771 1.317E-03	772 1.00E-07	773 1.317E-03			
		781 1.210E-03	782 1.00E-07	783 1.210E-03			
		791 1.100E-03	792 1.00E-07	793 1.100E-03			
		7A1 9.898E-04	7A2 1.00E-07	7A3 9.897E-04	A=10		
		7B1 8.833E-04	7B2 1.00E-07	7B3 8.832E-04	B=11		
		7C1 7.841E-04	7C2 1.00E-07	7C3 7.840E-04	C=12		
		7D1 6.958E-04	7D2 1.00E-07	7D3 6.957E-04	D=13		
		7E1 6.212E-04	7E2 1.00E-07	7E3 6.211E-04	E=14		
		7F1 5.629E-04	7F2 1.00E-07	7F3 5.628E-04	F=15		
		7G1 5.229E-04	7G2 1.00E-07	7G3 5.228E-04	G=16		
		7H1 5.026E-04	7H2 1.00E-07	7H3 5.025E-04	H=17		

Table 6 - 2: Voltage Divider Calculations.

3. EEPROM

The 25 comparator states must be processed into a 6-bit angle of arrival. The electronically erasable programmable read only memory (EEPROM) performs this mapping function. ATMEL Model AT28C256 is used. The EEPROM is a small logic block. Each EEPROM converts 15 input bits to an 8-bit output via its internal programming. Because of the limit of 15 inputs, two EEPROM must be used to process all 25 comparators. The "Thermometer Code" programmed into the EEPROM is shown in Table 6 - 3. The thermometer code is the string instructions to the EEPROM that maps input to output. With two EEPROM the thermometer code has two stages as shown on the circuit diagrams of Figure 6- 15 and Figure 6- 16.

The first stage encodes the 15 least significant (lowest threshold) comparators of the modulus 17 channel into a 4-bit representation of the number of active comparators. The encoding is a simple binary conversion. The second column of Table 6 - 3 is the number of comparators active in the modulus 17 channel in each bin. The fourth column is a binary representation of the state of the input pins for the first EEPROM and the fifth column is the hexadecimal representation of that binary number. The sixth column is the decimal output desired from EEPROM #1 for the given input; it is the decimal number of number of active comparators. The seventh column is the hexadecimal representation of that digital number. The result is that the number of active comparators is converted to a 4-bit input. The shift and bias circuit and comparators for Modulus 17 and EEPROM #1 are physically located on the same circuit board. The output of EEPROM #1 and comparators 16 and 17 must be passed to EEPROM #2 on the second circuit board. Figure 6- 15 illustrates how this signal is passed to EEPROM #2.

RSNS Encoding Scheme

Bin	XICOR #1:10 LSB of Mod 17 Channel			XICOR #2:7 MSB of Mod 17 Channel						
	Channel 17	Channel 8	Input XICOR #1	Hex Input XICOR #1	Output XICOR #1	Hex Out XICOR #1	Input XICOR#2	Hex Input XICOR#2	Output XICOR#2	Hex Out XICOR#2
0	10	6	000 0011 1111 1111	03FF	10	A	000 1111 1100 1010	0FCA	0	00
1	10	5	000 0011 1111 1111	03FF	10	A	000 0111 1100 1010	07CA	1	01
2	11	5	000 0111 1111 1111	07FF	11	B	000 0111 1100 1011	07CB	2	02
3	11	4	000 0111 1111 1111	07FF	11	B	000 0111 1100 1011	03CB	3	03
4	12	4	000 1111 1111 1111	0FFF	12	C	000 0011 1100 1100	03CC	4	04
5	12	3	000 1111 1111 1111	0FFF	12	C	000 0001 1100 1100	01CC	5	05
6	13	3	001 1111 1111 1111	1FFF	13	D	000 0001 1100 1101	01CD	6	06
7	13	2	001 1111 1111 1111	1FFF	13	D	000 0000 1100 1101	00CD	7	07
8	14	2	011 1111 1111 1111	3FFF	14	E	000 0000 1100 1110	00CE	8	08
9	14	1	011 1111 1111 1111	3FFF	14	E	000 0000 0100 1110	004E	9	09
10	15	1	111 1111 1111 1111	7FFF	15	F	000 0000 0100 1111	004F	10	0A
11	15	0	111 1111 1111 1111	7FFF	15	F	000 0000 0000 1111	000F	11	0B
12	16	0	111 1111 1111 1111	7FFF	15	F	000 0000 0001 1111	001F	12	0C
13	16	1	111 1111 1111 1111	7FFF	15	F	000 0000 0101 1111	005F	13	0D
14	17	1	111 1111 1111 1111	7FFF	15	F	000 0000 0111 1111	007F	14	0E
15	17	2	111 1111 1111 1111	7FFF	15	F	000 0000 1111 1111	00FF	15	0F
16	16	2	111 1111 1111 1111	7FFF	15	F	000 0000 1101 1111	00DF	16	10
17	16	3	111 1111 1111 1111	7FFF	15	F	000 0001 1101 1111	01DF	17	11
18	15	3	111 1111 1111 1111	7FFF	15	F	000 0001 1100 1111	01CF	18	12
19	15	4	111 1111 1111 1111	7FFF	15	F	000 0011 1100 1111	03CF	19	13
20	14	4	011 1111 1111 1111	3FFF	14	E	000 0011 1100 1110	03CE	20	14
21	14	5	011 1111 1111 1111	3FFF	14	E	000 0111 1100 1110	07CE	21	15
22	13	5	001 1111 1111 1111	1FFF	13	D	000 0111 1100 1101	07CD	22	16
23	13	6	001 1111 1111 1111	1FFF	13	D	000 1111 1100 1101	0FCDD	23	17
24	12	6	000 1111 1111 1111	0FFF	12	C	000 1111 1100 1100	0FCC	24	18
25	12	7	000 1111 1111 1111	0FFF	12	C	001 1111 1100 1100	1FCC	25	19
26	11	7	000 0111 1111 1111	07FF	11	B	001 1111 1100 1011	1FCB	26	1A
27	11	8	000 0111 1111 1111	07FF	11	B	011 1111 1100 1011	3FCB	27	1B
28	10	8	000 0111 1111 1111	03FF	10	A	011 1111 1100 1010	3FCA	28	1C
29	10	7	000 0011 1111 1111	03FF	10	A	001 1111 1100 1010	1FCA	29	1D
30	9	7	000 0001 1111 1111	01FF	9	9	001 1111 1100 1001	1FC9	30	1E
31	9	6	000 0001 1111 1111	01FF	9	9	000 1111 1100 1001	0FC9	31	1F
32	8	6	000 0001 1111 1111	00FF	8	8	000 1111 1100 1000	0FC8	32	20
33	8	5	000 0000 1111 1111	00FF	8	8	000 0111 1100 1000	07C8	33	21
34	7	5	000 0000 0111 1111	007F	7	7	000 0111 1100 0111	07C7	34	22
35	7	4	000 0000 0111 1111	007F	7	7	000 0011 1100 0111	03C7	35	23
36	6	4	000 0000 0011 1111	003F	6	6	000 0011 1100 0110	03C6	36	24
37	6	3	000 0000 0011 1111	003F	6	6	000 0001 1100 0110	01C6	37	25
38	5	3	000 0000 0001 1111	001F	5	5	000 0001 1100 0101	01C5	38	26
39	5	2	000 0000 0001 1111	001F	5	5	000 0000 1100 0101	00C5	39	27
40	4	2	000 0000 0000 1111	000F	4	4	000 0000 1100 0100	00C4	40	28
41	4	1	000 0000 0000 1111	000F	4	4	000 0000 0100 0100	0044	41	29
42	3	1	000 0000 0000 0111	0007	3	3	000 0000 0100 0011	0043	42	2A
43	3	0	000 0000 0000 0111	0007	3	3	000 0000 0000 0011	0003	43	2B
44	2	0	000 0000 0000 0011	0003	2	2	000 0000 0000 0010	0002	44	2C
45	2	1	000 0000 0000 0011	0003	2	2	000 0000 0100 0010	0042	45	2D
46	1	1	000 0000 0000 0001	0001	1	1	000 0000 0100 0001	0041	46	2E
47	1	2	000 0000 0000 0001	0001	1	1	000 0000 1100 0001	00C1	47	2F
48	0	2	000 0000 0000 0000	0000	0	0	000 0000 1100 0000	00C0	48	30
49	0	3	000 0000 0000 0000	0000	0	0	000 0001 1100 0000	01C0	49	31
50	1	3	000 0000 0000 0001	0001	1	1	000 0001 1100 0001	01C1	50	32
51	1	4	000 0000 0000 0001	0001	1	1	000 0011 1100 0001	03C1	51	33
52	2	4	000 0000 0000 0011	0003	2	2	000 0011 1100 0010	03C2	52	34
53	2	5	000 0000 0000 0011	0003	2	2	000 0111 1100 0010	07C2	53	35
54	3	5	000 0000 0000 0111	0007	3	3	000 0111 1100 0011	07C3	54	36
55	3	6	000 0000 0000 0111	0007	3	3	000 1111 1100 0011	0FC3	55	37
56	4	6	000 0000 0000 1111	000F	4	4	000 1111 1100 0100	0FC4	56	38
57	4	7	000 0000 0000 1111	000F	4	4	001 1111 1100 0100	1FC4	57	39
58	5	7	000 0000 0001 1111	001F	5	5	001 1111 1100 0101	1FC5	58	3A
59	5	8	000 0000 0001 1111	001F	5	5	011 1111 1100 0101	3FC5	59	3B
60	6	8	000 0000 0011 1111	003F	6	6	011 1111 1100 0110	3FC6	60	3C
61	6	7	000 0000 0011 1111	003F	6	6	001 1111 1100 0110	1FC6	61	3D
62	7	7	000 0000 0111 1111	007F	7	7	001 1111 1100 0111	1FC7	62	3E
63	7	6	000 0000 0111 1111	007F	7	7	000 1111 1100 0111	0FC7	63	3F

Table 6 - 3: Thermometer Code of EEPROM Programming.

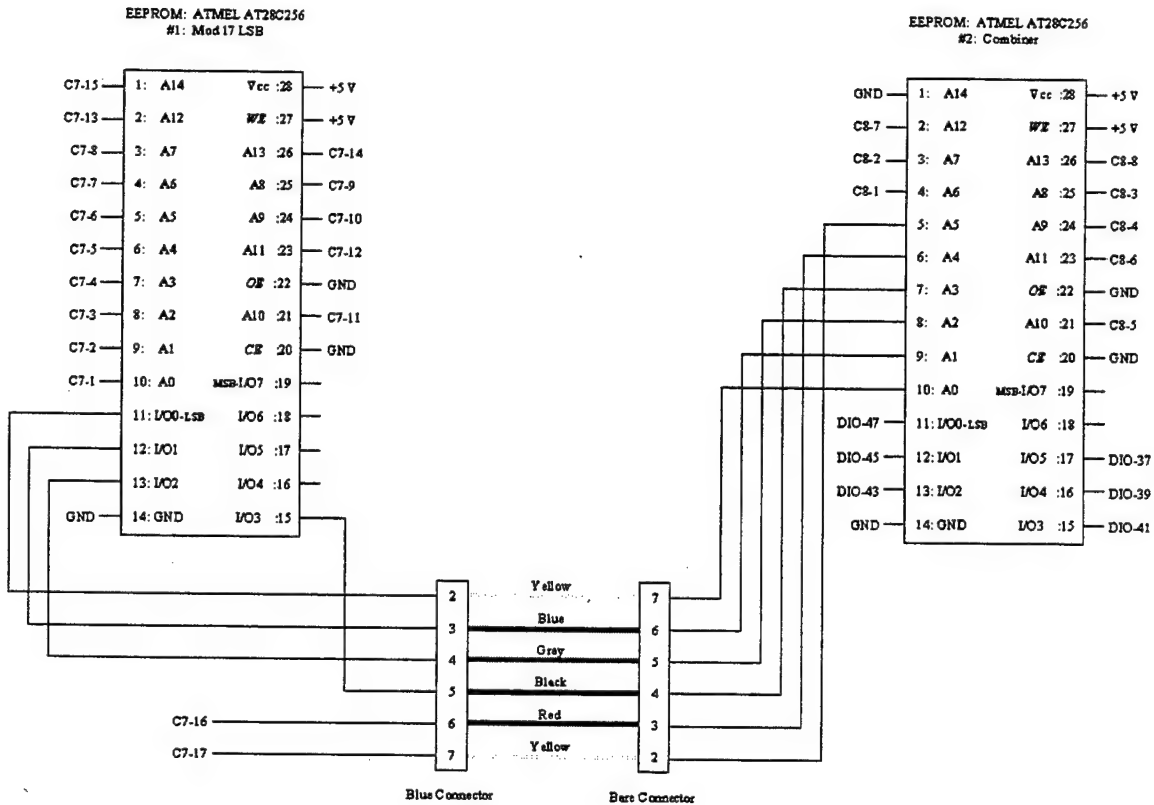


Figure 6- 15: Schematic Diagram of Mod 17 Comparator Output to EEPROM#2 Input.

EEPROM #2 takes the 4-bit output of EEPROM #1 into the least significant bit input. Modulus 17 comparators 16 and 17 are the next two input bits. The next eight input bits are the modulus 8 comparator inputs. Table 6 - 3 column 8 shows the binary input to EEPROM #2 for each bin and column 9 is the hexadecimal representation of this input. Column 10 is the digital output and column 11 is the hexadecimal output. The hexadecimal columns are required because the programming of the EEPROM is conducted in hexadecimal representation. The 6-bit output of EEPROM #2 is the input to the DIO board. The DIO board is the interface with the computer and has 50 pins. Figure 6- 16 diagrams how the signal is passed to the proper pins of the DIO board. LABVIEW samples the input from the DIO board and records the data.

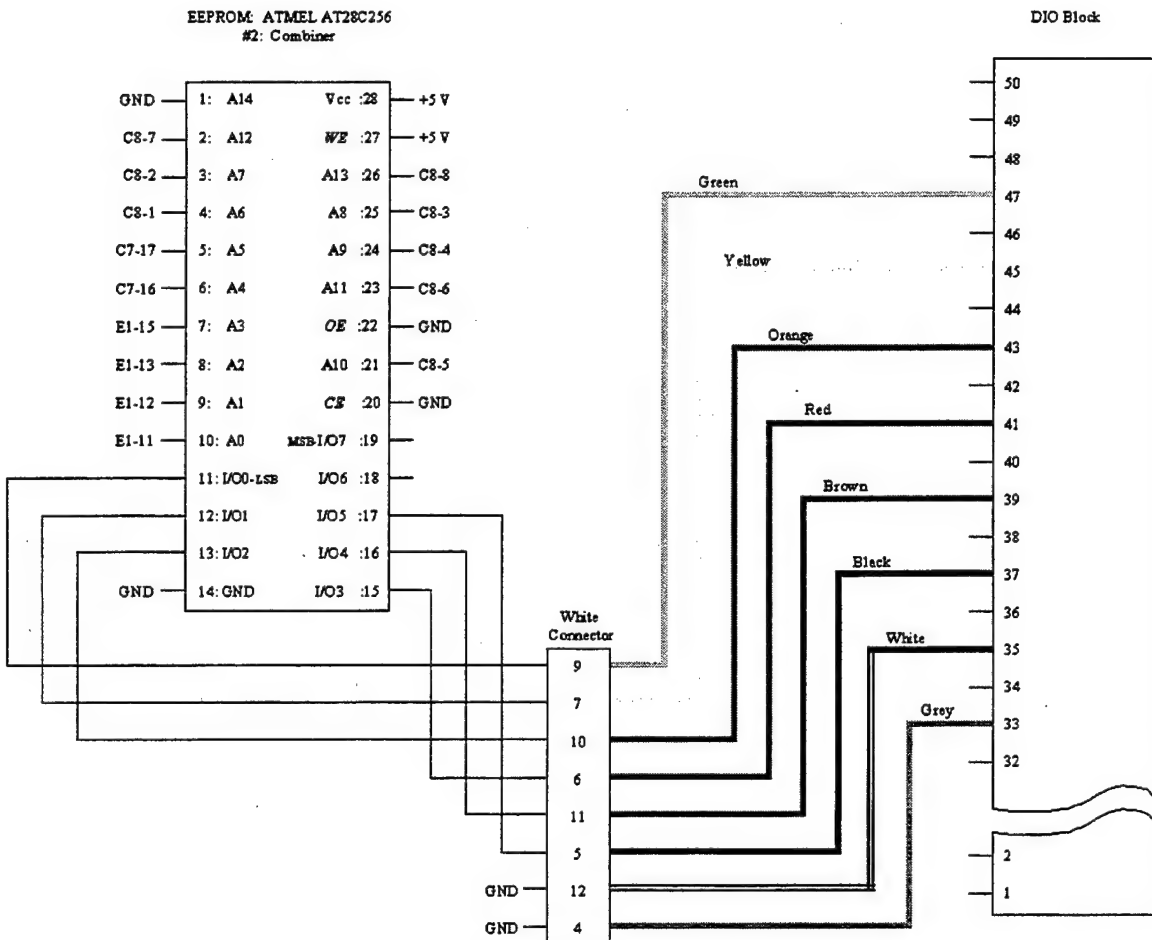


Figure 6- 16: Schematic Diagram of EEPROM #2 to DIO Board Wiring.

The LABVIEW program records the binary output to the DIO board. The transfer function is completed when a MATLAB routine (*AOA_map.m*) converts the bin number to an estimated angle of arrival.

VII. TEST AND EVALUATION OF PROTOTYPE HARDWARE

A. ANECHOIC CHAMBER AND TEST PROCEDURE

The prototype antenna is tested in the Naval Postgraduate School Microwave Anechoic Chamber. The major components and communication paths used for testing are shown in Figure 7-1. The test system architecture centerpiece is a 486 computer. One of two LABVIEW programs controls the test via a General Purpose Interface Bus (GPIB), the Serial port, and a PC-DIO-96 board. The local oscillator that produces the radiated signal is located on a Hewlett Packard 8510 Vector Network Analyzer (VNA). In the anechoic chamber, a standard gain feed horn transmits the microwave signal generated by the local oscillator. The antenna is placed on a pedestal (Figure 7-1) approximately 12 feet from the transmitting horn with the microwave circuit mounted on the back of the array ground plane. A servomotor is controlled through the computer Serial port and rotates the pedestal with a best resolution of 0.1 degrees. The microwave circuit continuously analyzes the received signal, and at each resolution step the phase detector output is sampled. The phase detector output is carried out of the anechoic chamber on RG-59 coaxial cables. The digital circuits process the phase detector output. The 6-bit output of the digital circuit is transmitted to the computer via the DIO board. Two HP 3478A digital multimeters measure either the phase detector output or the shift and bias circuit output. The computer samples the multimeters through the GPIB bus. The experiment control and recording equipment are shown in Figure 7 - 2.

The data collection and processing technique is illustrated in Figure 7 - 3. Two types of tests are conducted depending upon the parameter of interest. The first test measures the output of the phase detector, and other test measures the output of the shift and bias amplifier and the binary angle of arrival estimation simultaneously. One LABVIEW program is written for each test, so the tests cannot be run concurrently. These programs are presented in Appendix B. When the phase detector output is measured, the procedure follows the left path on Figure 7 - 3. The phase detector output

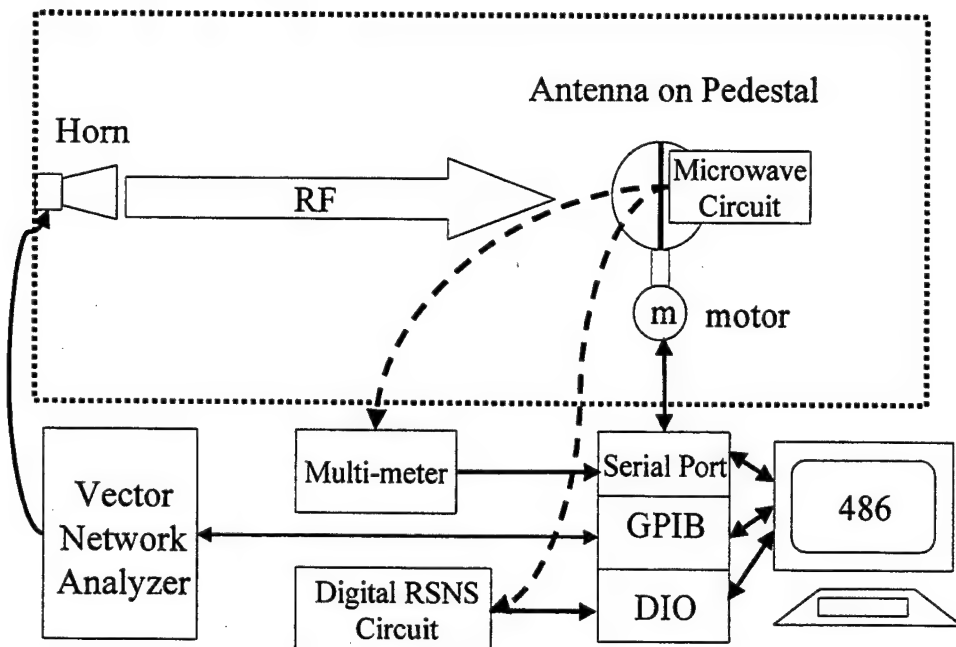


Figure 7 - 1: Anechoic Chamber Configuration.

of each channel is connected to a multimeters via an RG-59 coaxial cable. The LABVIEW VI code *DF_mm_R2* samples the multimeters at each servomotor step. The data is saved in column format. The four columns of data are (1) antenna position, (2) channel 1 (modulus 17) multimeter output, (3) antenna position, and (4) channel 2 (modulus 8) multimeter output. This data is physically transported from the lab on a diskette. The data is opened in Microsoft Excel using the “text-tab delimited” format. Manual normalization of the data is performed. The minimum and maximum values of the phase detector folding waveforms are located. A column is inserted between the second and third data columns. The normalized phase detector output $\eta_{i,norm}$ is calculated using the equations:

$$\bar{\eta} = (\eta_{\max} + \eta_{\min})/2, \quad (7.1)$$

$$\Delta\eta = (\eta_{\max} - \eta_{\min})/2, \quad (7.2)$$

$$\eta_{i,norm} = \frac{\eta_i - \bar{\eta}}{\Delta\eta}. \quad (7.3)$$

The normalized output for each channel is placed in the new third column (modulus 17) and the sixth columns (modulus 8).

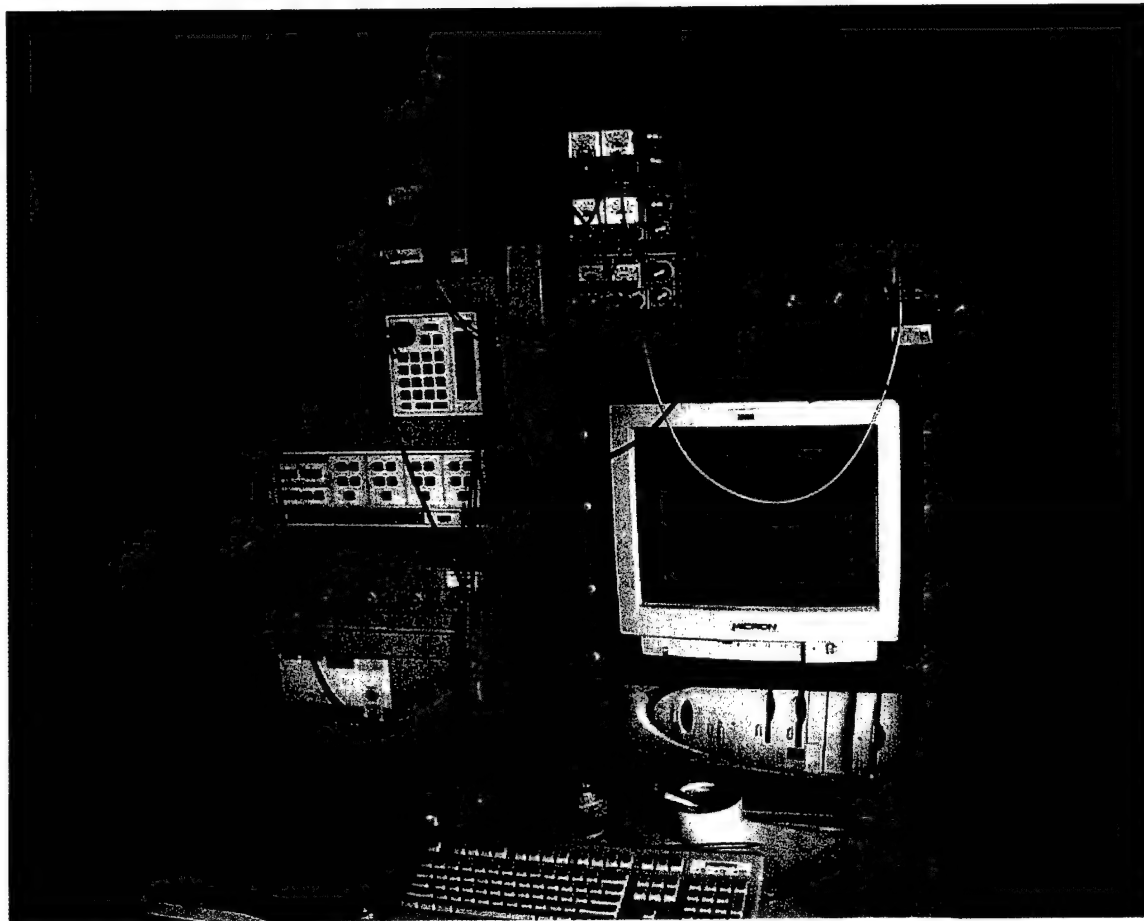


Figure 7 - 2: Anechoic Chamber Control and Recording Equipment.

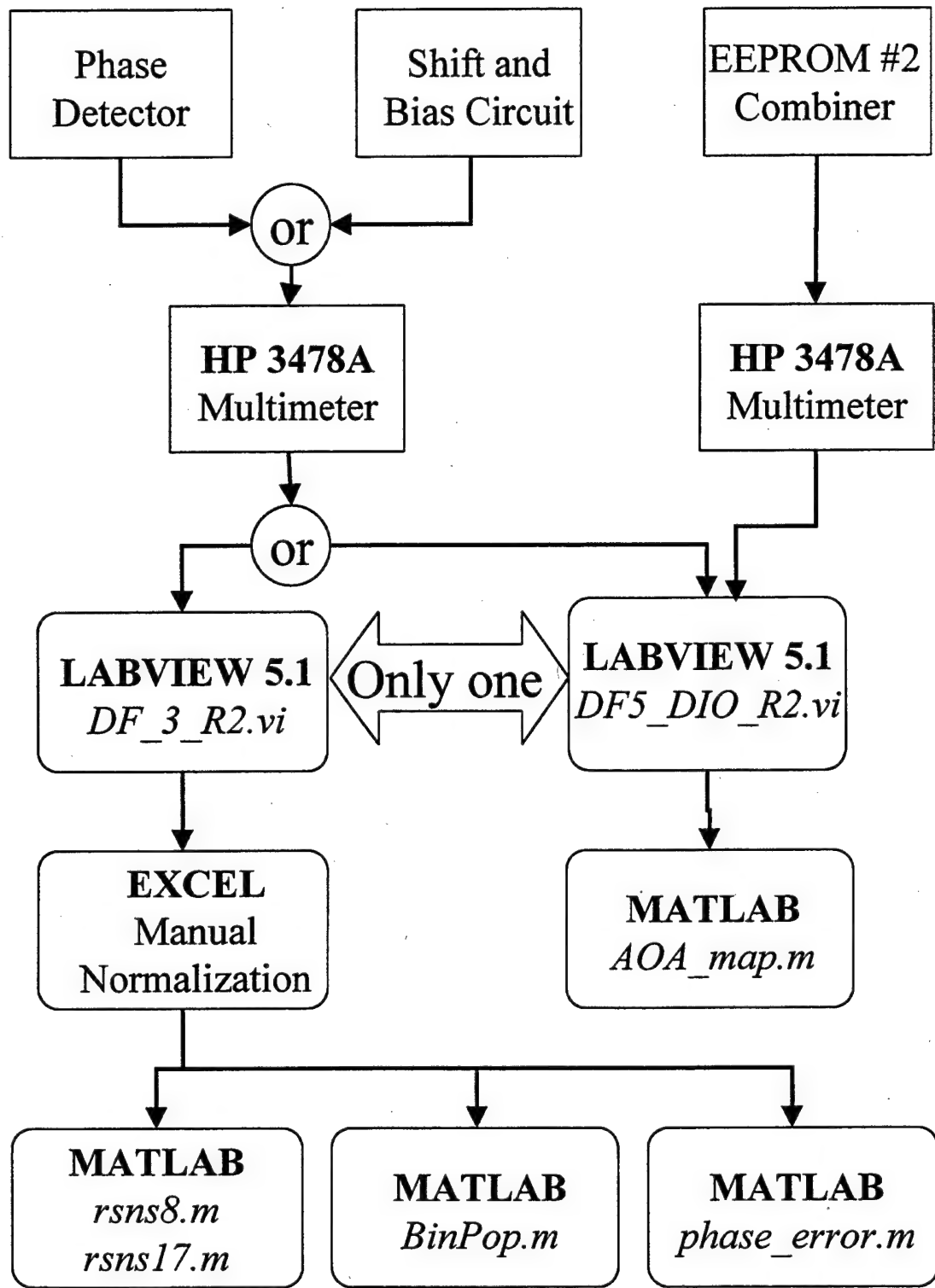


Figure 7 - 3: Data Collection Flow Chart.

The normalized phase detector output is saved in tab delimited text format with a “.dat” extension. This is the standard input format for the MATLAB processing programs provided in Appendix A. The measured phase detector output is visually compared to simulated data using the *rsns8.m* and *rsns17.m* programs. *Phase_error.m* calculates and plots the phase error between a simulated and normalized measured phase detector output. The normalized phase detector output is passed through a simulation of the digital processing in *Bin_Pop.m*. If the output of the shift and bias circuit is connected to the multimeters rather than the phase detector output, the same collection and processing may be conducted on this signal; however, this specific configuration was not used in this thesis.

The output of the digital circuit follows the path on the right of Figure 7 - 3. Either the phase detector or shift and bias circuit output is connected to the multimeters. The binary output of the digital circuit is connected to the computer via the DIO board. The LABVIEW VI code *DF5_DIO_R2* samples the multimeters and DIO board at each servomotor step. The data is again saved in column format and must be transported, and opened as before. No normalization is required for this data, but it must be saved in tab delimited text format with a “.dat” extension. Analysis of the data is performed by one program, *AOA_map.m*. This program plots the folding waveforms and the bin mapping. It converts the bin numbers into an estimated angle of arrival and plots the transfer function.

The duration of a test depends upon the desired resolution of the test. For the *DF_mm_R2* measurement of the analog data, a 0.5° resolution test duration is 25 minutes and a high (0.1°) resolution test requires approximately two hours to complete. The low-resolution measurements are used for initial phasing of the microwave circuits, and high resolution measurements are used for detailed analysis of the antenna performance. The digital output sampling program, *DF5_DIO_R2*, requires 9 hours for a high resolution test. The program can conduct low resolution tests, but none were conducted for this thesis research.

B. UNSCALED ANTENNA RESULTS

Two antennas have been built and tested. The first antenna is unscaled ($\xi=1$). The second antenna is scaled for a 60° field of view ($\xi = \sqrt{3}/2$). Both have been tested at a resolution of 0.1° . The results from each antenna will be presented individually beginning with the unscaled antenna. Figure 7 - 4 shows the normalized modulus 8 phase detector output output. The solid line represents the simulated results and the dashed line shows the measured results. The phase adjusters are tuned to achieve the best fit between the measured and simulated results. Figure 7 - 5 shows the same results for the normalized modulus 17 phase detector output.

Figure 7 - 6 plots the phase difference between the simulated and measured results. *Phase_error.m* finds the difference between the arccosines of the simulated and normalized phase detector output data of Figure 7 - 4 and Figure 7 - 5. The comparator thresholds are spaced uniformly in phase, so phase errors larger than one comparator step in the measured mixer output disrupts the thermometer code. Minimizing the phase error is critical to the success of the RSNS architecture. The normalized measured phase detector output is processed by the simulated transfer function using *BinPop.m* in Figure 7 - 7. This figure clearly shows that the large phase errors observed in Figure 7 - 6 prevent the RSNS system from properly estimating the angle of arrival. The RSNS circuit maps the angles of arrival with small phase ($-30^\circ \leq \theta \leq 0^\circ$) errors without difficulty.

The phase detector output is the input of the shift and bias circuit. The variable resistors R_1 and R_2 in the shift and bias circuit are used to tune the shift and bias circuit. The output of the shift and bias circuit is shown as Figure 7 - 8. The comparator networks process the shift and bias output and are subsequently processed by the EEPROM. The digital output of the EEPROM #2 is shown as Figure 7 - 9. This output is input to the computer and is processed by *AOA_map.m* to determine the estimated angle of arrival with the results shown in Figure 7 - 10. The unscaled antenna maps from

approximately $\theta = -70^\circ$ to $\theta = +65^\circ$ with significant gaps in the processing between $0^\circ \leq \theta \leq 10^\circ$ and $35^\circ \leq \theta \leq 50^\circ$.

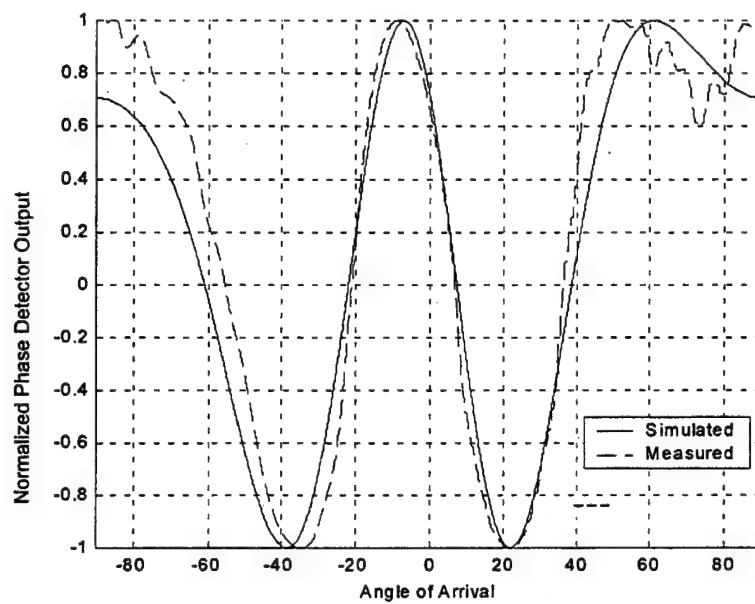


Figure 7 - 4: Unscaled Antenna, Modulus 8 Normalized Phase Detector Output.

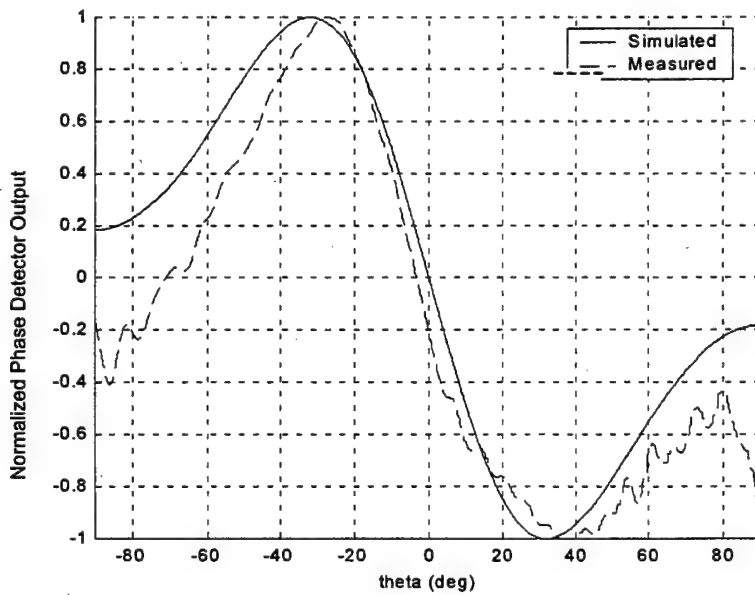


Figure 7 - 5: Unscaled Antenna, Modulus 17 Normalized Phase Detector Output.

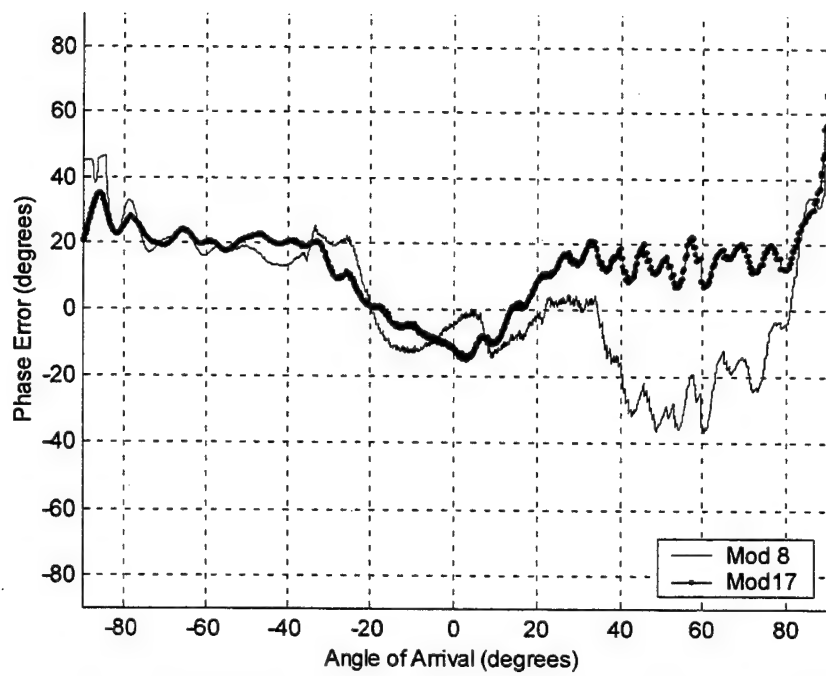


Figure 7 - 6: Phase Difference Between Simulated and Measured Waveforms, Unscaled Antenna.

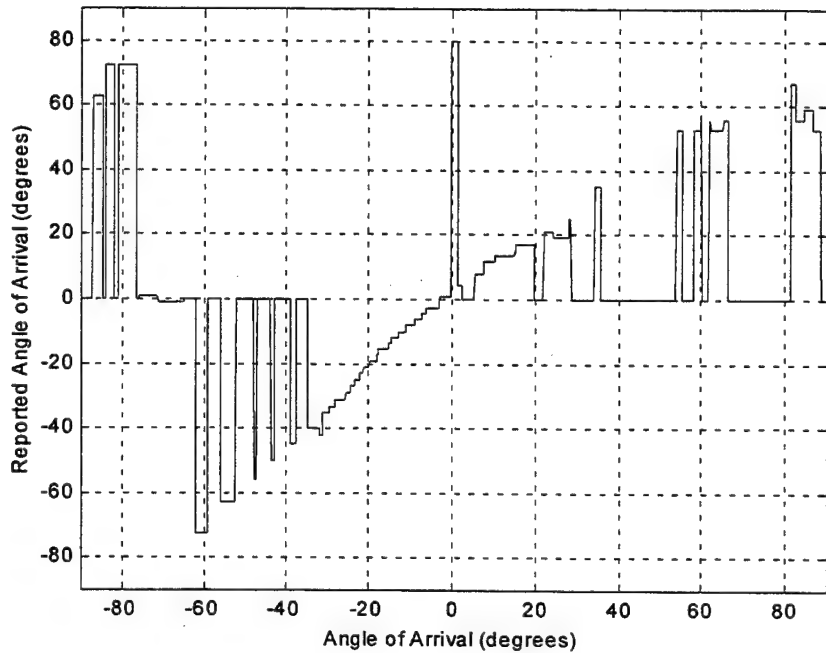


Figure 7 - 7: Measured Phase Dectector Output through Simulated Digital Circuit.

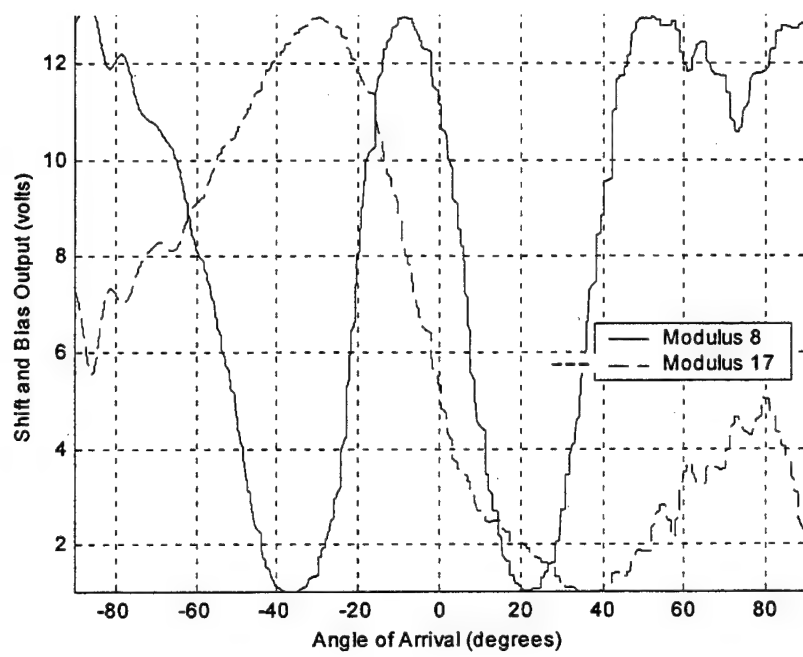


Figure 7 - 8: Unscaled Antenna, Shift and Bias Circuit Output.

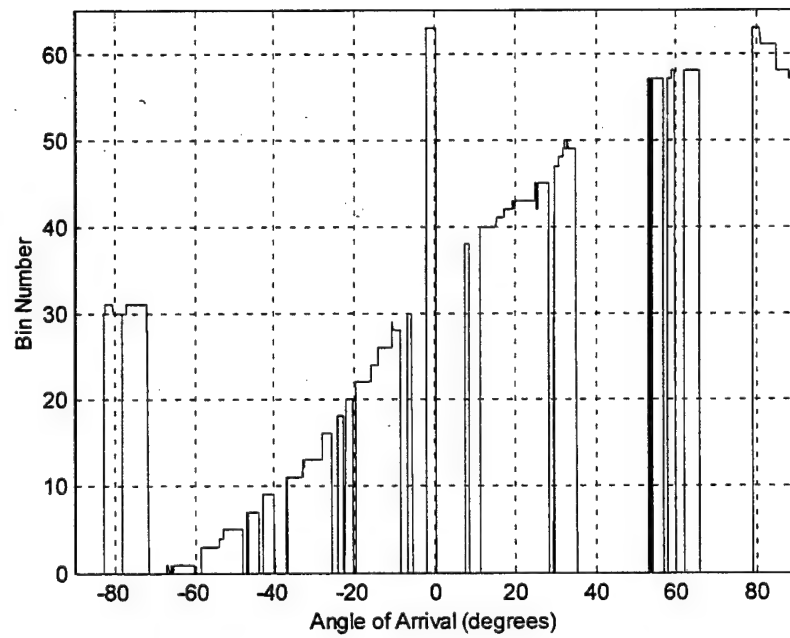


Figure 7 - 9: Bin Mapping of Unscaled Antenna.

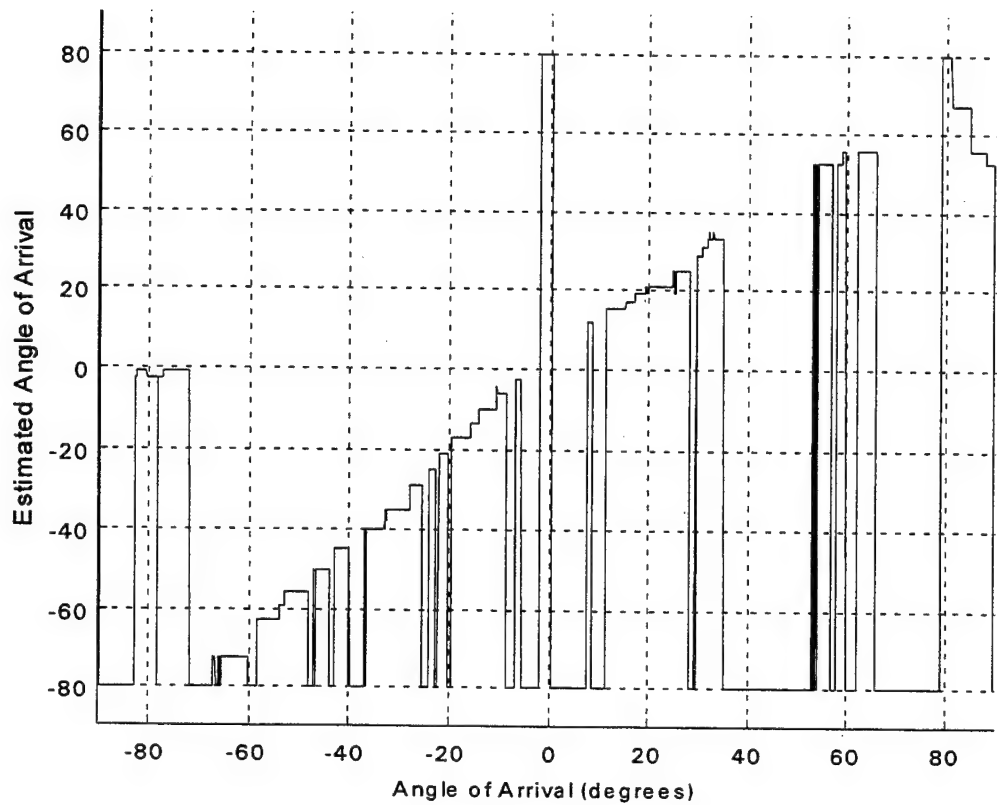


Figure 7 - 10: Transfer Function of Unscaled Antenna.

C. SCALED ANTENNA RESULTS

The phase errors shown in Figure 7 - 6 are attributed in part to mutual coupling as predicted in Figure 5-15. The scaled antenna has larger element spacings by a factor of $1/\xi = 2/\sqrt{3}$ and is designed to accommodate dummy elements. The same sequence of measurements is conducted with the scaled antenna with no dummy elements installed to investigate the effect of scaling only. Figure 7 - 11 and Figure 7 - 12 show that the folding waveforms are compressed (as expected). The phase error of the array is shown in Figure 7 - 13. The phase error for this array is smaller in magnitude for near broadside angles of arrival, but in general, the scaled antenna with no dummy elements has approximately the same phase error. The scaling compresses the mappable field of view that makes the bin widths smaller by a factor of $\sqrt{3}/2$. This makes the scaled array less tolerant of phase errors than the unscaled array. The performance of the measured mixer output when passed through the simulated digital circuit is shown in Figure 7 - 14. The shift and bias circuit output shown in Figure 7 - 15. The digital circuit processes this signal with the digital bin mapping result shown in Figure 7 - 16. The final, processed output is the estimated angle of arrival shown in Figure 7 - 17. As expected, the transfer function is steeper.

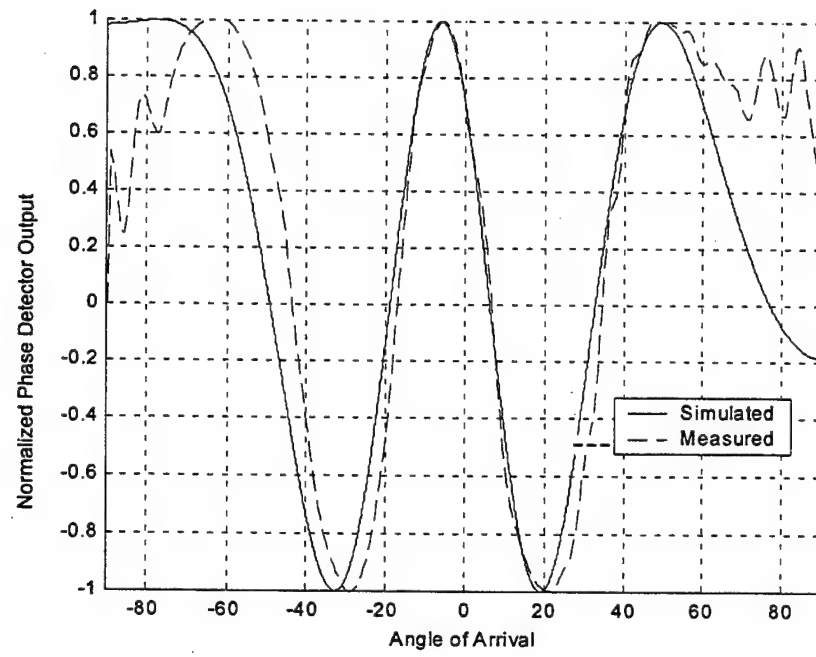


Figure 7 - 11: Scaled Antenna, Modulus 8 Phase Detector Output.

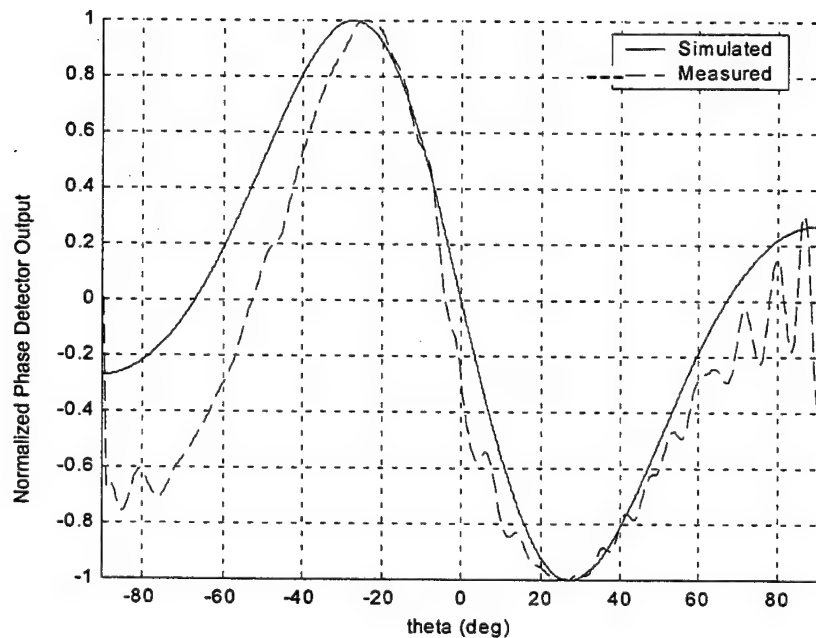


Figure 7 - 12: Scaled Antenna, Modulus 17 Phase Detector Output.

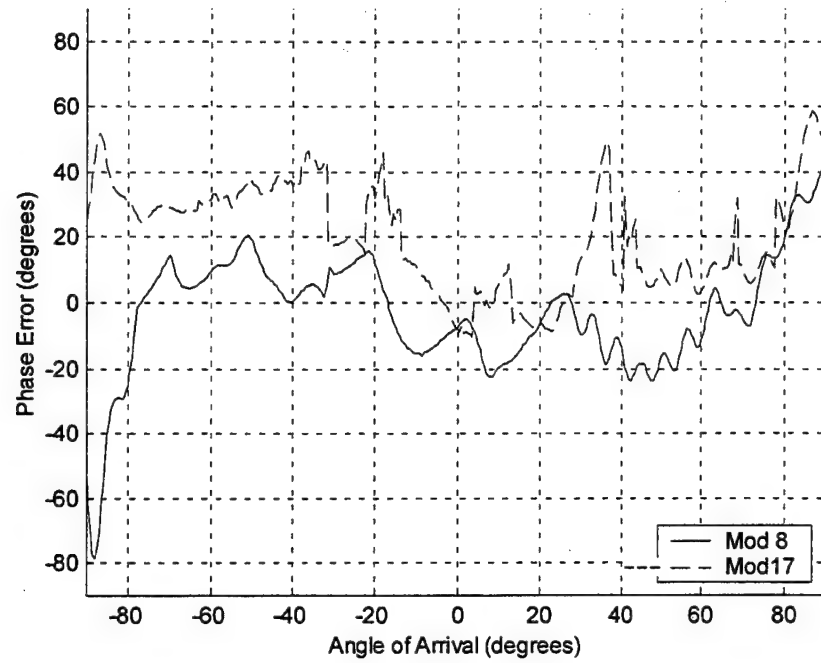


Figure 7 - 13: Phase Difference Between Simulated and Measured Waveforms, Scaled Antenna.

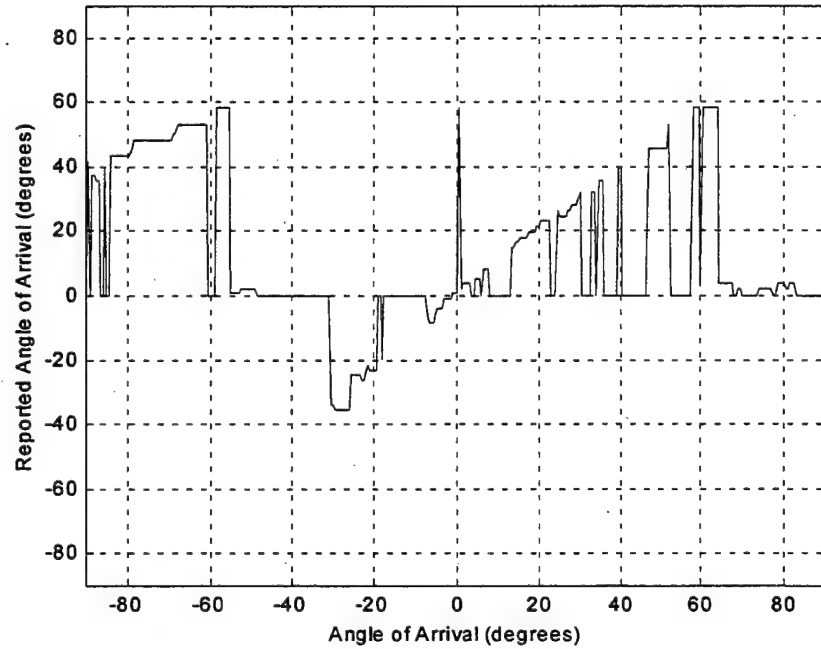


Figure 7 - 14: Measured Phase Dectector Output passed through Simulated Digital Circuit.

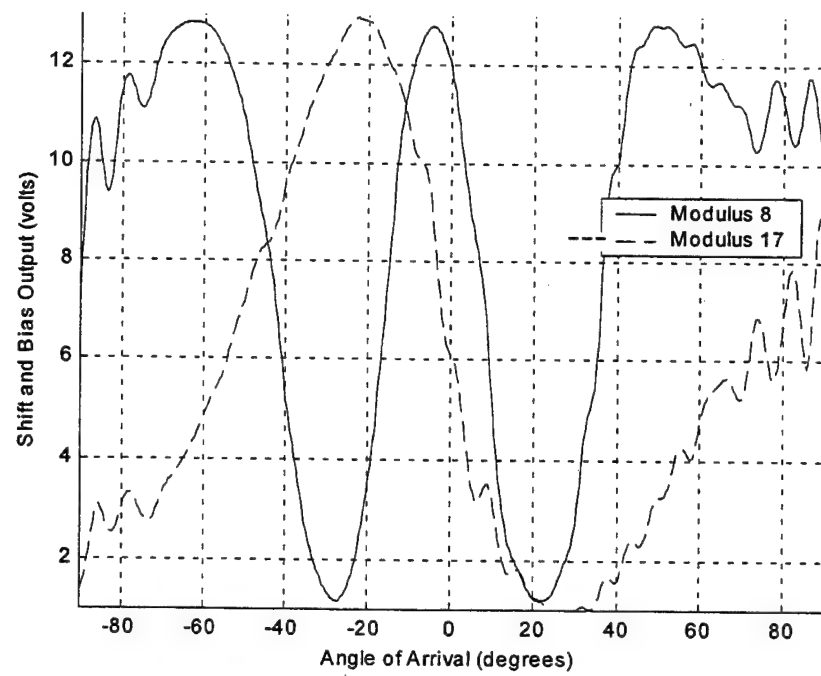


Figure 7 - 15: Shift and Bias Output, Scaled Antenna.

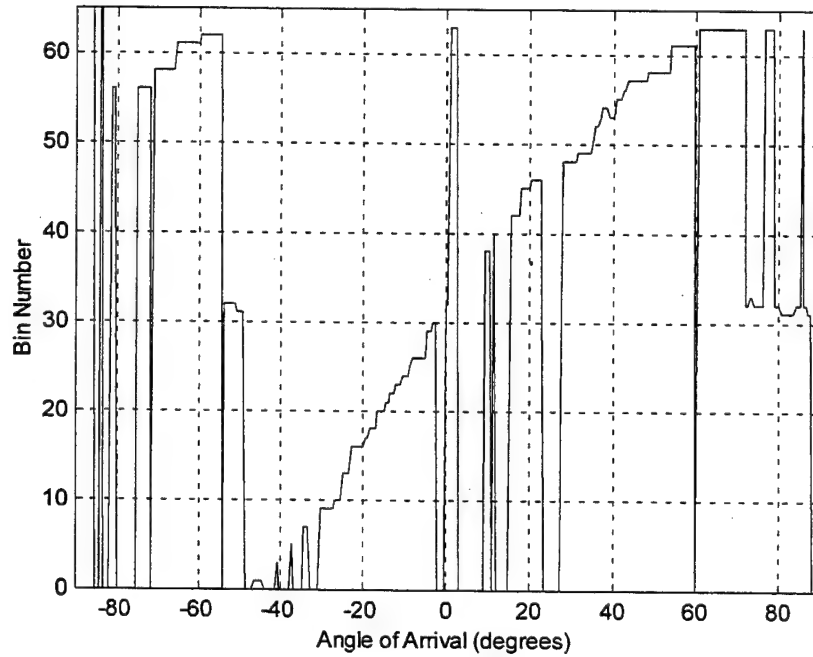


Figure 7 - 16: Scaled Antenna Bin Mapping

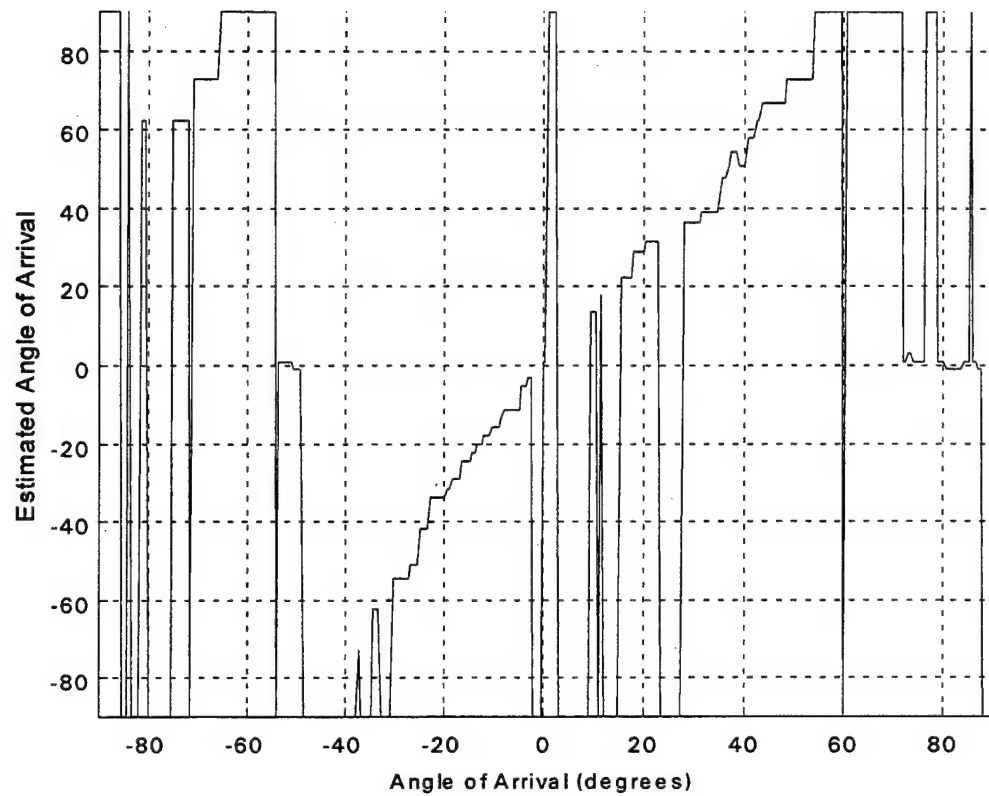


Figure 7 - 17: Scaled Antenna Transfer Function.

D. DUMMY ELEMENT INFLUENCE ON MUTUAL COUPLING

The scaled antenna is built to accommodate two pairs of dummy elements that repeat the array spacing as shown in Figure 7-18. The dummy elements are loaded with 50Ω loads and are removable. To test the impact of the dummy elements on the mutual coupling, the array is tested with no dummy elements installed, with one pair of dummy elements installed, and with both pairs of dummy elements installed. The mutual coupling-induced phase errors should be reduced by approximately 50% as shown in Figure 5-17. The results are shown for each case in Figures 7-20 through 7-22.

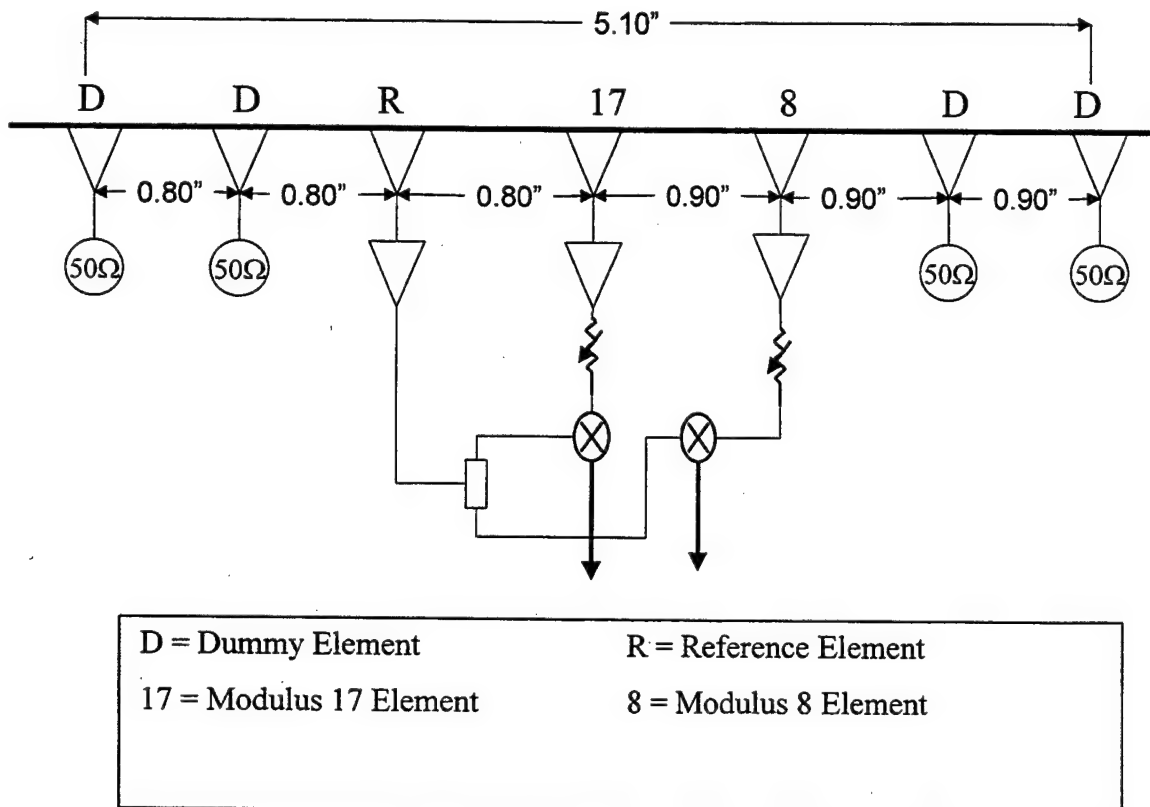


Figure 7 - 18: Scaled Array Construction with Dummy Elements.

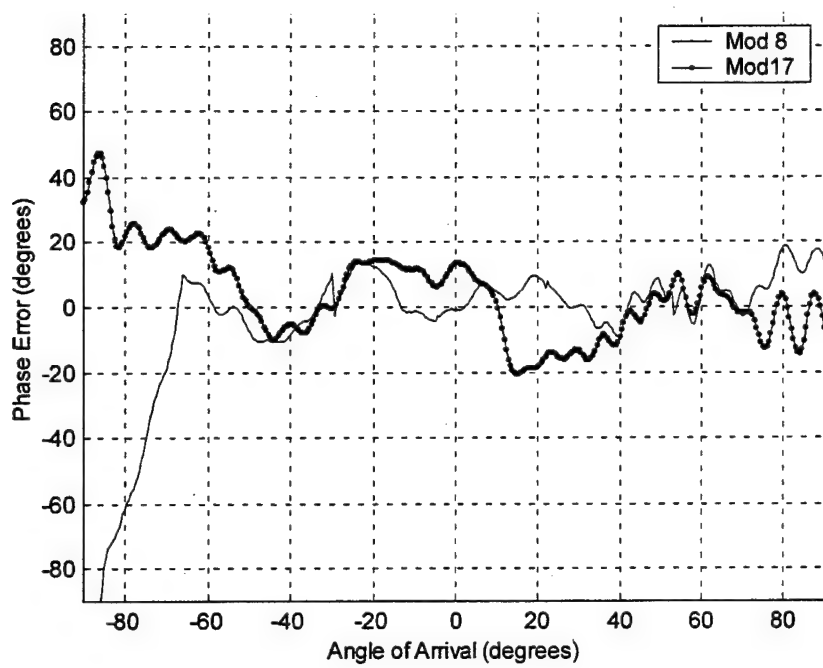


Figure 7 - 19: Phase Error Results with No Dummy Elements Installed.

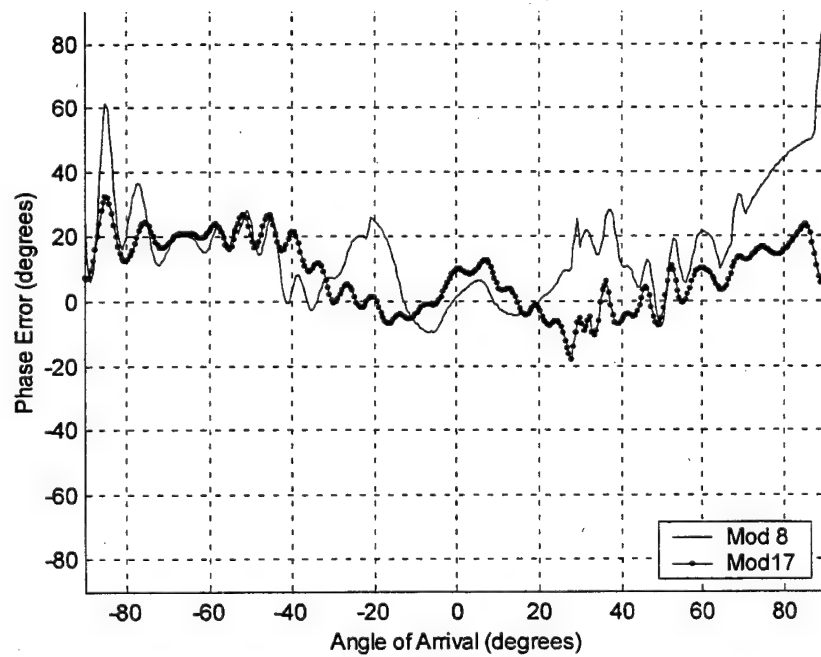


Figure 7 - 20: Phase Error Results with One Pair of Dummy Elements Installed.

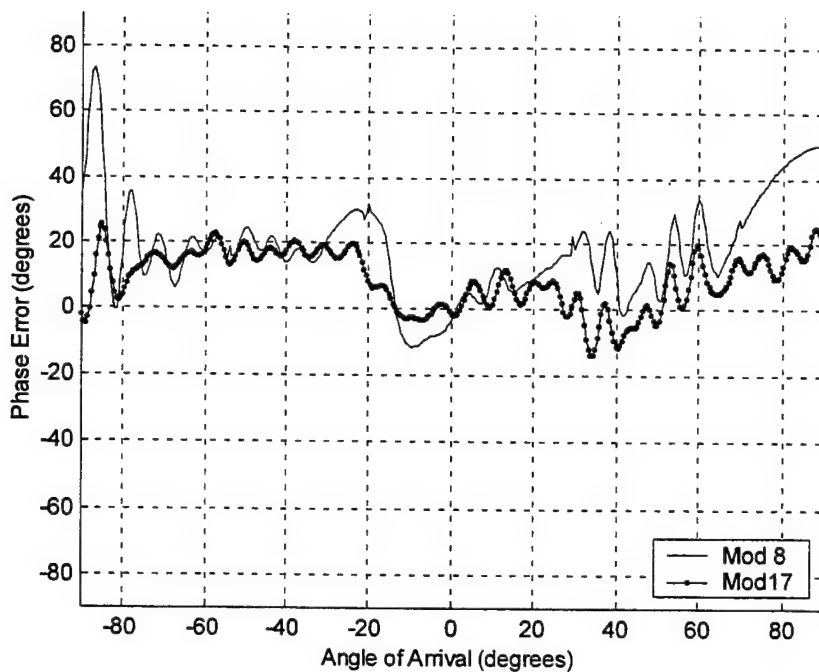


Figure 7 - 21: Phase Error Results with Two Pair of Dummy Elements Installed.

Modulus	No dummy elements installed	One pair dummy elements	Two pair of dummy elements
8	1.00	0.86	0.89
17	1.00	0.93	0.87

Table 7 - 1: Normalized RMS Phase Error for Various Dummy Element Configurations.

Table 7 - 1 summarizes the phase errors observed in each modulus for the patterns shown in Figures 7-20 through 7-22. The one dummy pair case was expected to show a phase error decrease of 50%. The observed decrease was 14% for modulus 8 and 7% for modulus 17. This indicates that mutual coupling may not be the dominant source of phase error observed in the measured data.

E. THREE CHANNEL SCALED ANTENNA RESULTS

In order to investigate the performance of the RSNS architecture in an environment with significantly less mutual coupling, the stripline elements must be replaced with channeled waveguide transitions used on the OSNS prototype. These components are too wide to fit into the array as designed. Equation 4.21 governs the element spacing. The minimum acceptable mappable aperture is 60 degrees, so ξ is already at its minimum limit ($\sqrt{3}/2$). The largest modulus channel defines the minimum spacing. In order to increase the spacing, the dynamic range must increase, but from (4.11) the dynamic range increases linearly with the modulus in a two-channel case. For this reason, a three-channel array was designed and built. The design equations are the same as the two-channel array. The geometry, predicted folding waveforms, and simulated transfer function are presented in Appendix C.

The measured phase detector outputs are shown in Figure 7 - 22, Figure 7 - 23, and Figure 7 - 24. Phase errors are evident upon a casual visual inspection of the plots. These phase errors are too large accurate bin mapping shown in Figure 7 - 25. The observed performance of the antenna in the absence of significant coupling indicates that mutual coupling is not the cause of the phase errors observed in the two-channel array. The source must be located in the microwave circuit.

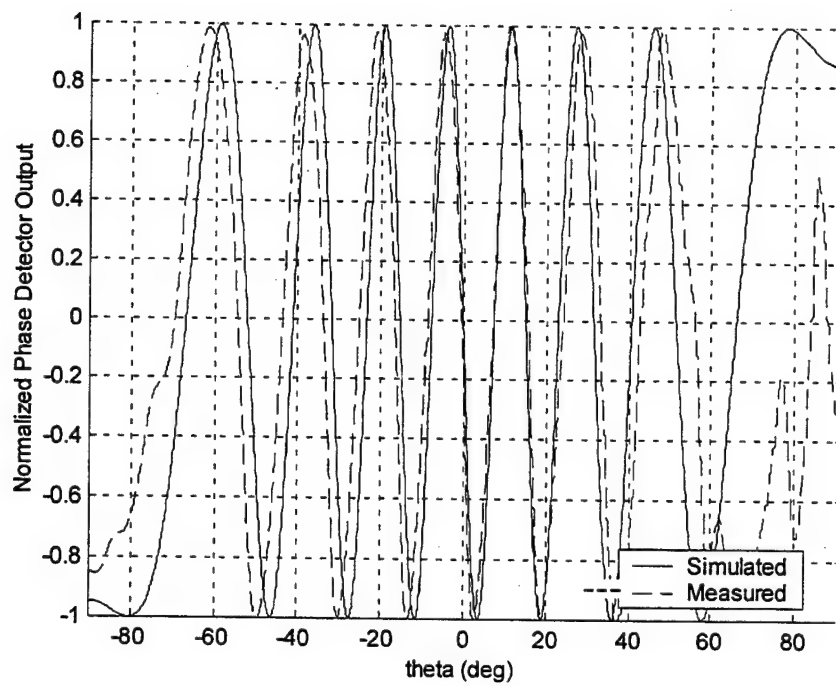


Figure 7 - 22: Normalized Measured Phase Detector Output, Three Channel Array, Modulus 6.

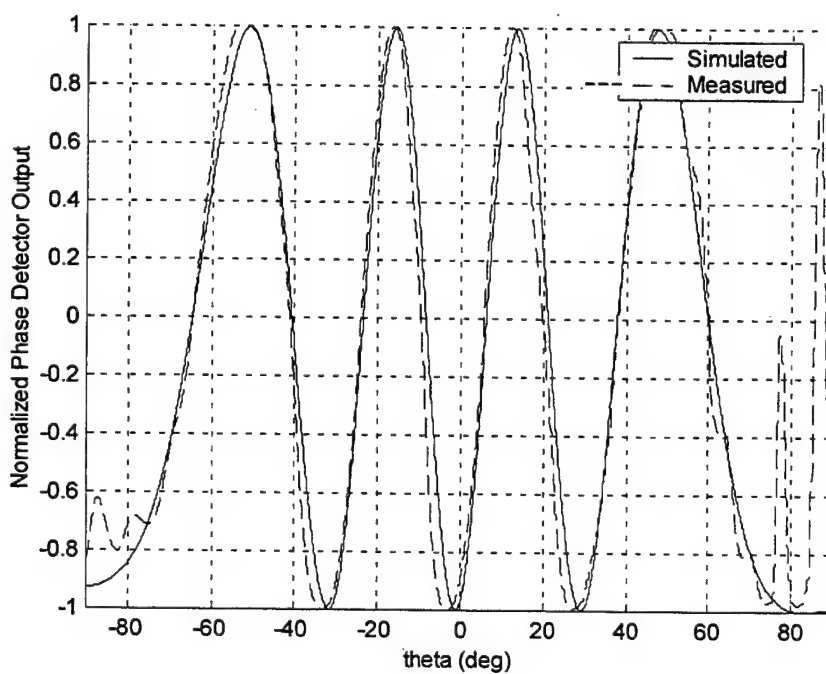


Figure 7 - 23: Normalized Measured Phase Detector Output, Three Channel Array, Modulus 11.

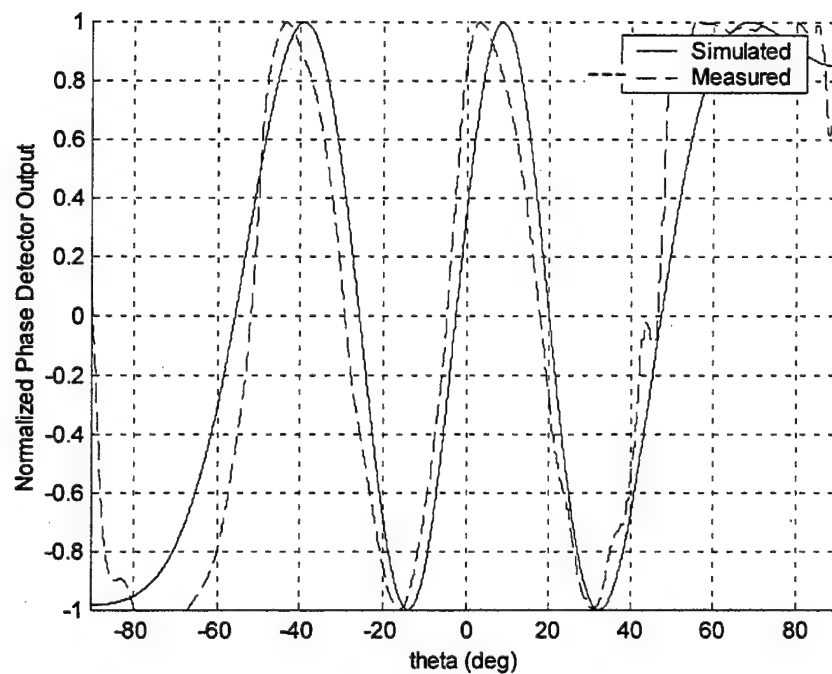


Figure 7 - 24: Normalized Measured Phase Detector Output, Three Channel Array, Modulus 17.

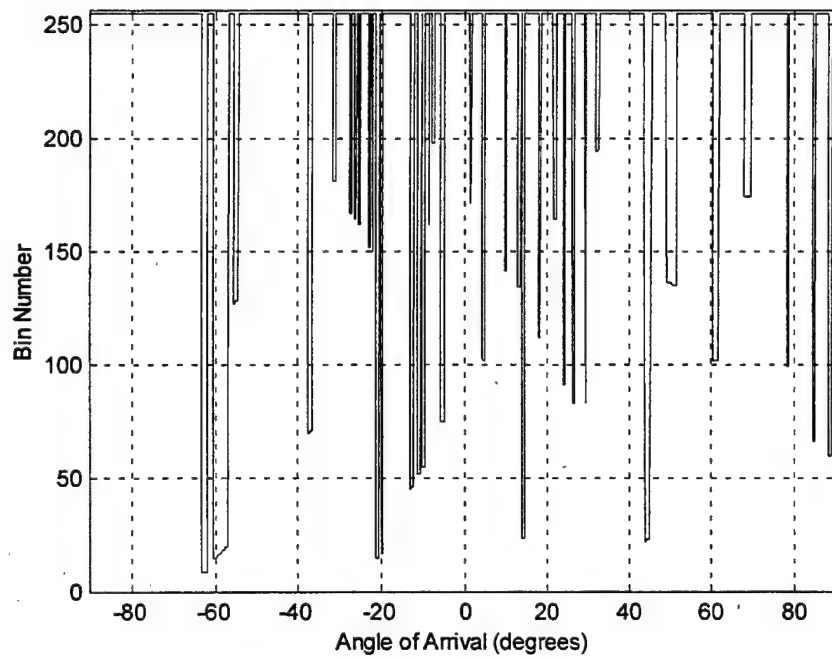


Figure 7 - 25: Three Channel Array Measured Phase Detector Output Processed by Simulated Digital Circuit.

The measured results of all three arrays have significant phase errors at the phase detector output. Three methods that reduce mutual coupling have been tested: scaling, dummy elements, and channeled waveguides. These methods have a small effect on the phase errors. Another source of phase error exists within the microwave circuit. Some alternative sources of the phase error and methods to reduce these errors are presented in the next chapter.

VIII. CONCLUSIONS

A. PROTOTYPE OUTPUT

The RSNS prototype, like all phase sampling interferometers, measures the phase difference between the reference and signal elements. The microwave circuit conditions the received signal, and folding waveforms that are a predictable function of the angle of arrival are produced by the phase detector. The digital circuit maps the phase difference at the mixer output into an estimated angle of arrival. The predicted output of the unscaled prototype array is reproduced as Figure 8 - 1. The measured phase detector output contains phase errors between the simulated and predicted results. These phase errors cause the thermometer code to incorrectly map the incident wave to the proper angle of arrival. The measured transfer function of the unscaled prototype antenna is reproduced as Figure 8 - 2.

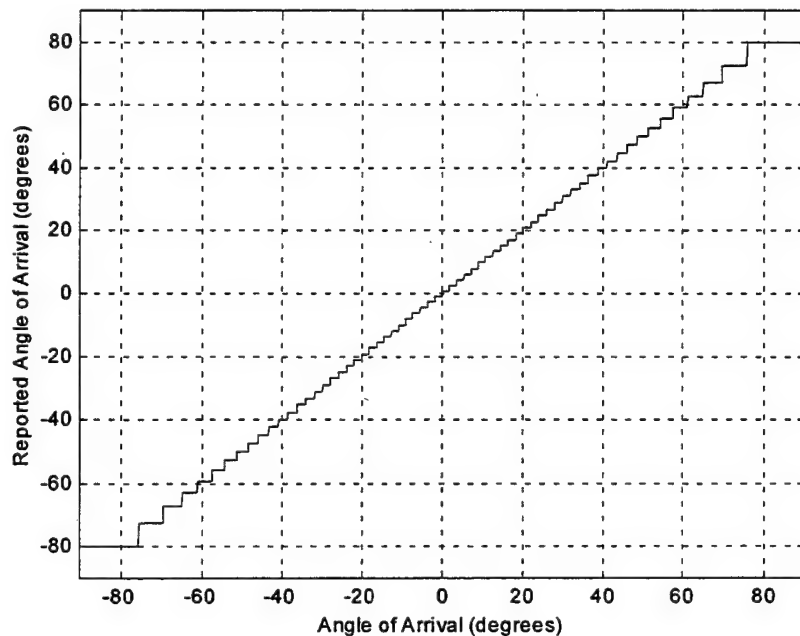


Figure 8 - 1: Simulated Transfer Function of the Unscaled Prototype Antenna.

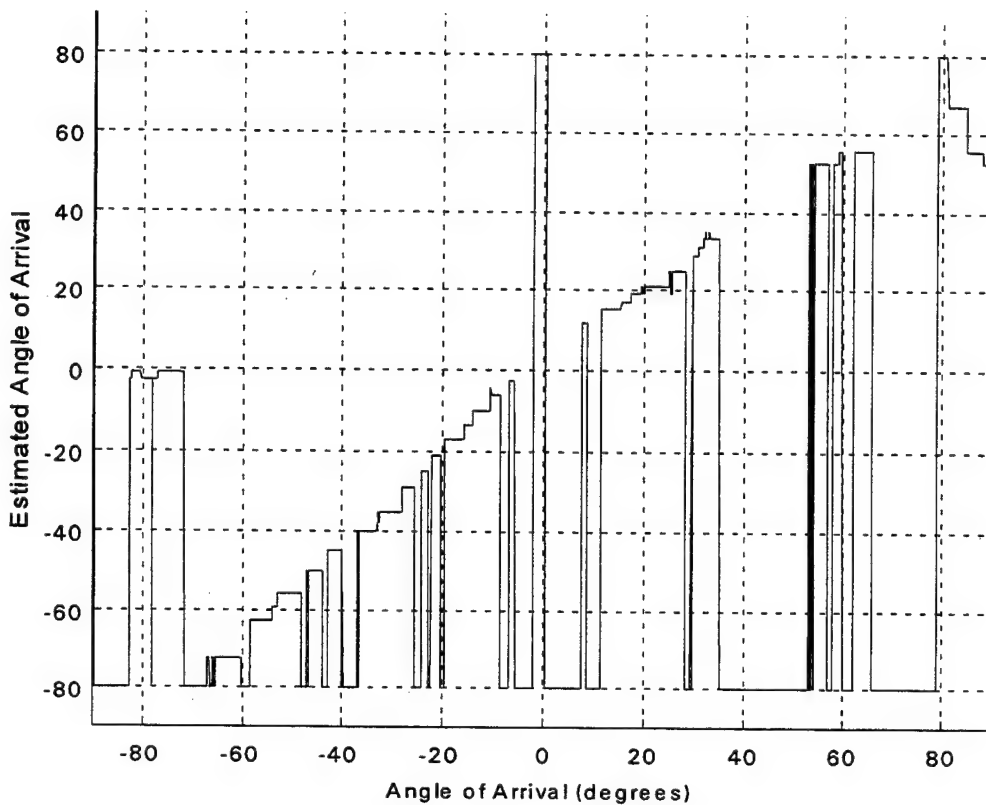


Figure 8 - 2: Measured Transfer Function of the Unscaled Prototype Antenna.

Mutual coupling is a common cause of phase errors between closely spaced antenna. In order to separate the elements, a scale factor (ξ) is derived. The scale factor is the ratio of the element spacing of the scaled and unscaled arrays. The scale factor narrows the mappable field of view of the antenna and increases the resolution within the mappable field of view. For a scale factor of $\xi = \sqrt{3}/2$, the maximum mappable aperture (θ_{MM}) is 60° . The predicted transfer function for the scaled array is reproduced as Figure 8 - 3. The mixers output still contains significant phase errors, and the increased resolution of the antenna limits the ability to process the errors. The resulting measured transfer function is reproduced as Figure 8 - 4. The steeper slope of the scaled transfer function is clearly visible when comparing Figure 8 - 2 and Figure 8 - 4.

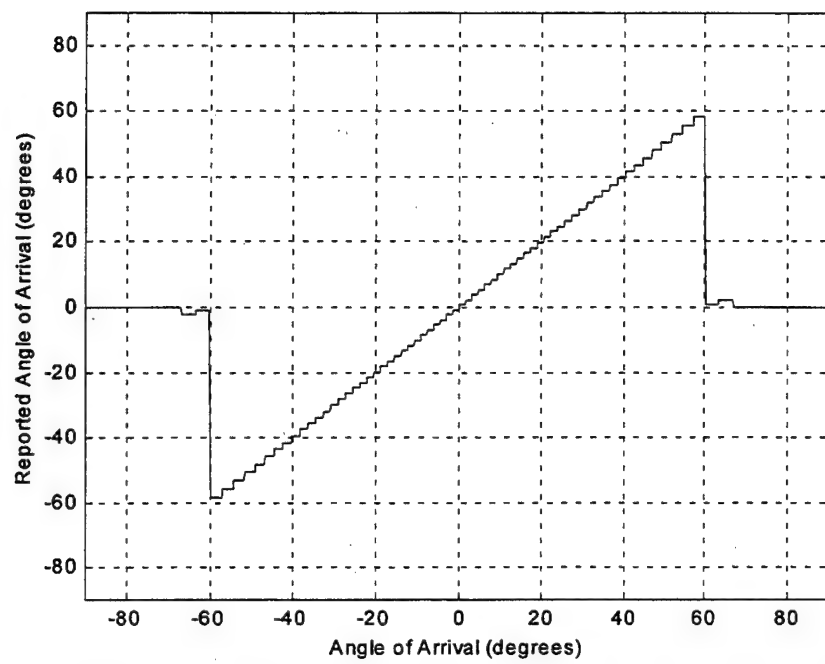


Figure 8 - 3: Simulated Transfer Function of the Scaled Prototype Antenna.

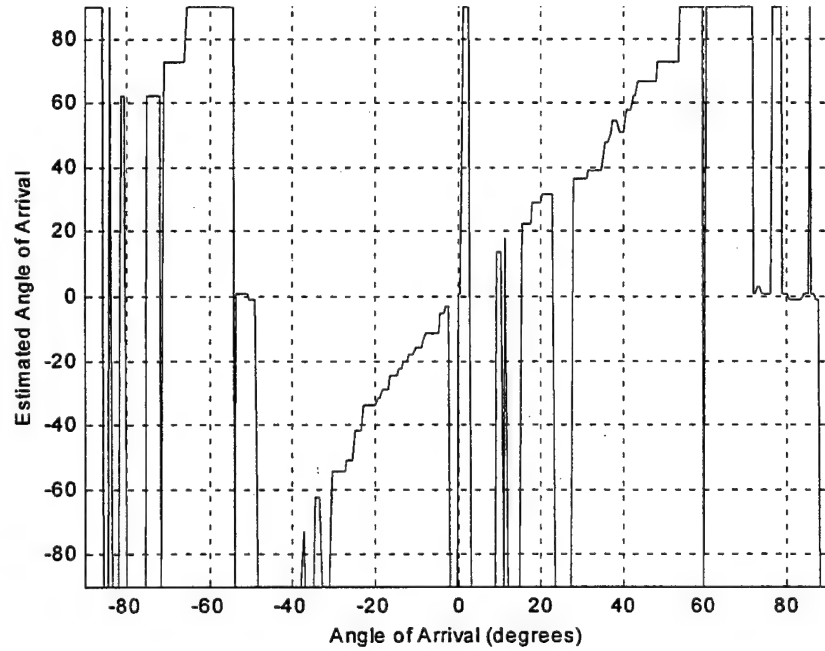


Figure 8 - 4: Measured Transfer Function of the Scaled Prototype Antenna.

The observed difference in the phase errors between the scaled and unscaled antenna does not correspond to the predicted effects of mutual coupling. An array comprised of channeled waveguide receiving elements was constructed and tested. These elements have significantly less mutual coupling, but the phase errors observed in the arrays built with stripline (dipole) elements persisted. This shows that mutual coupling is not the primary cause of the observed phase detector phase errors.

Because the antenna elements are not causing the phase errors, the microwave circuit must introduce the errors. Three likely sources are the low noise amplifiers, coaxial phase adjusters, and the rigid coaxial cable. The prototype uses three models of LNA operating in saturation. These amplifiers are not phase matched. Variations in the amplitude of the incident signal caused by the receiving element patterns may cause phase shifts in the amplifier output. Coaxial phase adjusters are a common source of noise within microwave circuits. The rigid coaxial cables that transmit the microwave signal between components are candidates for three reasons. First, the cable lengths are long and subject to thermal expansion and contraction, particularly in the vicinity of the Avantek amplifiers that get hotter than the DBS models. Second, mechanical connectors are used at the cable junctions. These components often have reflections that introduce noise into the circuit. Finally, the cables function are both transmission lines and physical support structures for the microwave circuit. The cables are subject to vibration on the rotating antenna pedestal and may randomly change the path length within each channel.

The measured results are promising. The RSNS processing is resilient against phase errors of about 15 degrees. The mixer output errors are due in part to mutual coupling, but the major source is generated within the microwave circuit. Printed microwave circuit boards and the use of common components in all channels will reduce these sources. When these analog errors are reduced, the RSNS architecture seems to be capable of mapping through the remaining mutual coupling induced phase errors.

B. FUTURE WORK

1. Phase Error Reduction

The sources of phase error in the microwave circuit are controllable. A printed circuit board will improve the performance by eliminating the coaxial cabling as an error source. When all channels have identical components, phase errors are likely to be uniform in each line and will tend to cancel. Using phase-matched amplifiers will eliminate the errors caused by using three different amplifier models. The RSNS prototype used cascaded comparators to operate in saturation. The implementation of constant output amplifiers will reduce the generation of harmonic and intermodulation product signals that contribute to the phase error.

2. Frequency Agility

The RSNS architecture faces a significant challenge in making the system frequency agile. The RSNS system is based upon a fixed broadside phase difference between the reference and signal channels. This phase difference is due to the physical path difference between the reference and signal channels. For a fixed difference in cable lengths, as the frequency varies, the phase difference also varies. Frequency invariant phase sampling techniques [1] are being studied. Another approach would use an active path length adjusting circuit to maintain the fixed phase difference.

The scale factor, ξ , was introduced as the ratio between element spacings for a fixed frequency. Because frequency and wavelength are inversely proportional, the scale factor is also equal to the reciprocal of the ratio of wavelengths. This insight enables the scale factor to be easily used to map angles of arrival for various frequencies incident upon an array with fixed element spacings. The scale factor takes the form:

$$\xi = \frac{f'}{f} \quad (8.1)$$

where f is the design frequency and f' is the measured frequency. For example, Figure 8 - 5, Figure 8 - 6 and Figure 8 - 7 show the transfer function for an unscaled antenna for

different incident frequencies. Figure 8 - 5 shows the estimated angle of arrival for the design frequency of the element spacings. The transfer function uses the entire dynamic range. Figure 8 - 6 shows the estimated angle of arrival for a signal with half the design frequency. Note that only half of the bins and consequently half of the resolution are used. This corresponds to a resolution twice as large as the design frequency. Figure 8 - 7 shows the transfer function for an incident wave with twice the design frequency. From Equation (4.22), the maximum mappable aperture is $\theta_{MM} = \arcsin(1/\xi) = \arcsin(\frac{1}{2}) = 30^\circ$. The estimated angle of arrival is determined from (4.23).

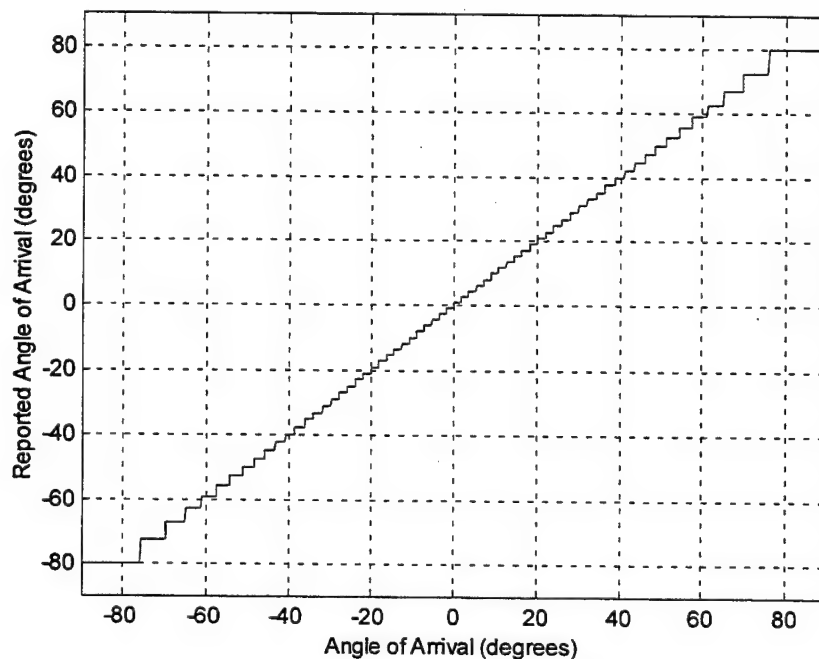


Figure 8 - 5: Simulated Transfer Function for Design Frequency.

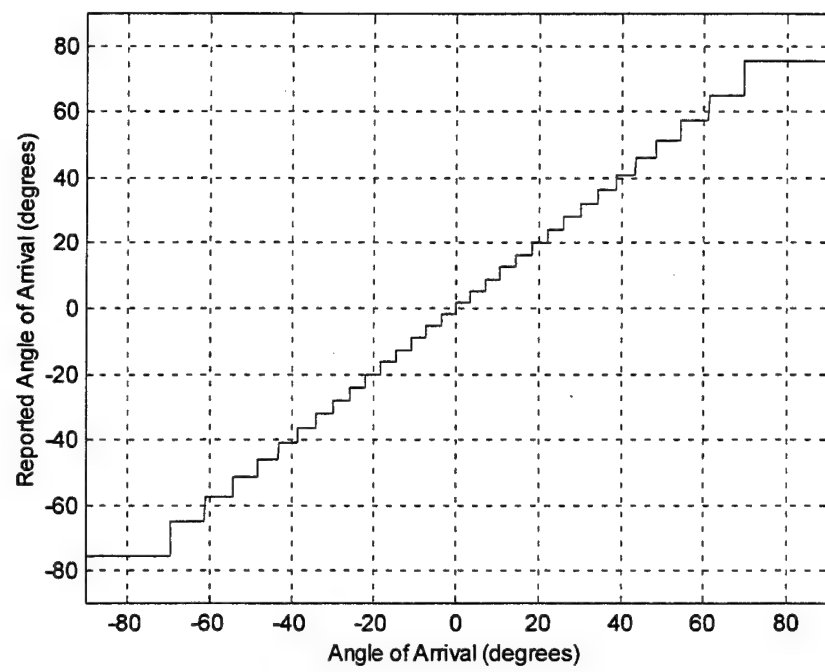


Figure 8 - 6: Simulated Transfer Function for Half Design Frequency.

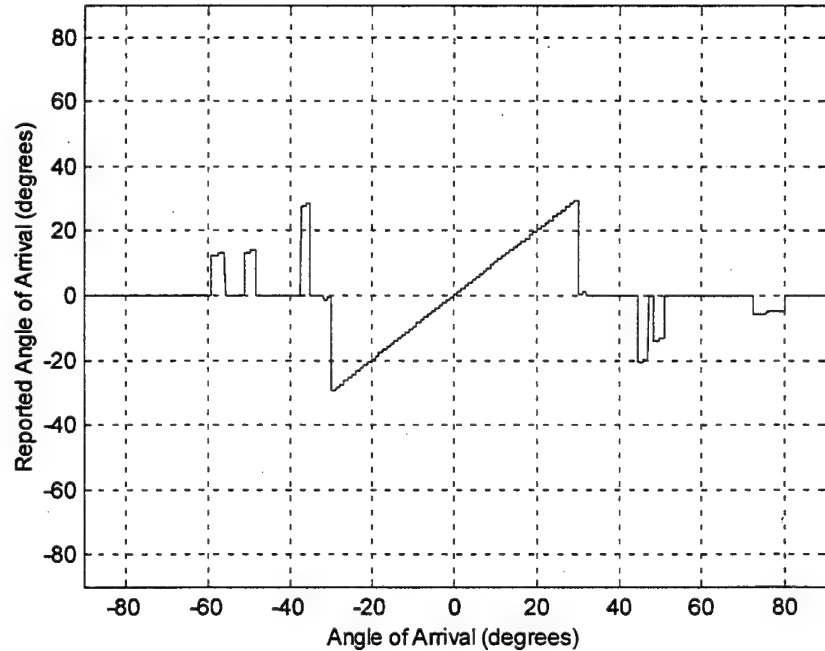


Figure 8 - 7: Simulated Transfer Function for Twice Design Frequency.

3. Multiple Signals

The prototype can be modified to process signals in a multiple signal environment through the use of narrow bandpass filters. The filter must be active to select the target signal. Further investigation into the current commercial techniques should allow this application to proceed.

4. Methods To Arrange Elements

If more than two channels are desired, the chosen modulus may require the elements to be spaced close together in order to have the required separation from the reference channel. In Figure 8 - 8, a four-channel case is presented. The moduli of {4,5,7,9} are chosen. In this case, the modulus 5 spacing would place the element close to the modulus 4 element or the modulus 7 element. By mixing the modulus 5 signal with the modulus 7 channel instead of the reference channel, the baseline is increased, but mutual coupling can be reduced.

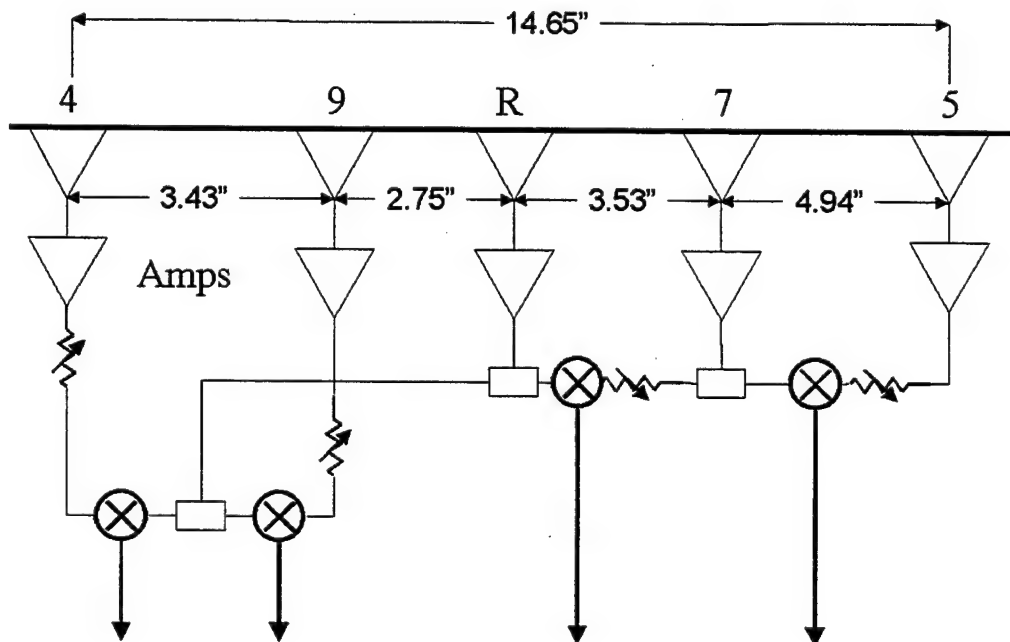


Figure 8 - 8: Possible Four Channel Geometry.

C. CONCLUDING REMARKS

This thesis research has investigated the performance of the Robust Symmetrical Number System as a technique to resolve ambiguities in phase sampling interferometry. The design equations for comparator thresholds, broadside phase difference, and a scale factor are derived. The simulated transfer function demonstrated that the RSNS antenna will have a wide instantaneous field of view and high resolution. Mutual coupling that adversely effects many phase sampling interferometers was overshadowed by other sources of phase error in the RSNS prototypes. The major source of phase errors is within the microwave circuit, but these sources can easily be reduced in future prototype generations. The simplicity of the RSNS design and absence of moving parts continue to make this architecture an attractive means to resolve ambiguities and control errors in a phase sampling interferometer.

APPENDIX A. MATLAB SIMULATION AND DATA EVALUATION CODE

This Appendix presents the codes that simulate the performance of the RSNS antenna. The first three codes simulate the antenna performance: RSNS8.m, RSNS17.m, and BinPop.m. All three can also be used to compare measured results to the predicted results. Two codes specifically designed to analyze the antenna output are also presented. These codes are AOA_map.m and phase_error.m.

%RSNS8.m WITH SCALING

```
% LT Dave Wickersham, 23 March 2000
% Generates the simulated folding waveform. Two element
arrays assumed.
% Can accept normalized mixer output for comparison to
simulated waveform.
% m = modulus; d = spacing (m); f = frequency
clear
N=2;
f=8.0e9; c=3e8; wavl=c/f;
k=2*pi/wavl;
rad=pi/180;
sf=sqrt(3)/2;           % sf is the scale factor

% ffd is forced phase difference to align signal to
required zero crossing
ffd=45; %original is 45!

% number of moduli in array design and their values
mm=[8 17]; nm=length(mm);
disp('moduli are: '), disp(mm)
% specify a modulus to plot
m=8;

% M is Dynamic Range
M=64;
% nf is number of folds
nf=M/(2*m*N);

% determines required element spacing
```

```

d=nf*wavl/sf/2;

% start, stop, increment angles
start=-90; stop=90; inc=0.1;
N=floor((stop-start)/inc)+1;

for n=1:N;
    thd(n)=start+(n-1)*inc; thr=thd(n)*rad;
    arg(n)=k*d*sin(thr);
    % mixer output
    mx(n)=cos(arg(n)+(ffd)*(pi/180));
end

load p24.dat

both8=[thd' mx']
save simu8.dat both8 -ascii

figure(1)
hold
plot(thd,mx,'k');
plot(p24(:,4),p24(:,6),'--k')
hold off
xlabel('Angle of Arrival'), ylabel('Normalized Mixer
Output');
grid
%title(['Modulus 8, p24, with ffd = ',num2str(ffd)])
legend('Simulated','Measured',0)
axis([-90,90,-1,1])
orient landscape

```

%RSNS17 WITH SCALING

```
% LT Dave Wickersham, 23 March 2000
% Generates the simulated folding waveform. Two element
arrays assumed.
% Can accept normalized mixer output for comparison to
simulated waveform.
% m = modulus; d = spacing (m); f = frequency
```

```
clear
N=2;
f=8e9; c=3e8; wavl=c/f;
sf=sqrt(3)/2;
k=2*pi/wavl;
rad=pi/180;
```

```
% ffd is forced phase difference to align signal to
required zero crossing
ffd=90; %original is 90!
```

```
m=17;
```

```
% M is Dynamic Range
M=64;
% nf is number of folds
nf=M/(2*m*N);
% calculation of required element spacing
d=nf*wavl/sf/2;

% start, stop, increment angles
start=-90; stop=90; inc=0.1;
N=floor((stop-start)/inc)+1;
```

```
for n=1:N;
    thd(n)=start+(n-1)*inc; thr=thd(n)*rad;
    arg(n)=k*d*sin(thr);
    % mixer output
    mx(n)=cos(arg(n)+(ffd)*(pi/180));
```

```
end
```

```
load p4.dat
```

```
both17=[thd' mx']
save simul7.dat both17 -ascii

figure(1)
hold
plot(thd,mx,'k');

% LABVIEW Output has mod 17 mixer output in second column.
% Normalization technique puts normalized mixer output in
third column.
plot(p4(:,1),p4(:,3),'g')

hold off
xlabel('Angle of Arrival (degrees)'), ylabel('Normalized
Mixer Output');
grid
title(['Modulus 17, p32, with ffd = ',num2str(ffd)])
legend('Modulus 17','Modulus 8',0)
axis([-90,90,-1,1])
orient landscape
```

```
%BinPop.m
```

```
% LT Dave Wickersham 23March2000

% step size is 0.1 degrees based on minimum stepper motor
resolution
% simulates the entire transfer function
% 1- determines number of active comparators at each step
for both modulus
% 2- determine bin number
% 3- determine angle of arrival

% Also calculates bin population and quantization error.

% Load either the simulated data (simu17.dat, simu8.dat)
% or the experimental data - SEE BELOW (ALSO SEE LINE 155-
156)
% Uses predicted thresholds calculated from cosine of
equally spaced angles
%*****format long;
clear;
sum_error_squared=0; Excess_RE=0;
sf=sqrt(3)/2;

load simu17.dat
load simu8.dat
df1=simu17;

%load p32.dat
%df1=[p32(:,1) p32(:,3)];

%*****point_num=1801;
Sum_AE=0;

%comparators mod 17

for i=1:point_num

    c_m17(i,[1])=i;
    c_m17(i,[2])=0;
    c_m17(i,[3])=0;
```

```

c_m17(i,[4])=0;
c_m17(i,[5])=0;
c_m17(i,[6])=0;
c_m17(i,[7])=0;
c_m17(i,[8])=0;
c_m17(i,[9])=0;
c_m17(i,[10])=0;
c_m17(i,[11])=0;
c_m17(i,[12])=0;
c_m17(i,[13])=0;
c_m17(i,[14])=0;
c_m17(i,[15])=0;
c_m17(i,[16])=0;
c_m17(i,[17])=0;
c_m17(i,[18])=0;

end

%SIMULATION THRESHOLDS
t1 = cos(33*pi/34);
t2 = cos(31*pi/34);
t3 = cos(29*pi/34);
t4 = cos(27*pi/34);
t5 = cos(25*pi/34);
t6 = cos(23*pi/34);
t7 = cos(21*pi/34);
t8 = cos(19*pi/34);
t9 = cos(17*pi/34);
t10 = cos(15*pi/34);
t11 = cos(13*pi/34);
t12 = cos(11*pi/34);
t13 = cos(9*pi/34);
t14 = cos(7*pi/34);
t15 = cos(5*pi/34);
t16 = cos(3*pi/34);
t17 = cos(pi/34);

for i=1:point_num

    % all the data points
    % c1 is the bottom comparator
    % t1 is the threshold voltage for c1 etc.

    if (df1(i,[2]))> t1

```

```

    c_m17(i,[2]) = 1;
else
    c_m17(i,[2]) = 0;
end

if (df1(i,[2]))> t2
    c_m17(i,[3]) = 1;
else
    c_m17(i,[3]) = 0;
end

if (df1(i,[2]))> t3
    c_m17(i,[4]) = 1;
else
    c_m17(i,[4]) = 0;
end

if (df1(i,[2]))> t4
    c_m17(i,[5]) = 1;
else
    c_m17(i,[5]) = 0;
end

if (df1(i,[2]))> t5
    c_m17(i,[6]) = 1;
else
    c_m17(i,[6]) = 0;
end

if (df1(i,[2]))> t6
    c_m17(i,[7]) = 1;
else
    c_m17(i,[7]) = 0;
end

if (df1(i,[2]))> t7
    c_m17(i,[8]) = 1;
else
    c_m17(i,[8])= 0;
end

if (df1(i,[2]))> t8
    c_m17(i,[9]) = 1;
else
    c_m17(i,[9]) = 0;

```

```

end

if (df1(i,[2]))> t9
  c_m17(i,[10]) = 1;
else
  c_m17(i,[10]) = 0;
end

if (df1(i,[2]))> t10
  c_m17(i,[11]) = 1;
else
  c_m17(i,[11]) = 0;
end
  if (df1(i,[2]))> t11
    c_m17(i,[12]) = 1;
else
  c_m17(i,[12]) = 0;
end

if (df1(i,[2]))> t12
  c_m17(i,[13]) = 1;
else
  c_m17(i,[13]) = 0;
end

if (df1(i,[2]))> t13
  c_m17(i,[14]) = 1;
else
  c_m17(i,[14]) = 0;
end

if (df1(i,[2]))> t14
  c_m17(i,[15]) = 1;
else
  c_m17(i,[15]) = 0;
end

if (df1(i,[2]))> t15
  c_m17(i,[16]) = 1;
else
  c_m17(i,[16]) = 0;
end

if (df1(i,[2]))> t16
  c_m17(i,[17]) = 1;

```

```

else
    c_m17(i,[17]) = 0;
end

if (df1(i,[2]))> t17
    c_m17(i,[18]) = 1;
else
    c_m17(i,[18]) = 0;
end

end
%encoding the thermometer code into a decimal number.
%rsns_m17 contains the number of comparators on at
each time
%step

for j=1:point_num

    A=c_m17(j,[2]);
    B=c_m17(j,[3]);
    C=c_m17(j,[4]);
    D=c_m17(j,[5]);
    E=c_m17(j,[6]);
    F=c_m17(j,[7]);
    G=c_m17(j,[8]);
    H=c_m17(j,[9]);
    I=c_m17(j,[10]);
    J=c_m17(j,[11]);
    K=c_m17(j,[12]);
    L=c_m17(j,[13]);
    M=c_m17(j,[14]);
    N=c_m17(j,[15]);
    O=c_m17(j,[16]);
    P=c_m17(j,[17]);
    Q=c_m17(j,[18]);

    Z=A+B+C+D+E+F+G+H+I+J+K+L+M+N+O+P+Q;

    rsns_m17(j)=Z;

end

xarray=[-90:180/1800:90];
figure(1)

```

```

plot(xarray,rsns_m17(:)),grid
xlabel('Angle of Arrival (degrees)')
ylabel('Number of Comparators')
% title('Number of Comparators on each time step for mod
17')
axis([-90 90 -1 17])

%*****
clear df1

df1=simu8;

%df1=[p32(:,4) p32(:,6)];
%*****

%comparators mod 8

for i=1:point_num

    c_m8(i,[1])=i;
    c_m8(i,[2])=0;
    c_m8(i,[3])=0;
    c_m8(i,[4])=0;
    c_m8(i,[5])=0;
    c_m8(i,[6])=0;
    c_m8(i,[7])=0;
    c_m8(i,[8])=0;
    c_m8(i,[9])=0;

end

t1 = cos(15*pi/16);
t2 = cos(13*pi/16);
t3 = cos(11*pi/16);
t4 = cos(9*pi/16);
t5 = cos(7*pi/16);
t6 = cos(5*pi/16);
t7 = cos(3*pi/16);
t8 = cos(pi/16);

for i=1:point_num

    % all the data points
    % c1 is the bottom comparator
    % t1 is the threshold voltage for c1 etc

```

```
if (df1(i,[2]))> t1
    c_m8(i,[2]) = 1;
else
    c_m8(i,[2]) = 0;
end

if (df1(i,[2]))> t2
    c_m8(i,[3]) = 1;
else
    c_m8(i,[3]) = 0;
end

if (df1(i,[2]))> t3
    c_m8(i,[4]) = 1;
else
    c_m8(i,[4]) = 0;
end

if (df1(i,[2]))> t4
    c_m8(i,[5]) = 1;
else
    c_m8(i,[5]) = 0;
end

if (df1(i,[2]))> t5
    c_m8(i,[6]) = 1;
else
    c_m8(i,[6]) = 0;
end

if (df1(i,[2]))> t6
    c_m8(i,[7]) = 1;
else
    c_m8(i,[7]) = 0;
end

if (df1(i,[2]))> t7
    c_m8(i,[8]) = 1;
else
    c_m8(i,[8]) = 0;
end

if (df1(i,[2]))> t8
    c_m8(i,[9]) = 1;
```

```

    else
        c_m8(i,[9]) = 0;
    end

end

%encoding the thermometer code into a decimal number.
%rsns_m8 contains the number of comparators on at
each time
%step

for j=1:point_num

    A=c_m8(j,[2]);
    B=c_m8(j,[3]);
    C=c_m8(j,[4]);
    D=c_m8(j,[5]);
    E=c_m8(j,[6]);
    F=c_m8(j,[7]);
    G=c_m8(j,[8]);
    H=c_m8(j,[9]);
    Z=A+B+C+D+E+F+G+H;

    rsns_m8(j)=Z;

end

figure(2)
plot(xarray,rsns_m8(:),'r'),grid
xlabel('Angle of Arrival (degrees)')
ylabel('Number of Comparators')
% title('Number of Comparators on each time step for m8')
axis([-90 90 -1 8])

figure(3)
hold on
plot(xarray,rsns_m17(:),'k')
plot(xarray,rsns_m8(:),'.-k')
hold off
xlabel('Angle of Arrival (degrees)')
ylabel('Number of Comparators')
legend('Mod 8','Mod 17',0)
%title('Number of Comparators on each time step for mod 17
& mod 8')
axis([-90 90 0 17])

```

orient landscape

```
% integers for trans_funct file
bin=-1; bin_ctr=1; start_th=-90; end_th=0;
sum_error_squared=0;

% Bin mapping for thermometer code.  doa is the bin number.
for s=1:point_num

    if (rsns_m17(s)==10 & rsns_m8(s)==6)
        doa(s) = 0;

    elseif (rsns_m17(s)==10 & rsns_m8(s)==5)
        doa(s) = 1;

    elseif (rsns_m17(s)==11 & rsns_m8(s)==5)
        doa(s) = 2;

    elseif (rsns_m17(s)==11 & rsns_m8(s)==4)
        doa(s) = 3;

    elseif (rsns_m17(s)==12 & rsns_m8(s)==4)
        doa(s) = 4;

    elseif (rsns_m17(s)==12 & rsns_m8(s)==3)
        doa(s) = 5;

    elseif (rsns_m17(s)==13 & rsns_m8(s)==3)
        doa(s) = 6;

    elseif (rsns_m17(s)==13 & rsns_m8(s)==2)
        doa(s) = 7;

    elseif (rsns_m17(s)==14 & rsns_m8(s)==2)
        doa(s) = 8;

    elseif (rsns_m17(s)==14 & rsns_m8(s)==1)
        doa(s) = 9;

    elseif (rsns_m17(s)==15 & rsns_m8(s)==1)
        doa(s) = 10;

    elseif (rsns_m17(s)==15 & rsns_m8(s)==0)
        doa(s) = 11;
```

```
elseif (rsns_m17(s)==16 & rsns_m8(s)==0)
doa(s) = 12;

elseif (rsns_m17(s)==16 & rsns_m8(s)==1)
doa(s) = 13;

elseif (rsns_m17(s)==17 & rsns_m8(s)==1)
doa(s) = 14;

elseif (rsns_m17(s)==17 & rsns_m8(s)==2)
doa(s) = 15;

elseif (rsns_m17(s)==16 & rsns_m8(s)==2)
doa(s) = 16;

elseif (rsns_m17(s)==16 & rsns_m8(s)==3)
doa(s) = 17;

elseif (rsns_m17(s)==15 & rsns_m8(s)==3)
doa(s) = 18;

elseif (rsns_m17(s)==15 & rsns_m8(s)==4)
doa(s) = 19;

elseif (rsns_m17(s)==14 & rsns_m8(s)==4)
doa(s) = 20;

elseif (rsns_m17(s)==14 & rsns_m8(s)==5)
doa(s) = 21;

elseif (rsns_m17(s)==13 & rsns_m8(s)==5)
doa(s) = 22;

elseif (rsns_m17(s)==13 & rsns_m8(s)==6)
doa(s) = 23;

elseif (rsns_m17(s)==12 & rsns_m8(s)==6)
doa(s) = 24;

elseif (rsns_m17(s)==12 & rsns_m8(s)==7)
doa(s) = 25;

elseif (rsns_m17(s)==11 & rsns_m8(s)==7)
doa(s) = 26;
```

```
elseif (rsns_m17(s)==11 & rsns_m8(s)==8)
doa(s) = 27;

elseif (rsns_m17(s)==10 & rsns_m8(s)==8)
doa(s) = 28;

elseif (rsns_m17(s)==10 & rsns_m8(s)==7)
doa(s) = 29;

elseif (rsns_m17(s)==9 & rsns_m8(s)==7)
doa(s) = 30;

elseif (rsns_m17(s)==9 & rsns_m8(s)==6)
doa(s) = 31;

elseif (rsns_m17(s)==8 & rsns_m8(s)==6)
doa(s) = 32;

elseif (rsns_m17(s)==8 & rsns_m8(s)==5)
doa(s) = 33;

elseif (rsns_m17(s)==7 & rsns_m8(s)==5)
doa(s) = 34;

elseif (rsns_m17(s)==7 & rsns_m8(s)==4)
doa(s) = 35;

elseif (rsns_m17(s)==6 & rsns_m8(s)==4)
doa(s) = 36;

elseif (rsns_m17(s)==6 & rsns_m8(s)==3)
doa(s) = 37;

elseif (rsns_m17(s)==5 & rsns_m8(s)==3)
doa(s) = 38;

elseif (rsns_m17(s)==5 & rsns_m8(s)==2)
doa(s) = 39;

elseif (rsns_m17(s)==4 & rsns_m8(s)==2)
doa(s) = 40;

elseif (rsns_m17(s)==4 & rsns_m8(s)==1)
doa(s) = 41;
```

```
elseif (rsns_m17(s)==3 & rsns_m8(s)==1)
doa(s) = 42;

elseif (rsns_m17(s)==3 & rsns_m8(s)==0)
doa(s) = 43;

elseif (rsns_m17(s)==2 & rsns_m8(s)==0)
doa(s) = 44;

elseif (rsns_m17(s)==2 & rsns_m8(s)==1)
doa(s) = 45;

elseif (rsns_m17(s)==1 & rsns_m8(s)==1)
doa(s) = 46;

elseif (rsns_m17(s)==1 & rsns_m8(s)==2)
doa(s) = 47;

elseif (rsns_m17(s)==0 & rsns_m8(s)==2)
doa(s) = 48;

elseif (rsns_m17(s)==0 & rsns_m8(s)==3)
doa(s) = 49;

elseif (rsns_m17(s)==1 & rsns_m8(s)==3)
doa(s) = 50;

elseif (rsns_m17(s)==1 & rsns_m8(s)==4)
doa(s) = 51;

elseif (rsns_m17(s)==2 & rsns_m8(s)==4)
doa(s) = 52;

elseif (rsns_m17(s)==2 & rsns_m8(s)==5)
doa(s) = 53;

elseif (rsns_m17(s)==3 & rsns_m8(s)==5)
doa(s) = 54;

elseif (rsns_m17(s)==3 & rsns_m8(s)==6)
doa(s) = 55;

elseif (rsns_m17(s)==4 & rsns_m8(s)==6)
doa(s) = 56;
```

```

elseif (rsns_m17(s)==4 & rsns_m8(s)==7)
doa(s) = 57;

elseif (rsns_m17(s)==5 & rsns_m8(s)==7)
doa(s) = 58;

elseif (rsns_m17(s)==5 & rsns_m8(s)==8)
doa(s) = 59;

elseif (rsns_m17(s)==6 & rsns_m8(s)==8)
doa(s) = 60;

elseif (rsns_m17(s)==6 & rsns_m8(s)==7)
doa(s) = 61;

elseif (rsns_m17(s)==7 & rsns_m8(s)==7)
doa(s) = 62;

elseif (rsns_m17(s)==7 & rsns_m8(s)==6)
doa(s) = 63;

else
    doa(s) = 100; % if the vector does not map, 100
is the error code

end

% Uses the formula asin[(-34)/64] to find bin center
gamma=2*doa(s)+1;
bin_center(s)=asin(gamma*sf/64)*180/3.1415;

% if
if doa(s)==100
    bin_center(s)=0; % if the vector did not map,
reports as broadside
end
angle_error(s)=bin_center(s)-(s-900)/10;

%Calculation of RMS Reporting Error
%if statement eliminates excessive errors and subs with
mean error.
if abs(angle_error(s)) <= 15
Sum_AE = Sum_AE + angle_error(s)*angle_error(s);

```

```

        Excess_RE=Excess_RE+1;
    end
end

z=0:63;

for l=1:64
    bin_count(l)=0;
end

for lb =1:1801
    if doa(lb)==100
        bc=1;
    else
        bc=doa(lb)+1;
    end
    bin_count(bc)=bin_count(bc)+1;
end

figure(4)
hold
plot(z,bin_count,'k'), axis([0,63,0,60]),grid
hold off
xlabel('Bin Number')
ylabel('Bin Population')

figure(5)
plot(xarray,doa,'k'),axis([-90,90,0,65])
xlabel('Angle of Arrival (degrees)')
ylabel('Bin Number')
grid

figure(6)
plot(xarray,bin_center,'k'),grid
axis([-90,90,-90,90]);
xlabel('Angle of Arrival (degrees)')
ylabel('Reported Angle of Arrival (degrees)')

figure(7)
plot(xarray,angle_error,'k'),grid
axis([-60,60,-2,2]);
ylabel('Reporting Error (degrees)')

```

```
xlabel('Angle of Arrival (degrees)')  
% end of program.
```

```

% AOA_Map.m Maps bin number to the angle of arrival for
measured data
% MAKE SURE THE MEASURED BIN IS IN THE 7TH COLUMN!!!
% LT Dave Wickersham 16 Mar 00

clear all;
M=64; % dynamic range
sf=1;%sqrt(3)/2; % scale factor

load p30.dat;

df1=p30;

doa=df1(:,7);
point_num=length(df1); % determines
number of samples
xarray=[-90:180/(point_num-1):90]; % determines
resolution bit

sb17=df1(:,2);
sb8=df1(:,4);

for s=1:point_num

    gamma(s)=-1+(2*doa(s)+1)/M;
    bin_center(s)=asin(gamma(s)/sf)*180/pi;
    if doa(s)==100
        bin_center(s)=0;
    end
end

figure(1)
plot(xarray,doa,'k'),axis([-90,90,0,65])
% title('Bin Number for p33')
xlabel('Angle of Arrival (degrees)')
ylabel('Bin Number')
grid

figure(2)
hold
plot(xarray,bin_center,'k'),axis([-90,90,-90,90])
% title('Estimated Angle of Arrival for p33')
xlabel('Angle of Arrival (degrees)')

```

```

ylabel('Estimated Angle of Arrival')
grid
hold off

figure(3)
hold
plot(xarray,sb8,'k')
plot(xarray,sb17,'--k')
axis([-90,90,1,13])
legend('Modulus 8','Modulus 17',0)
hold off
xlabel('Angle of Arrival (degrees)')
ylabel('Shift and Bias Output (volts)')
grid

```

```

%phase_error.m Determines the phase error between a
predicted and measured waveform
%2 channel input

clear all;

load p9.dat
theta=[p9(:,1)] ;

dv8=[p9(:,6)] ;
dv17=[p9(:,3)] ;
md=length(dv8) ;

% constants and design variables
N=2;
f=8e9; c=3e8; wavl=c/f;
sf=2/sqrt(3);
k=2*pi/wavl;
M=64;
nf=M/(2*N); % nf is number of folds (not really, no modulus
in this equation)
dw=nf/2; % new design for mixer ouputs

FirstMin=0;FirstMax=0;SecMin=0;SecMax=0;Max17=0;Min17=0;

rad=pi/180;

thet_r=theta*rad;

```

```

ffd8=175;      %45
ffd17=70;      %90

e8_sq=0; e17_sq=0; cnt8=0; cnt17=0;
d8=dw*wavl*sf/8;
d17=dw*wavl*sf/17;

%subroutine to find local max and min
% works because I know about where the max and min will
fall
% used to get the right quadrant for the arccos
%Mod 8
for i=(md-1)/6:(md-1)/2
    if dv8(i)<FirstMin
        FirstMin=dv8(i);
        Index1Min=i;
    end
end

for i=(md-1)/3:(md-1)/2
    if dv8(i)>FirstMax
        FirstMax=dv8(i);
        Index1Max=i;
    end
end

for i=(md-1)/2:2*(md-1)/3
    if dv8(i)<SecMin
        SecMin=dv8(i);
        Index2Min=i;
    end
end

for i=2*(md-1)/3:8*(md-1)/9
    if dv8(i)>SecMax
        SecMax=dv8(i);
        Index2Max=i;
    end
end

%Mod 17
for i=(md-1)/2:5*(md-1)/6
    if dv17(i)<Min17
        Min17=dv17(i);
        Index17Min=i;
    end
end

```

```

    end
end

for i=(md-1)/6:(md-1)/2
    if dv17(i)>Max17
        Max17=dv17(i);
        Index17Max=i;
    end
end

for n=1:md
    delt8(n)=k*d8*sin(thet_r(n))+(ffd8)*rad;      %delt8 is the
simulated total angle in rad
    unwrap(delt8(n));
    %while delt8(n)>pi
    %    delt8(n)=delt8(n)-2*pi;
    %end
    %while delt8(n)<-pi
    %    delt8(n)=delt8(n)+2*pi;
    %end

    dm8(n)=acos(dv8(n));      %dm8 is measured data's total
angle in rad
%    unwrap(dm8(n));
    if (n>=Index1Min) & (n<=Index1Max)
        dm8(n)=-dm8(n);
    end
    if (n>=Index2Min) & (n<=Index2Max)
        dm8(n)=-dm8(n);
    end

    phi8(n)=(delt8(n)-dm8(n));
%    unwrap phi8(n);
    while phi8(n)>pi
        phi8(n)=phi8(n)-2*pi;
    end
    while phi8(n)<-pi
        phi8(n)=phi8(n)+2*pi;
    end

```

```

delt17(n)=k*d17*sin(the_r(n))+(ffd17)*rad;    %delt17 is
the simulated total angle in rad
%   unwrap(delt17(n));
while delt17(n)>pi
    delt17(n)=delt17(n)-2*pi;
end
while delt17(n)<-pi
    delt17(n)=delt17(n)+2*pi;
end

dm17(n)=acos(dv17(n));      %dm17 is measured data's total
angle in rad

if n>=Index17Min
    dm17(n)=-dm17(n);
end

if n<=Index17Max
    dm17(n)=-dm17(n);
end

phi17(n)=(delt17(n)-dm17(n));
while phi17(n)>pi
    phi17(n)=phi17(n)-2*pi;
end
while phi17(n)<-pi
    phi17(n)=phi17(n)+2*pi;
end

end

phi8=phi8/rad;
phi17=phi17/rad;

for i=1:md                      %phi contributes to
RMS error only if it is real
    e8_sq = e8_sq + (real(phi8(i))*real(phi8(i)));
    e17_sq = e17_sq+ (real(phi17(i))*real(phi17(i)));
end

```

```

rms8=sqrt(e8_sq)/(md-1); %calculate RMS phase error
for each channel
rms17=sqrt(e17_sq)/(md-1);

disp(['RMS Phase Error of Mod 8 is ',num2str(rms8),' '])
disp(['RMS Phase Error of Mod 17 is ',num2str(rms17),' '])

figure(1)
hold
%plot(p12(:,4),p12(:,8),'--r')
plot(theta,phi8,'k');
plot(theta,phi17,'.-k');
axis([-90,90,-90,90])
hold off
legend('Mod 8','Mod17',0)
xlabel('Angle of Arrival (degrees)'),ylabel('Phase Error
(degrees)');
grid
%title(['Phase Error between Simulated and Measured Data,
Pattern 32'])
orient landscape

```


APPENDIX B. LABVIEW VI CODE

LABVIEW Virtual Instruments (VI) code has been used to create the data collection programs. These VI codes are updated for the LABVIEW 5.1 revision and are located in the D:\Anechoic Chamber\Programs\vi for LV5.1\RSNS-OSNS Antenna directory.

The General Purpose Interface Bus (GPIB), also called IEEE 488, is a method of communicating with standard-alone instruments, such as multimeters and oscilloscopes. The most direct method is to install a plug-in GPIB board in the computer and connect the respective instrument directly to this board with a GPIB cable, as the Figure B-1 shows. The GPIB cable consists of a shielded 24-conductor cable, which has both a plug and a receptacle connector at each end, as Figure B-2 shows.

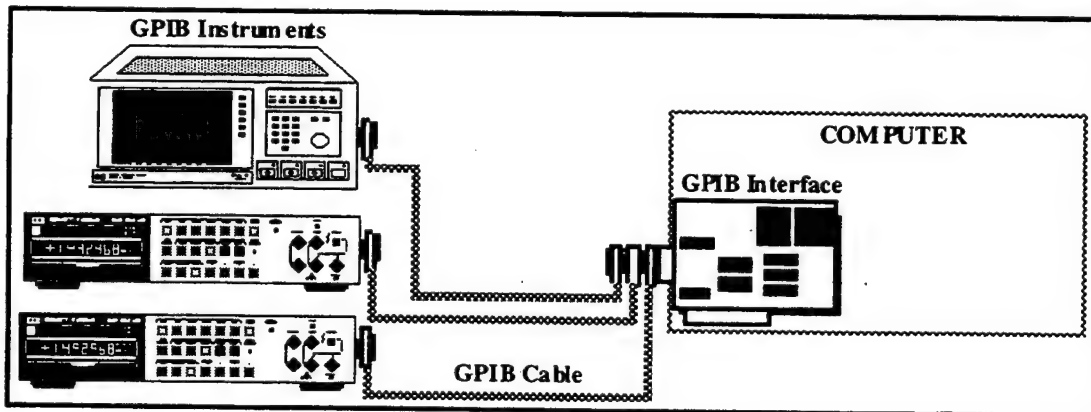


Figure B-1: Configuration to Link Devices Using a GPIB Cable. [16]

The GPIB carries device-dependent messages and interface messages. GPIB devices can be Talkers, Listeners, and Controllers. A multimeter, like in our case, is a Talker and may be a Listener as well. The Controller manages the flow of information on the GPIB by sending commands to all devices.

With the GPIB interface board and its software, the computer plays all three roles:

- Controller – to manage the GPIB,
- Talker – to send data,
- Listener – to receive data.

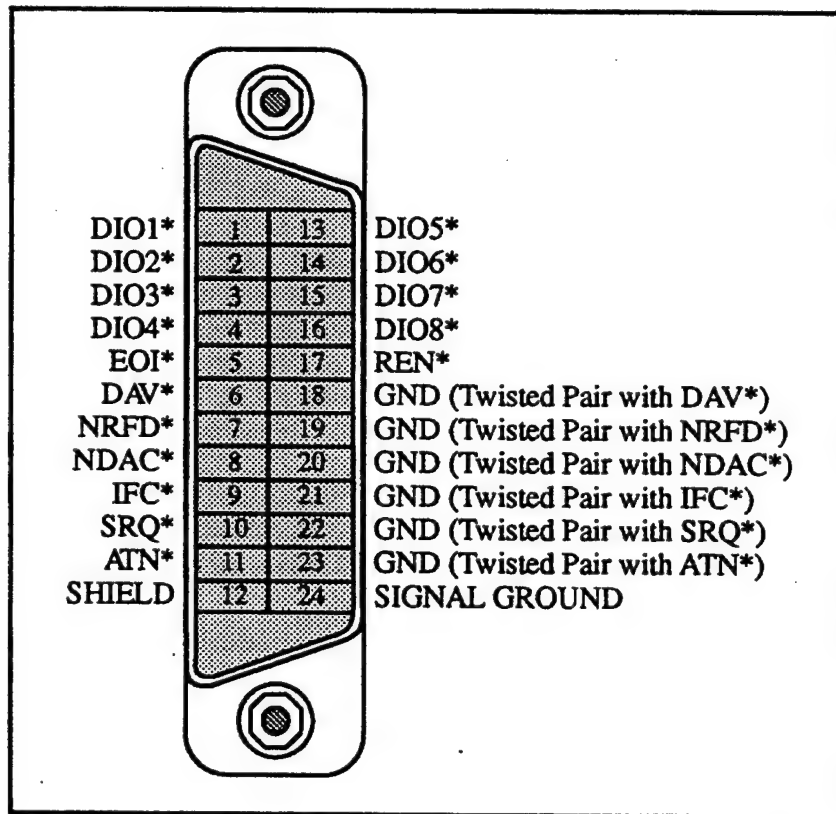


Figure B-2: A GPIB Connector Showing Signal Assignment. [16]

After this small analysis, the code will be understandable easily.

Any VI contains an interactive user interface, which is called the front panel, because it simulates the panel of physical instrument. The front panel can contain knobs, push buttons, graphs, and other controls and indicators, as shown in Figure B-3. VI receives instructions from a block diagram, which it can be constructed using the graphical programming language, G. We can think of the block diagram as source code.

The procedure for this code and the small steps, that are followed for the successful communication between a GPIB device and a computer, are shown below:

- i. Service Request (SRQ). The GPIB line that the device asserts to notify the CIC (Controller-In-Charge) that the device needs servicing.
- ii. Writes command string and send it to the GPIB device (multimeter), as the frame 0 in Figure B.4 shows.
- iii. Waits for GPIB to assert SRQ to indicate that reading is available, as shown in Figure B-5 (frame 1).
- iv. Reads measurement from multimeter, as shown in Figure B.5 (frame 2).
As the left icon in this frame indicates, reads by the count number of bytes from the GPIB device (multimeter). As the right icon indicates, it copies the measurement value.
- v. Figure B-6 shows that it clears the SRQ mode in order to be ready for the next request. [16]

Thomas.vi
Last modified on 10/3/97 at 1:56 AM

Page 1

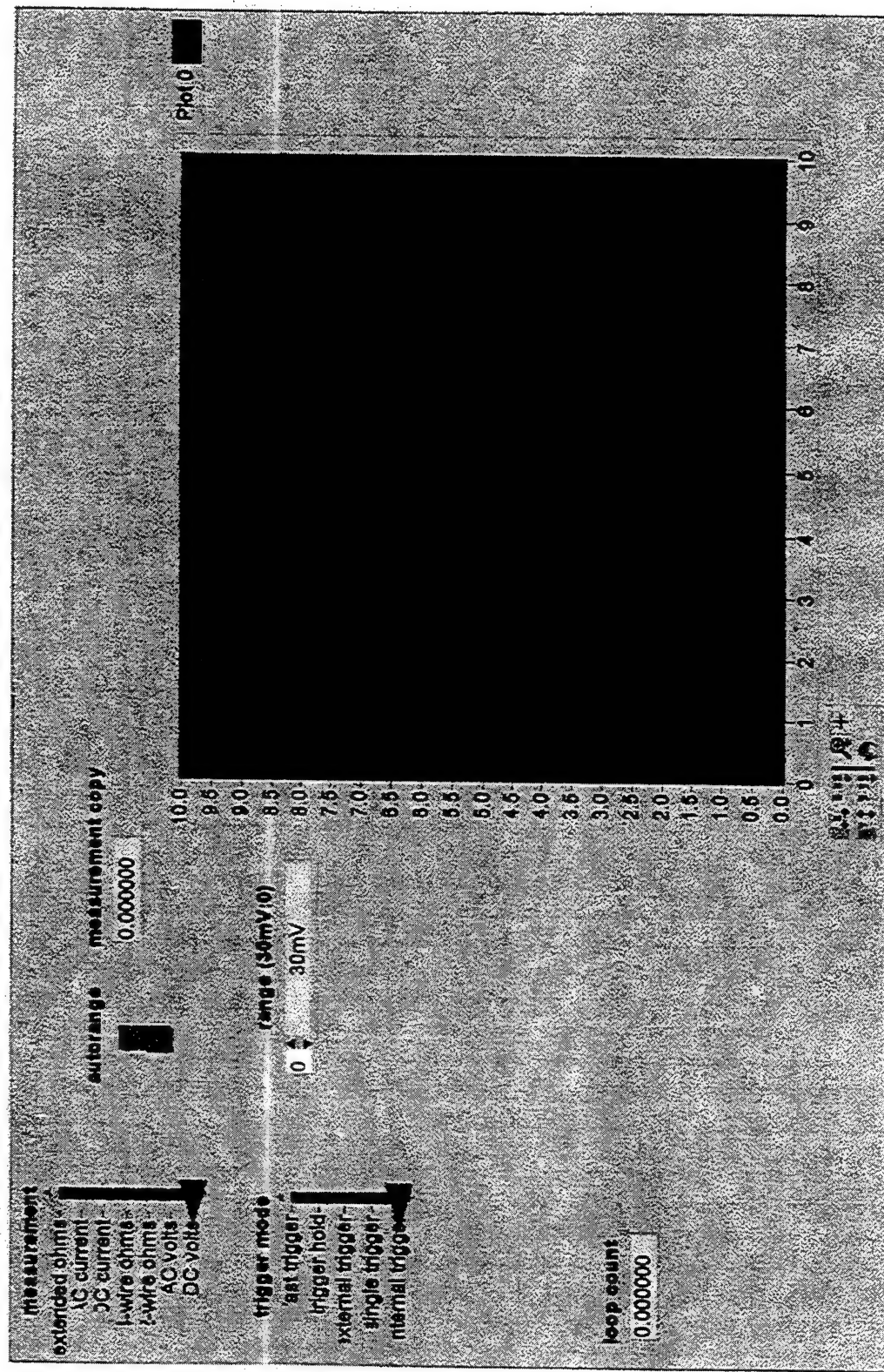


Figure B-3: Front Panel.

Thomas.vi
Last modified on 10/3/97 at 11:56 AM

Page 1

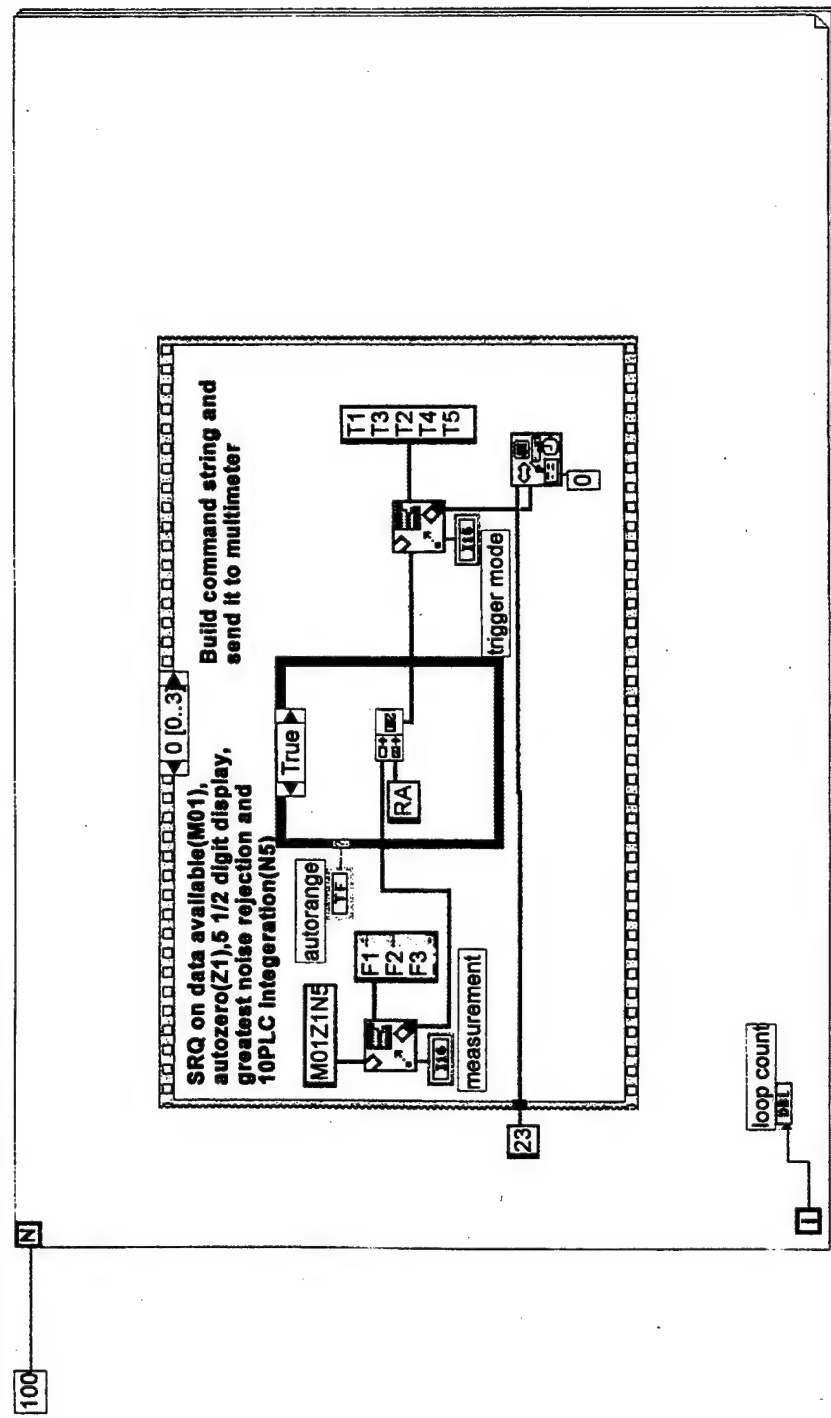


Figure B-4: Writes Command String to the GPIB Device (Multimeter).

Thomas.vi
Last modified on 10/3/97 at 11:56 AM



Page 2

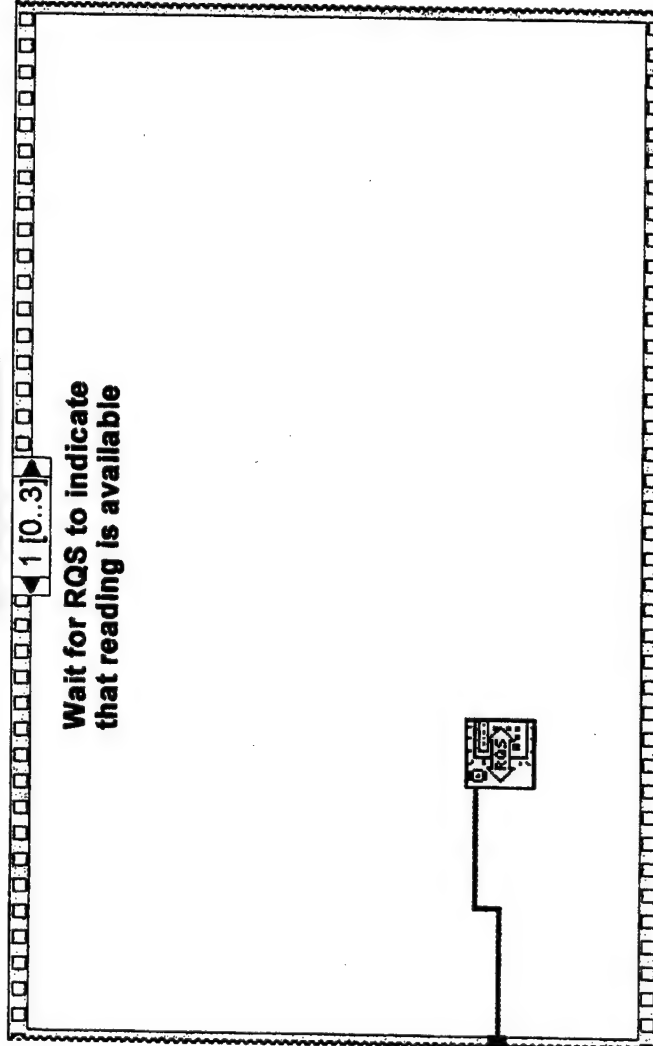
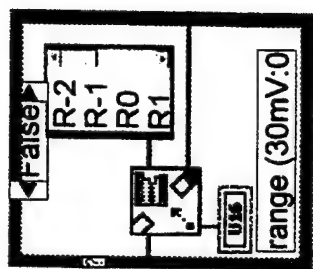


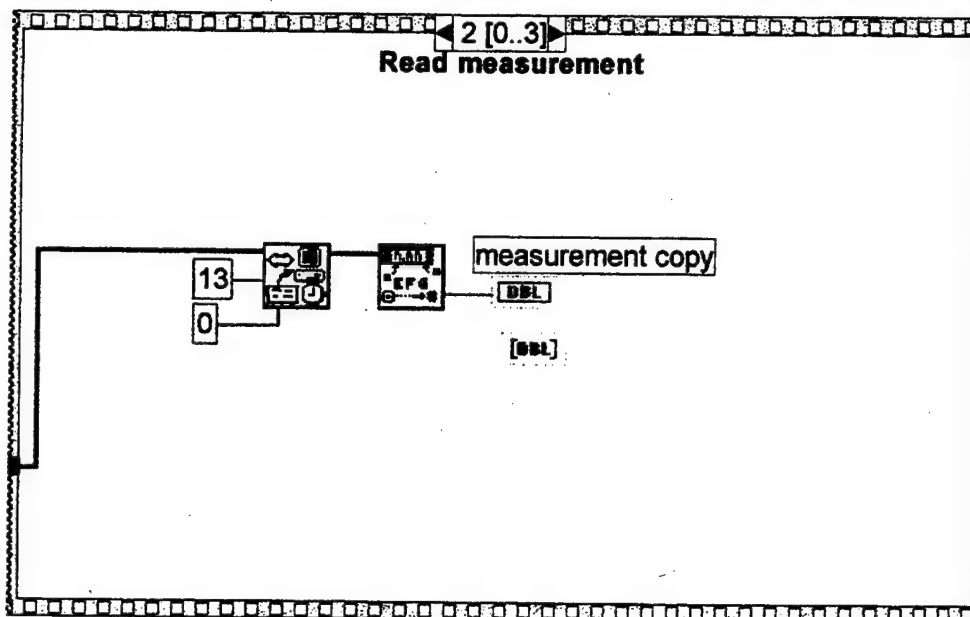
Figure B-5: Frame 1 Waits for GPIB to Assert SRQ.

Frame 2 Reads Measurement from Multimeter.

Thomas.vi

Last modified on 10/3/97 at 11:56 AM

Page 3



Thomas.vi

Last modified on 10/3/97 at 11:56 AM

Page 4

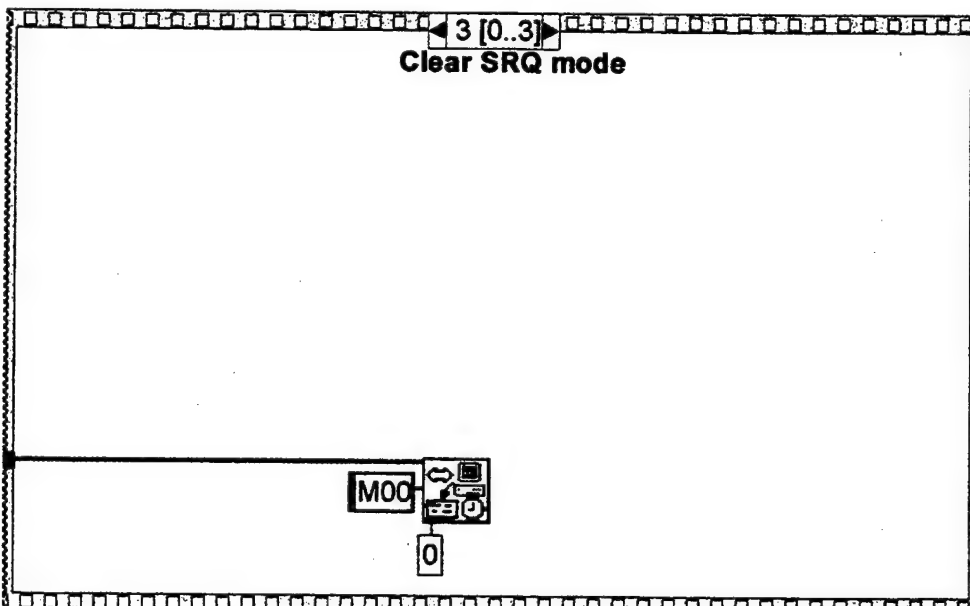


Figure B-6: Clears the SRQ Mode to be Ready for the Next Request.

APPENDIX C. THREE CHANNEL RSNS ARRAY DESIGN RESULTS

This Appendix presents the design of a 3-channel RSNS prototype array. The element geometry is presented and followed by the predicted folding waveforms and transfer function. The measured results are presented in Chapter VII Section D.

The moduli are $m_1 = 6$, $m_2 = 11$, and $m_3 = 17$. The dynamic range is 226. The element spacings are calculated from (4.20) with $N=3$. The two dummy elements are placed to minimize any mutual coupling that may be present. The array geometry is shown in Figure C-1.

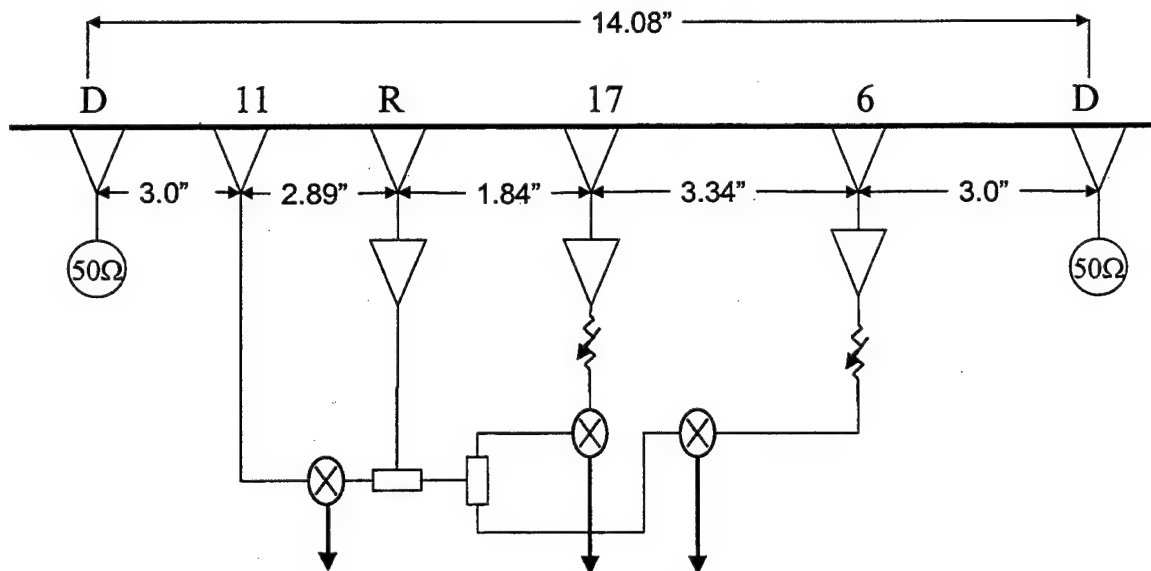


Figure C-1: 3 Channel RSNS Prototype Array Geometry.

The folding waveforms for each modulus are shown as Figures C-2 through C-4. The thermometer code is presented as Table C-1 with the comparator thresholds determined by (4.12). Figure C-5 shows the simulated bin mapping of the antenna. The RMS resolution is 0.55 degrees.

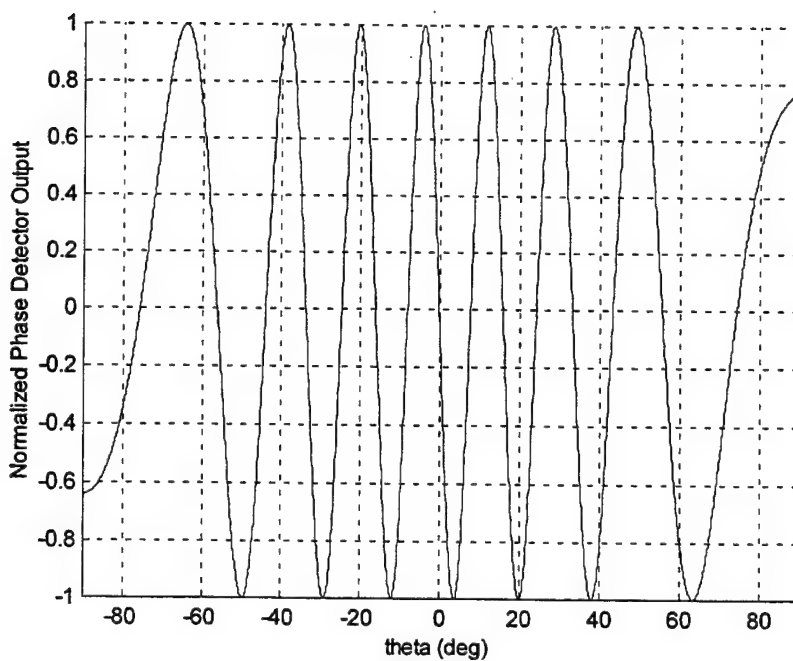


Figure C-2: Folding Waveform for Three Channel Array Modulus 6.

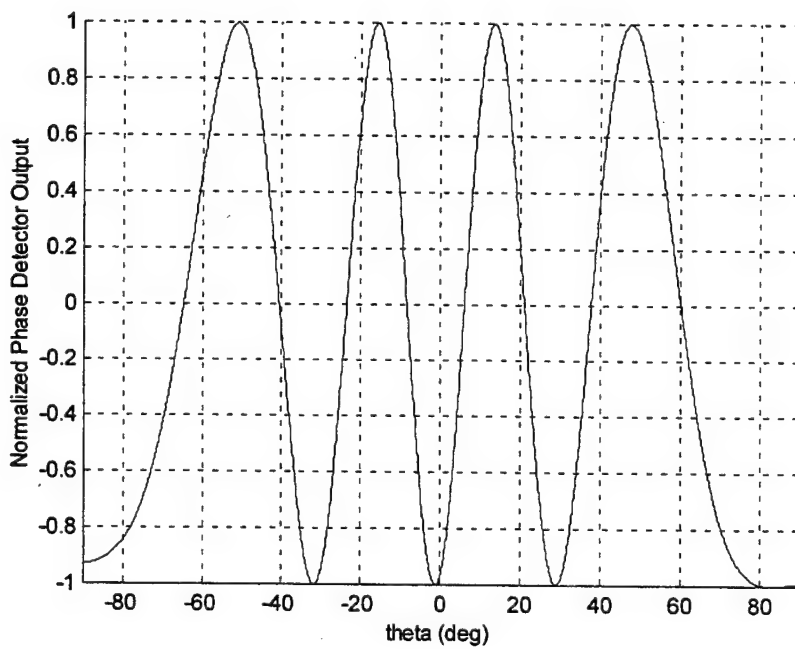


Figure C-3: Folding Waveforms for Three Channel Array Modulus 11.

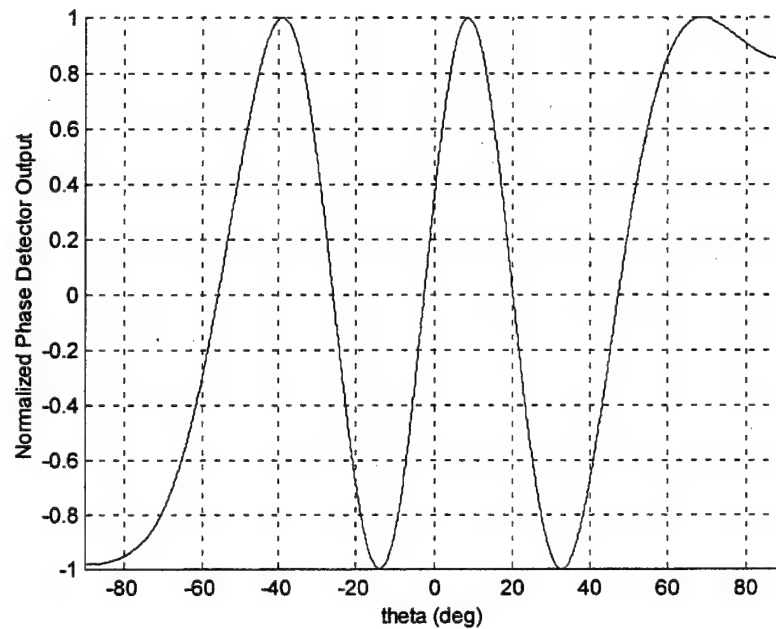


Figure C-4: Folding Waveforms for Three Channel Array Modulus 17.

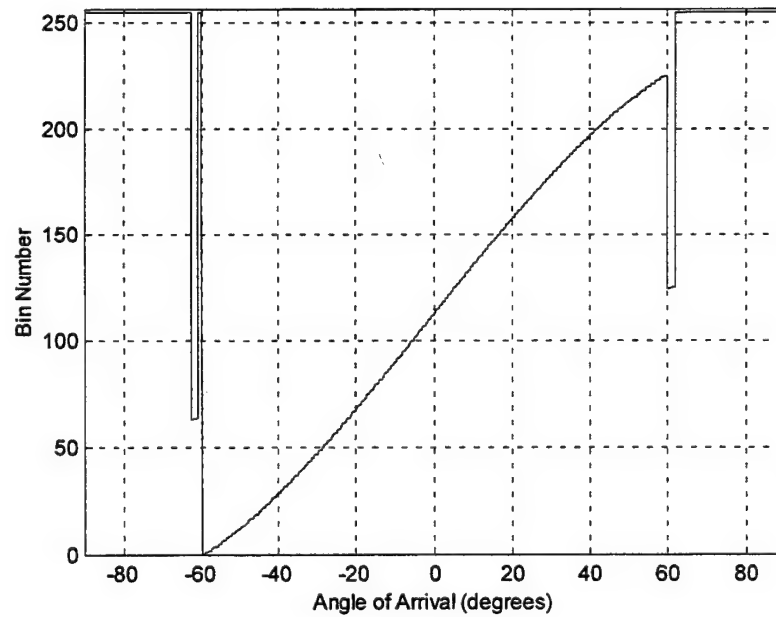


Figure C-5: Bin Mapping of RSNS 3 Channel Prototype Array.

LIST OF REFERENCES

1. R.L. Musselman and J.D. Norgard, "Frequency Invariant Interferometry," *IEEE Proceedings of Antennas and Propagation Society International Symposium*, Vol. 4, pp. 2101-2104, July 1992.
2. E. Jacobs and E.W. Ralson, "Ambiguity Resolution in Interferometry," *IEEE Transactions on Aerospace and Electronic Systems*, Vol. AES-17, No. 6, pp. 766-780, November 1981.
3. Y.W. Wu, S. Rhodes, and E.H. Satorius, "Direction of Arrival Estimation Via Extended Phase Interferometry," *IEEE Transactions on Aerospace and Electronic Systems*, Vol. 31, No. 1, pp. 375-382, January 1995.
4. A.J. Weiss and B. Friedlander, "Mutual Coupling Effects on Phase-Only Direction Finding," *IEEE Transactions on Antennas and Propagation*, Vol 40, No. 5, pp. 535-541, May 1992.
5. D. Peavy and T. Ogumfunmi, "The Single Channel Interferometer Using A Pseudo-Doppler Direction Finding System," *IEEE Transactions on Acoustics, Speech, and Signal Processing*, Vol. 5, pp. 4129-32, April 1997.
6. W.A.U. Titze, P.V. Brennan, and R. Benjamin, "Direction Finding System Using Symmetric-Pair Antenna Arrays," *IEE Preceedings on Radar, Sonar, and Navigation*, Vol. 142, No. 3, pp. 130-6, June 1995.
7. Herndon H. Jenkins, *Small-Aperture Radio Direction Finding*, Artech House Inc, Norwood, MA, 1991.
8. Stephen E. Lipsky, *Microwave Passive Direction Finding*, John Wiley & Sons, Inc., NY, 1987.
9. P. Pace, J.L. Schafer, and D. Styer, "Optimum Analog Preprocessing for Folding ADC's," *IEEE Transactions on Circuits and SystemsSystems-II: Analog and Digital Signal Processing*, Vol 42, No. 12, December 1995.
10. D. Jenn, P. Pace, T. Hatzithanasiou, "High Resolution Wideband Direction Finding Arrays Based On Optimum Symmetrical Number System Encoding," *Electronics Letters*, Vol 34, No. 11, May 28, 1998, pp. 1062-1063.

11. Thomas Hatzithanasiou, "Optimum Symmetrical Number System Phase Sampled Direction Finding Antenna Architectures," Naval Postgraduate School Master's Thesis, June 1998.
12. Pace, P.E., Styer, D., and Akin, I.A., "A Folding ADC Preprocessing Architecture Employing a Robust Symmetrical Number System with Gray-Code Properties," *IEEE Transactions on Circuits and Systems-II: Analog and Digital Signal Processing*, Accepted for publication.
13. I. Niven, H.S. Zukerman and H.L. Montgomery, *An Introduction to the Theory of Numbers*, 5th Ed. John Wiley and Sons Inc, New York, 1991.
14. I.A. Akin, "A Robust Symmetrical Number System with Gray Code Properties for Applications in Signal Processing," Naval Postgraduate School Master's Thesis, September 1997.
15. Bugg, D.V., *Electronics: Circuits, Amplifiers and Gates*, Institute of Physics Publishing, Philadelphia, 1991, p 97.
16. National Instruments, *LabVIEW Data Acquisition VI Reference Manual*, National Instruments Corporate Headquarters, Austin, TX, 1995.

INITIAL DISTRIBUTION LIST

	No of Copies
1. Defense Technical Information Center.....	2
8725 John J. Kingman Rd., STE 0944	
Ft. Belvoir, VA 22060-6218	
2. Dudley Knox Library	2
Naval Postgraduate School	
411 Dyer Rd.	
Monterey, Ca 93943-5101	
3. Chairman, Code PH	1
Department of Physics	
Naval Postgraduate School	
Monterey, CA, 93943-5121	
4. Professor Phillip E. Pace, Code EC/PC	1
Department of Electrical and Computer Engineering	
Naval Postgraduate School	
Monterey, CA, 93943-5121	
5. Professor D. Scott Davis, Code PH/DV	1
Physics Department	
Naval Postgraduate School	
Monterey, CA, 93943-5121	
6. Professor David C. Jenn, Code EC/JN	1
Department of Electrical and Computer Engineering	
Naval Postgraduate School	
Monterey, CA, 93943-5121	
7. Director, Center for Reconnaissance Research.....	2
(Attention: Professor John Powers, Code EC/PO)	
Naval Postgraduate School	
Monterey, CA, 93943-5121	
8. Engineering and Technology Curricular Office, Code 34	1
Naval Postgraduate School	
Monterey, CA, 93943-5121	

9. Commanding Officer, Naval Research Laboratory1
Attn: Mr. Alfred DiMatta, Code 5701.00
4555 Overlook Ave SW
Washington, DC, 20375-5339

10. Professor David Styer1
16 Brandywine Dr.
Cincinnati, OH, 45246-3809

11. Mr. Raju Chandra.....1
Manager, EW/Antenna Products
Condor Systems
2133 Samaritan Drive
San Jose, CA, 95124

12. Lieutenant David J. Wickersham1
6393 Falling Leaf Circle
Parker, CO, 80132